NATIONAL TECHNICAL UNIVERSITY OF ATHENS

SCHOOL OF APPLIED MATHEMATICAL AND PHYSICAL SCIENCES

DEPARTMENT OF PHYSICS

Monolithic diamond Raman resonators for high-resolution spectroscopy

DIPLOMA THESIS

Georgios STOIKOS

Committee:

Prof. R. Vlastou-Zanni
Prof. M. Kokkoris
Prof. A. Papayannis

Supervisor:

Dr. E. Granados

ATHENS 2023

Περίληψη

Ο σκοπός αυτής της μελέτης είναι να διερευνήσει την αναγκαιότητα και τις λύσεις για συντονίσιμες, φασματικά καθαρές πηγές laser σε ορατά μήκη κύματος για διάφορες εφαρμογές στη φασματοσκοπία, τη μετρολογία και την κβαντική τεχνολογία. Η εργασία προτείνει συντονιστές Raman μονολιθικού διαμαντιού ως κλιμακούμενες, συντονίσιμες, μονής συχνότητας πηγές laser . Αυτοί οι συντονιστές έχουν σχεδιαστεί για να αντιμετωπίζουν τους περιορισμούς των σημερινών laser στενού φάσματος που είναι ογκώδη και πολύπλοκα.

Το Κεφάλαιο 1 της μελέτης παρέχει μια εισαγωγή στα φασματικά καθαρά λέιζερ και τις εφαρμογές τους, εξηγεί πώς το στενό εύρος γραμμής των laser, ειδικά laser μονής διαμήκους λειτουργίας (single-longitudinal-mode, SLM) ή laser μονής συχνότητας, είναι απαραίτητο για εφαρμογές υψηλής ευαισθησίας όπως ατομικά ρολόγια, ψύξη ύλης και αντιύλης και παγίδευση και χειρισμό ιόντων για κβαντικούς υπολογισμούς και κβαντικές μνήμες. Η έλλειψη ποικιλίας και επεκτασιμότητας τέτοιων laser έχει οδηγήσει στην ανάγκη για νέες πηγές laser που συνδυάζουν χαρακτηριστικά όπως η σταθερότητα, η ακρίβεια, η δυνατότητα συντονισμού και η ανοχή ισχύος, διατηρώντας παράλληλα την επεκτασιμότητα. Η εργασία εστιάζει σε ένα συντονιστή Ραμαν μονολιθικού διαμαντιού που δημιουργεί ένα πεδίο laser μονής συχνότητας μέσω εξαναγκασμένης σκέδασης Raman (stimulated Raman scattering, SRS) σε διαμάντι. Ο συντονιστής προσφέρει δυνατότητες συντονισμού μεγάλης ακρίβειας ενώ εκπέμπει παλμούς νανοδευτερολέπτων και θεωρείται εξαιρετικά κατάλληλο για ολοκληρωμένες on-chip πηγές laser για κλιμακούμενες εφαρμογές.

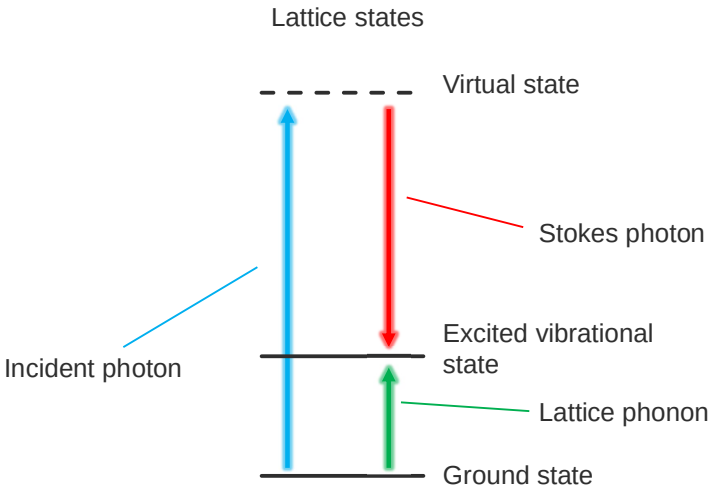

Σχήμα 1: Προσπίπτον φωτόνιο απορροφάται απο το πλέγμα, διεγείροντας το σε ένα φανταστικό επίπεδο ενέργειας το οποίο αποδιεγείρεται σε ένα δονητικό επίπεδο εκμπέμποντας ένα φωτόνιο Stokes χαμηλότερης συχνότητας.

Παρέχεται επίσης μια επισκόπηση του φαινομένου Raman και της χρήσης του ως μέθοδος laser στην ολοκληρωμένη φωτονική. Το κεφάλαιο ολοκληρώνεται με μια συζήτηση του τρόπου με τον οποίο τα αποτελέσματα των προηγούμενων μελετών χρησιμοποιούνται για τη διεξαγωγή μιας επίδειξης φασματοσκοπίας υψηλής ανάλυσης χρησιμοποιώντας διαμάντι, δείχνοντας την καταλληλότητά του για εφαρμογές χειρισμού ιόντων.

Το Κεφάλαιο 2 της μελέτης διερευνά τη φυσική πίσω από το φαινόμενο Raman και την SRS που παράγει πεδία laser. Το φαινόμενο Raman είναι ένα από τα τέσσερα βασικά

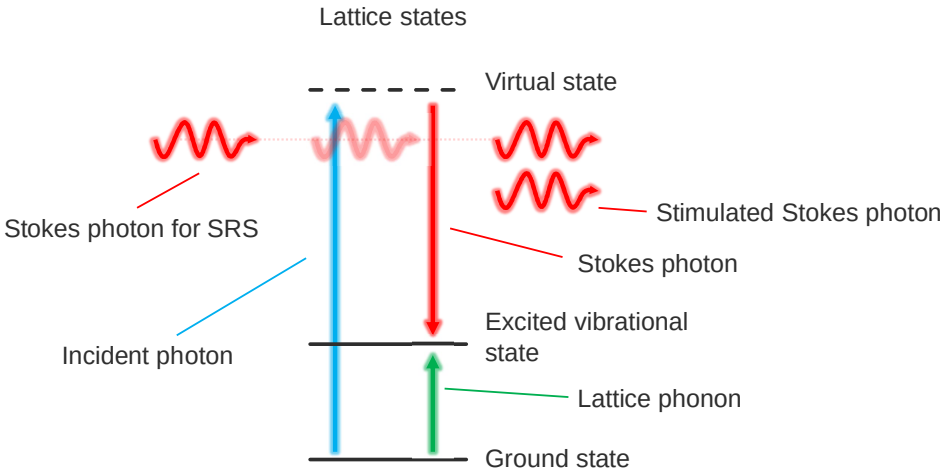

Σχήμα 2: Γραφική παράσταση εξαναγκασμένης σκέδασης Raman όπου ένα προϋπάρχον φωτόνιο Stokes εξαναγκάζει τη διαδικασια σκέδασης.

φαινόμενα σκέδασης που συμβαίνει κατά τη διάδοση του φωτός στην ύλη, και περιλαμβάνει την απορρόφηση φωτονίων από ένα υλικό και τη διέγερση του κρυσταλλικού πλέγματος του σε ένα εικονικό ενεργειακό επίπεδο, ακολουθούμενη από την αποδιέγερση σε υψηλότερο επίπεδο ενέργειας από ότι πριν από την απορρόφηση, εκπέμποντας ένα φωτόνιο μειωμένης ενέργειας γνωστό ως φωτόνιο Stokes. Εξηγείται η διαφορά μεταξύ της σκέδασης Raman και Brillouin, τονίζοντας ότι η σκέδαση Raman προκαλεί πολύ μεγαλύτερες μετατοπίσεις συχνότητας στο προσπίπτον φως, δημιουργώντας υπέρυθρα οπτικά φωνόνια. Ακόμα, το φαινόμενο Raman χρησιμοποιείται ευρέως στη φασματοσκοπία για χημική ανάλυση υλικών και μπορεί να χρησιμοποιηθεί για στερεά, υγρά, αέρια, ακόμη και βιολογικούς ιστούς.

Η SRS επιτυγχάνεται με την εφαρμογή ισχυρών πεδίων αντλίας, τα οποία τελικά φθάνουν σε ένα όριο όπου το αυθόρμητο φως Stokes μπορεί να διεγείρει την εκπομπή περισσότερου φωτός Stokes, παράγοντας χαρακτηριστικά laser όπως συνοχή, κατευθυντικότητα, μονοχρωματικότητα και υψηλή φωτεινότητα. Το κεφάλαιο εξηγεί τη διαφορά μεταξύ της σκέδασης SRS και Raman και υπογραμμίζει τα πλεονεκτήματα της SRS σε σχέση με άλλες μεθόδους laser. Η εφαρμογή των Raman laser μπορεί να πραγματοποιηθεί μέσω οπτικής ίνας ή κρυστάλλου, με τις πιο κοινές μεθόδους να περιλαμβάνουν αέρια. Το κεφάλαιο εξηγεί τα πλεονεκτήματα κάθε προσέγγισης, τονίζοντας τα μεγάλα μήκη αλληλεπίδρασης και το χαμηλό κατώφλι κέρδους των Raman laser οπτικών ινών, ενώ τα Raman laser όγκου κρυστάλλων λειτουργούν συνήθως σε καθεστώς παλμών ps και fs λόγω του υψηλού κατωφλίου του laser.

Παρουσιάζονται οι εφαρμογές των Raman laser στην αστρονομία, στην ψύξη ατόμων, στα ατομικά ρολόγια, στη φασματοσκοπία υψηλής ανάλυσης και στα συστήματα LIDAR. Η παραγωγή πεδίων laser μονής συχνότητας χρησιμοποιώντας διαμάντι ως ενεργό μέσο Raman ήταν επιτυχής στην ανίχνευση υδρατμών στην ατμόσφαιρα και στην επέκταση της εκπομπής μήκους κύματος των laser από ζαφείρι τιτανίου (Titanium Sapphire, Ti:Sa). Η υψηλή ισχύς και τα εξαιρετικά φασματικά χαρακτηριστικά των Raman laser διαμαντιού τα καθιστούν μια πιθανή λύση για προβλήματα που απαιτούν τέτοια χαρακτηριστικά.

Το πυρίτιο χρησιμοποιήθηκε αρχικά ως ενεργό μέσο ωστόσο αντιμετώπισε περιορισμούς ενώ το διαμάντι αποδείχθηκε πιο αποτελεσματικό υλικό λόγω της υπερευρείας διαφάνειας, της γιγαντιαίας μετατόπισης Raman και της δυνατότητας λειτουργίας σε καθεστώς βαθιάς υπεριώδους ακτινοβολίας χωρίς τις επιβλαβείς επιπτώσεις του TPA και της

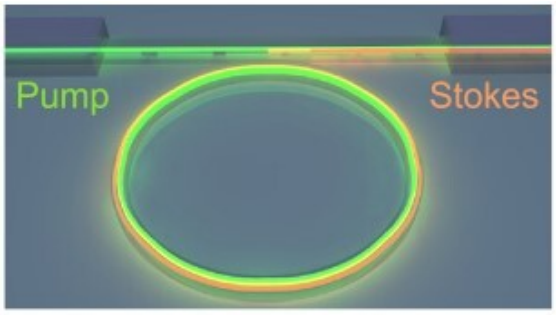

Σχήμα 3: On-chip ολοκληρωμένος κυματοδηγός συνεχούς Raman laser διαμαντιου. [1].

απορρόφησης ελεύθερου φορέα. Η καταλληλότητα του διαμαντιού ως ενεργού κρυστάλλου Ραμαν αποδείχθηκε με τη δημιουργία του πρώτου ενσωματωμένου Raman laser με διαμάντι, το οποίο είχε ιδιότητες συντονισμού σε εύρος ζώνης 100 nm με κεντρικό μήκος κύματος 2 μm. Η εργασία αναφέρει τη χρήση ενός συντονιστή διαμαντιού σε διαμόρφωση Fabry-Pérot (FP), ως πηγή πεδίων Stokes με λεπτή ρύθμιση, στενού πλάτους, ns-παλμών, εξελίσσοντας το πεδίο των on-chip Raman laser.

Συνολικά, το Κεφάλαιο 2 υπογραμμίζει τις δυνατότητες των Raman laser, ιδιαίτερα στο πλαίσιο της ολοκληρωμένης φωτονικής, και τους διάφορους περιορισμούς και πλεονεκτήματα των διαφορετικών υλικών για Raman. Το κεφάλαιο παρουσιάζει τα επιτεύγματα διαφόρων ερευνητών στη δημιουργία ολοκληρωμένων Raman laser με διαμάντι και την πιθανή επίδραση αυτών των laser σε διάφορες τεχνικές μεθοδολογίες. Το κεφάλαιο περιλαμβάνει επίσης διάφορες εικόνες, συμπεριλαμβανομένων διαγραμμάτων της οπτικής ρύθμισης που χρησιμοποιήθηκε για τη δημιουργία ενός ενσωματωμένου Raman laser με διαμάντι και ενός ενσωματωμένου κυματοδηγού για ένα on-chip CW Raman laser με διαμάντι.

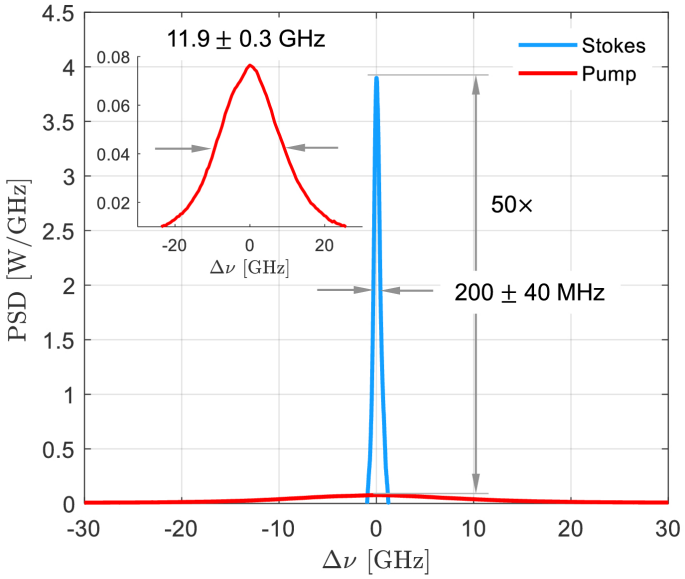

Σχήμα 4: Σύγκριση μεταξύ εύρους γραμμών του Stokes laser και της αντλίας. [2].

Το Κεφάλαιο 3 παρουσιάζει τεχνικές πτυχές του ενσωματωμένου συντονιστή Raman με διαμάντι το οποίο έχει εξαιρετικές ιδιότητες ως υλικό για μονολιθικούς συντονιστές laser. Για παράδειγμα, ο χαμηλός θερμοοπτικός συντελεστής, η αμελητέα διπλοθλαστικότητα και το μεγάλο όριο ζημιάς καθιστούν το διαμάντι ιδανικό υλικό για υψηλής φασματικής ποιότητας, ανθεκτικά στην ισχύ ενσωματωμένα Raman laser. Στη συνέχεια παρουσιάζεται η επεξεργασία των λεπτομερειών της διαμόρφωσης αντηχείου FP, η οποία αποτελείται από έναν μονό κυβοειδή κρύσταλλο διαμαντιού. Αυτός ο μονολιθικός συντονιστής με διαμάντι έχει διαστάσεις $6 \times 2 \times 2\ mm^3$ και λειτουργεί σε διαμόρφωση FP. Οι επιφάνειες του διαμαντιού λειτουργούν ως καθρέφτες στις άκρες, ενώ ο όγκος του διαμαντιού χρησιμεύει ως ενεργό μέσο Raman. Στη συνέχεια εξηγείται ο μηχανισμός πίσω από τη λειτουργία SLM και την ιδέα της ελεύθερης φασματικής περιοχής (free spectral range, FSR). Σε ένα συντονιστή FP που λειτουργεί με Raman, το φιλτράρισμα είναι ενσωματωμένο στην αρχή λειτουργίας και το κέρδος εξαντλείται ομοιογενώς με το μεγαλύτερο μέρος του να πηγαίνει στον κύριο τρόπο ταλάντωσης. Μετά το καθιερωμένο φασματικό φιλτράρισμα, το τελευταίο βήμα για την επίτευξη φωτός Stokes μονής λειτουργίας είναι να διασφαλιστεί η κατάλληλη απόσταση για τις πλευρικές λειτουργίες Stokes. Εξηγεί επίσης τις μεθόδους ρύθμισης της συχνότητας Stokes, συμπεριλαμβανομένης της ρύθμισης της θερμοκρασίας του συντονιστή και της μεταβολής άλλων εξωτερικών παραγόντων, όπως η πίεση, τα ηλεκτρικά και μαγνητικά πεδία και η γωνία έγχυσης της αντλίας. Παρουσιάζεται μια επισκόπηση του τρόπου με τον οποίο μπορεί να συντονιστεί η έξοδος μιας συχνότητας χωρίς να αυξηθεί η πολυπλοκότητα του συστήματος. Τέλος παρουσιάζεται το συμπέρασμα ότι με τη χρήση ενός μονολιθικού συντονιστή διαμαντιού, μπορούν να αποκτηθούν πεδία laser στενού πλάτους νανοδευτερόλεπτου, μέχρι το όριο Fourier, και ο μετατροπέας Raman επιτρέπει πολύ ευκολότερες μεθόδους συντονισμού για την έξοδο Stokes.

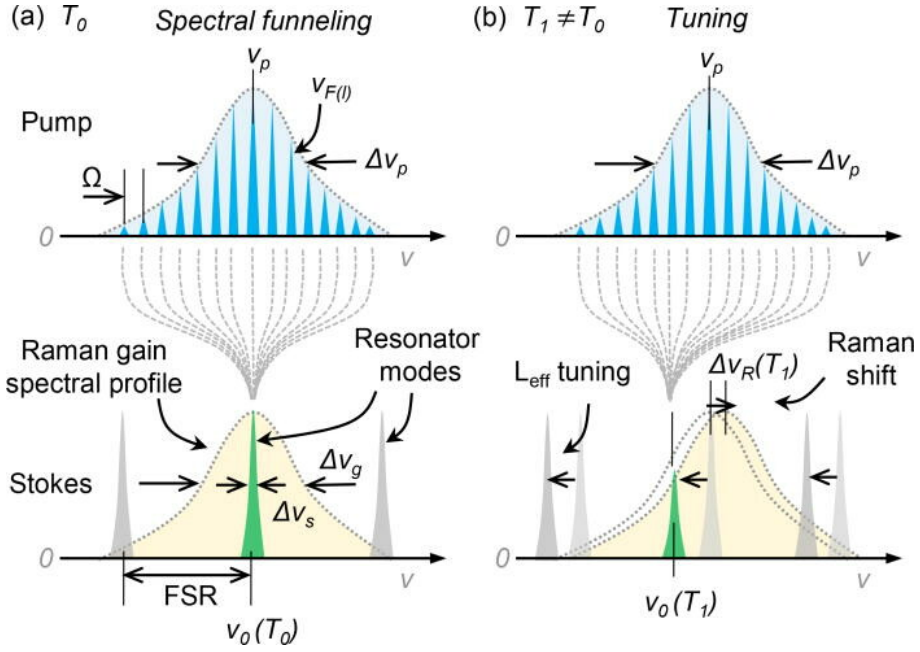

Σχήμα 5: (α)Πολυ-τροπική αντλία δημιουργεί πεδία Stokes μονής συχνότητας. (β) Θερμοκρασιακές μεταβολές αλλαζουν το πεδίο Stokes και τα φωνόνια Raman. [3].

Το Κεφάλαιο 4 συζητά τη χρήση της θερμοκρασίας ως κύριας μεθόδου συντονισμού για το πεδίο laser εξόδου σε συντονιστές Raman μονολιθικού διαμαντιού, παρουσιάζει τη φυσική πίσω από τη μέθοδο ρύθμισης θερμοκρασίας και παρέχει ένα θεωρητικό και

αριθμητικό μοντέλο για να καταδείξει τις δυνατότητές της. Η βασική ιδέα έγκειται στο γεγονός ότι το φως βλέπει ένα μήκος διαφορετικό από το φυσικό μήκος και αυτό το ενεργό μήκος δίνεται ως γινόμενο μεταξύ του φυσικού μήκους και του δείκτη διάθλασης. Στη συνέχεια εξάγεται ο ρυθμός φασματικής μεταβολής με τη θερμοκρασία, ο οποίος καθορίζεται από τις οπτομηχανικές ιδιότητες του συντονιστή. Δείχνεται επίσης ότι το εύρος των υποψήφιων συχνοτήτων καθορίζεται από τα φωνόνια Raman του διαμαντιού, των οποίων η συχνότητα εξαρτάται από τη θερμοκρασία. Στη συνέχεια, παρουσιάζεται μια πειραματική προσέγγιση για την επίδειξη των δυνατοτήτων ρύθμισης θερμοκρασίας, η οποία περιλαμβάνει την τοποθέτηση ενός μονολιθικού αντηχείου διαμαντιού μήκους 6 mm πάνω από ένα χάλκινο υπόστρωμα μέσα σε έναν φούρνο υψηλής ακρίβειας. Το διαμάντι αντλείται χρησιμοποιώντας ένα διπλασιασμένης συχνότητας Q-switched Ti:Sa laser με δυνατότητα ρύθμισης, και η πειραματική διάταξη φαίνεται στο Σχήμα 6.

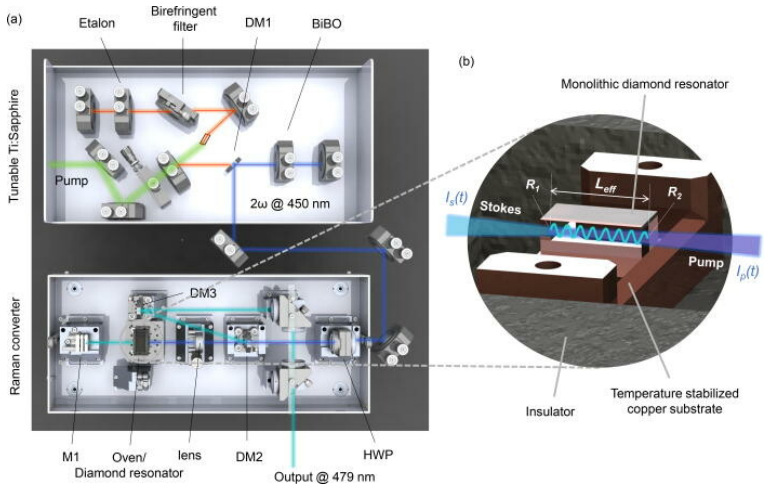

Σχήμα 6: Το Ti:Sa laser αντλεί ένα μονολιθικό αντηχείο διαμαντιού ελεγχόμενης θερμοκρασίας [3].

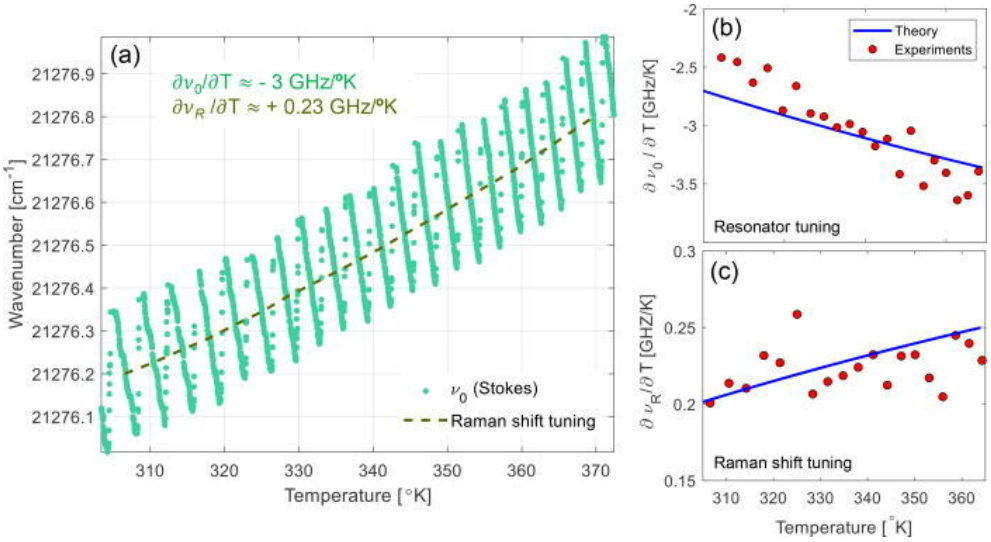

Σχήμα 7: (α) Το μήκος κύματος Stokes ως συνάρτηση της θερμοκρασίας. (β) Σύγκριση μεταξύ του μετρούμενου $\frac{\partial \nu_S}{\partial T}$ και του θεωρητικού υπολογισμού από την εξ. 4.2. (γ) Μεταβολή μετατόπισης Raman $\frac{\partial \nu_R}{\partial T}$ με τη θερμοκρασία. [3].

Επισημαίνονται επίσης οι αδυναμίες των τρεχουσών αριθμητικών προσεγγίσεων για τη μοντελοποίηση της συμπεριφοράς του συντονιστή και παρουσιάζεται μια νέα προσέγγιση που εστιάζει σε ακριβείς μετρήσεις του θερμοοπτικού συντελεστή διαμαντιού. Το Σχήμα 5, δείχνει την αντλία πολλαπλών λειτουργιών που δημιουργεί ένα πεδίο Stokes μίας λειτουργίας και τις αλλαγές θερμοκρασίας μετατοπίζοντας τόσο το πεδίο Stokes όσο και το κέρδος Raman, ενώ το Σχήμα 6, απεικονίζει την πειραματική διάταξη. Το Σχήμα 7, δείχνει το μήκος κύματος Stokes ως συνάρτηση της θερμοκρασίας και σύγκριση ρυθμών φασματικής αλλαγής.

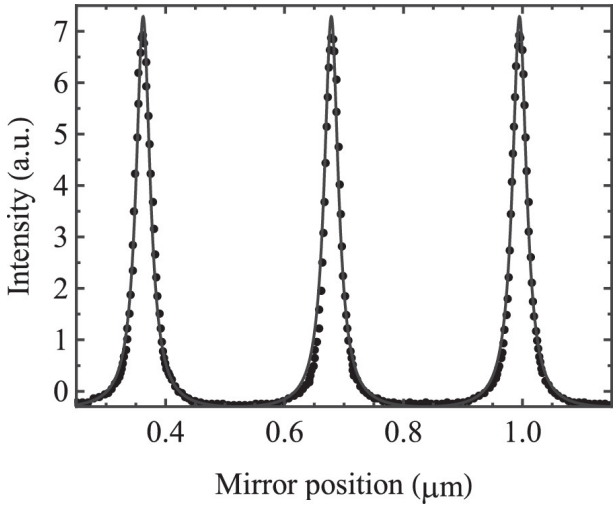

Σχήμα 8: Περιοδικοί συντονισμοί ως αλλαγές οπτικής διαδρομής. [4].

Το Κεφάλαιο 5 της εργασίας εμβαθύνει στη φυσική των δυνατοτήτων φασματικής συμπίεσης του μονολιθικού συντονιστή διαμαντιού και παρουσιάζει πειραματικά αποτελέσματα που δείχνουν σημαντική συμφωνία με τη θεωρητική πρόβλεψη, επιτρέποντας περαιτέρω στένωση εύρους γραμμής.

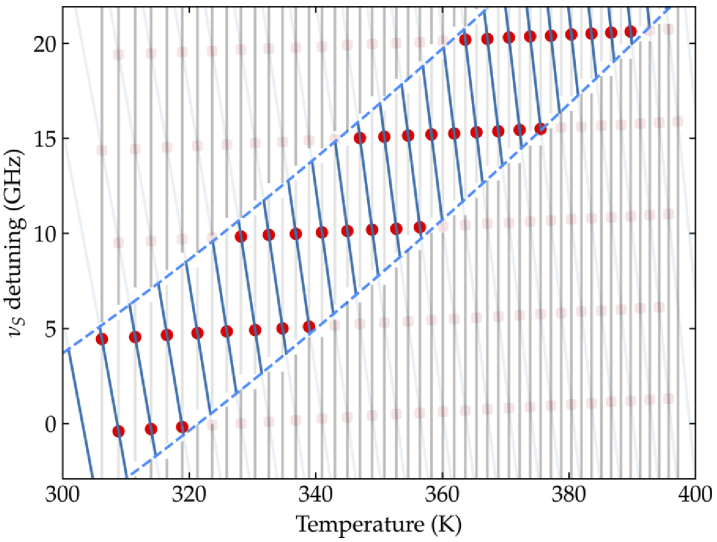

Σχήμα 9: Προβλεπόμενες περιοχές διπλού συντονισμού. Οι μπλε γραμμές δείχνουν την κεντρική συχνότητα Stokes ενώ οι γκρι γραμμές δείχνουν τις θερμοκρασίες όπου συντονίζει η αντλία. Οι κόκκινες κουκκίδες είναι οι διασταυρώσεις των μπλε και γκρίζων γραμμών όπου συμβαίνει διπλός συντονισμός. [5]

Η ενότητα 5.1 συζητά το κυρίαρχο φαινόμενο που παρατηρείται σε ένα συμβολόμετρο Fabry-Pérot (FPI) που ένα εξωτερικό πεδίο laser αντηχεί περιοδικά και μεγιστοποιεί την ενδοκοιλοτική έντασή του. Το φαινόμενο περιοδικού συντονισμού σε ένα FPI σάρωσης παρουσιάζεται στο Σχ. 8, ενώ ένα παρόμοιο φαινόμενο μπορεί να εμφανιστεί στον μονολιθικό συντονιστή διαμαντιού όταν το λέιζερ άντλησης είναι μονής λειτουργίας.

Επεξηγείται η επίδραση της θερμοκρασίας στον διπλό συντονισμό και παρουσιάζεται ένα μοντέλο για την κατανόηση του φαινομένου. Το μοντέλο και τα πειραματικά αποτελέσματα επιβεβαιώνουν ότι ο κατάλληλος συντονισμός θερμοκρασίας μπορεί να αυξήσει σημαντικά τη φωτεινότητα του πεδίου Stokes. Η συνθήκη διπλού συντονισμού μπορεί να εκπληρωθεί με σταθερότητα θερμοκρασίας $< 0.07\ K$, η οποία μπορεί να οδηγήσει σε περαιτέρω βελτίωση της φασματικής πυκνότητας ισχύος (power spectral density, PSD) με κατάλληλα συστήματα ελέγχου.

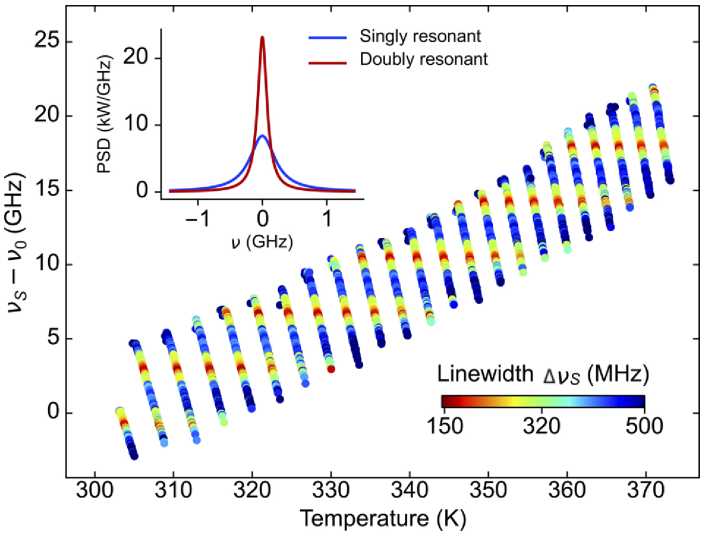

Σχήμα 10: Μετρημένη συχνότητα Stokes με χρωματικό χάρτη με βάση το πλάτος γραμμής. Το ένθετο συγκρίνει το PSD μεταξύ μονής και διπλής αντήχησης. [5]

Το Σχήμα 9 προβλέπει περιοχές διπλού συντονισμού, ενώ το Σχήμα 10 δείχνει τη μετρούμενη συχνότητα Stokes με έναν χρωματικό χάρτη που βασίζεται στο πλάτος γραμμής και συγκρίνει το PSD μεταξύ μονού και διπλού συντονισμού.

Το Κεφάλαιο 6 εστιάζει στην πρακτική εφαρμογή του μονολιθικού συντονιστή διαμαντιού για φασματοσκοπία υψηλής ευκρίνειας και περιγράφει τις απαιτήσεις και τις αρχές πίσω από τη φασματοσκοπία υψηλής ανάλυσης (high resolution spectroscopy HRS), τον τρόπο μείωσης της διεύρυνσης Doppler, την πειραματική ρύθμιση και τα αποτελέσματα του πειράματος.

Στο Σχήμα 11, παρουσιάζεται η διαδικασία φασματοσκοπίας ιονισμού συντονισμού (RIS). Το Σχήμα 12 δείχνει περαιτέρω τη σημασία της μείωσης της διεύρυνσης Doppler για να καταστεί δυνατή η φασματοσκοπία HRS. Για τη μείωση της διεύρυνσης Doppler, συζητείται η ιδέα της φασματοσκοπίας διασταυρούμενης δέσμης και τη χρήση του συστήματος Perpendicularly Illuminated Laser Ion Source and Trap, PI-LIST. Το κεφάλαιο περιγράφει περαιτέρω την πειραματική ρύθμιση, η οποία έλαβε χώρα στην εγκατάσταση Offline-2 στο CERN. Το σχήμα 13 παρέχει μια γραφική αναπαράσταση της οπτικής ρύθμισης για το πείραμα, το οποίο χρησιμοποίησε ένα σχήμα ιονισμού δύο σταδίων σε ^{152}Sm.

Τα αποτελέσματα του πειράματος παρουσιάζονται στα Σχήματα 14 και 15. Το Σχήμα 14 δείχνει την κεντρική συχνότητα Stokes που αποσυντονίζεται με τη θερμοκρασία, με

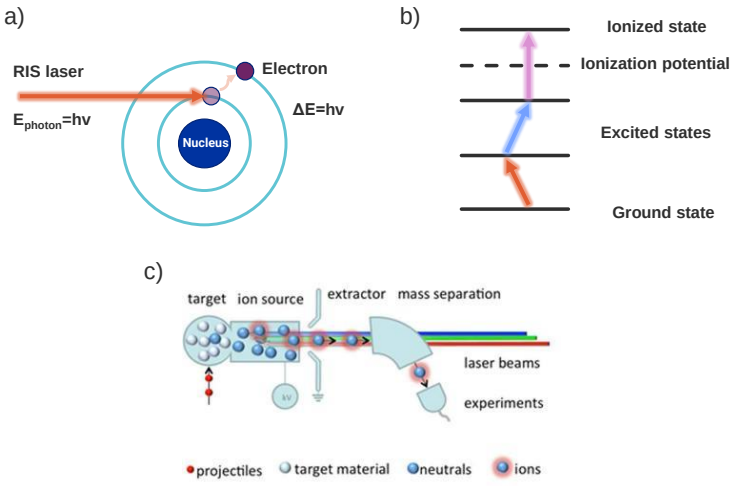

Σχήμα 11: (α) Το RIS laser παρέχει φωτόνια της ακριβούς ενέργειας που απαιτείται για μια μετάβαση. (β) Διαδοχικές σταδιακές διεγέρσεις οδηγούν σε ιονισμό. (γ) Επιδείξη επιλεκτικότητας του συστήματος.

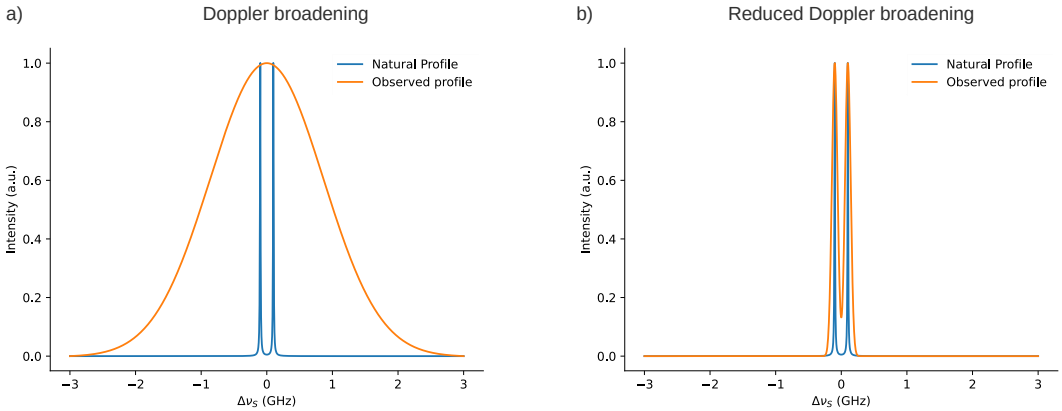

Σχήμα 12: (α) Η διεύρυνση Doppler είναι αρκετά μεγάλη ώστε να ενσωματώσει τις δύο ενεργειακές καταστάσεις, καθιστώντας τις δυσδιάκριτες. (β) Η μειωμένη διεύρυνση Doppler καθιστά τις δύο ενεργειακές καταστάσεις χωριστές.

το ένθετο να δείχνει το φάσμα της εξόδου Stokes. Η εικόνα δείχνει ένα πλάτος γραμμής FWHM $\Delta\nu_S = 170$ MHz. Το Σχήμα 15 δείχνει το ρεύμα ιόντων ως συνάρτηση της κεντρικής συχνότητας Stokes, με προσαρμογη σε κορεσμένη Lorentzian με FWHM 0.51 GHz. Η ανάλυση είναι κατάλληλη για φασματοσκοπία HRS, επιτρέποντας ακριβή φασματοσκοπία και μετρήσεις μετατόπισης ισοτόπων.

Το Κεφάλαιο 7 συζητά τη σημασία των φασματικά καθαρών πεδίων laser σε εφαρμογές υψηλής ακρίβειας όπως οι κβαντικοί υπολογιστές, η κβαντική μετρολογία και η έρευνα πυρηνικής φυσικής. Η ιδανική πηγή laser μονής συχνότητας θα πρέπει να έχει ευρέως συντονίσιμη, σταθερή έξοδο και ικανότητα να λειτουργεί με περιορισμένους παλμούς ns Fourier, αλλά οι συμβατικές ρυθμίσεις laser με αυτά τα χαρακτηριστικά είναι ογκώδεις, χρονοβόρες και δεν μπορούν να κλιμακωθούν.

Οι συγγραφείς προτείνουν μονολιθικούς συντονιστές διαμαντιού ως πηγή για πεδία laser μονής συχνότητας που πληρούν όλες τις απαιτήσεις για εφαρμογές υψηλής ακρίβειας. Ο συντονισμός της εξόδου Stokes του ενσωματωμένου αντηχείου διαμαντιού πραγματοποιείται μέσω ακριβούς ελέγχου θερμοκρασίας, ο οποίος είχε ως αποτέλεσμα ρυθμό μεταβολής

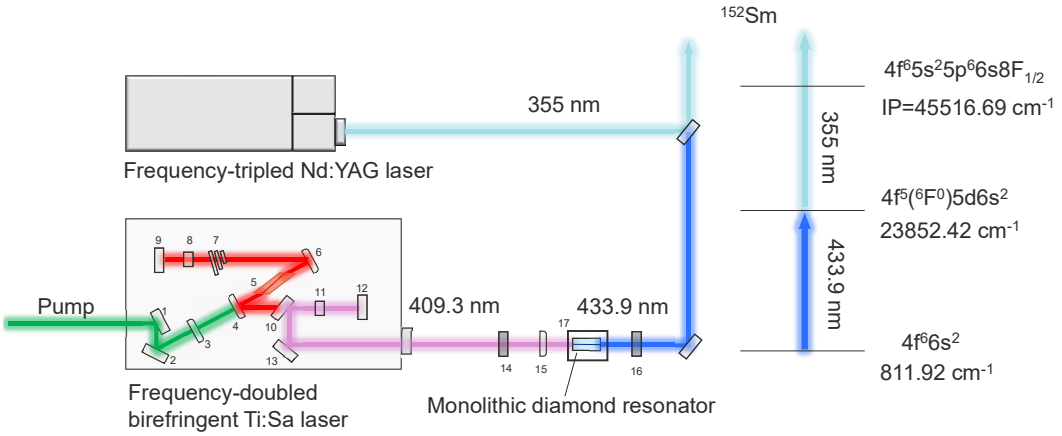

Σχήμα 13: Οπτική ρύθμιση για το πείραμα. Το Stokes laser καθοδηγείται στην κάθετη κατεύθυνση του PI-LIST ενώ το Nd:YAG laser στην παράλληλη. 1, 2, 9, 12, 13: καθρέφτες. 3, 15: φακός εστίασης. 4, 6: κυρτός καθρέφτης. 5: κρύσταλλος Ti:Sa. 7, 8: φασματικά φίλτρα. 10: διχρωμικός καθρέφτης. 11: κρύσταλλος διπλασιασμού. 14, 18: half wave plate HWP. 17: ελεγκτής θερμοκρασίας.

$\frac{\partial \nu_S}{\partial T} \approx 3GHz/K$ σε μήκος κύματος 479 nm και θερμοκρασία 300 K. Η σταθερότητα του συστήματος επιτεύχθηκε επίσης μέσω ελέγχου θερμοκρασίας, με αποτέλεσμα σταθερότητα καλύτερη από < 52 MHz RMS όταν μετρήθηκε για 16 ώρες.

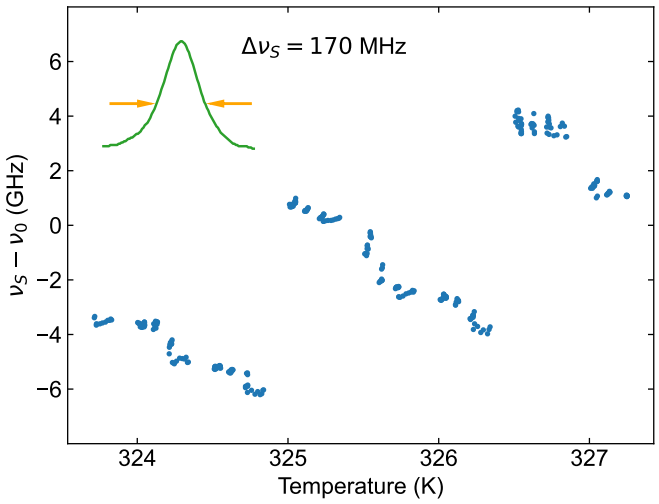

Σχήμα 14: Αποσυντονισμός κεντρικής συχνότητας Stokes με θερμοκρασία. Ένθετο: Φάσμα εξόδου Stokes με FWHM $\Delta\nu_S = 170$ MHz.

Με τη λειτουργία του μονολιθικού συντονιστή διαμαντιού σε καθεστώς διπλού συντονισμού, αποδείχθηκε μείωση του εύρους γραμμής μεγαλύτερη από ×3, υποδεικνύοντας ότι η χρήση δύο μεθόδων συντονισμού, όπως η θερμοκρασία και η γωνία έγχυσης της αντλίας, μπορεί ενδεχομένως να επιτρέψει τη βέλτιστη φασματική απόδοση. Οι συγγραφείς απέδειξαν επίσης την καταλληλότητα του μονολιθικού αντηχείου διαμαντιού για φασματοσκοπία υψηλής ανάλυσης σαρώνοντας το φασματικό προφίλ της βασικής κατάστασης των ^{152}Sm, με αποτέλεσμα μια κορυφή με FWHM 0.51 GHz.

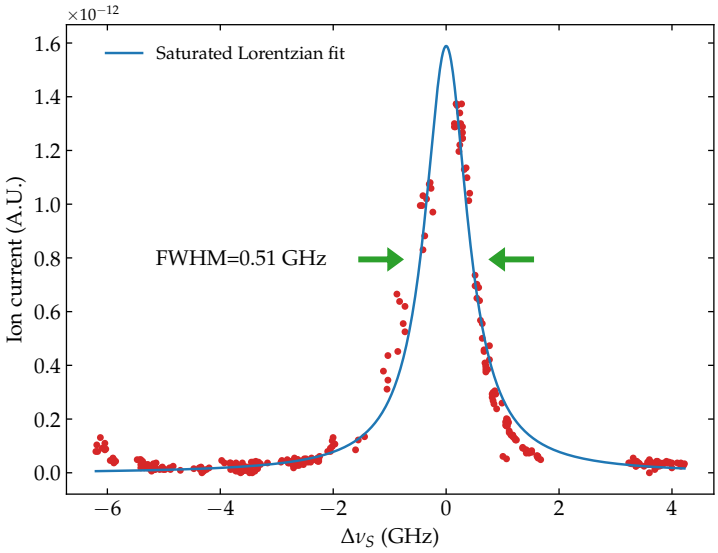

Σχήμα 15: Ρεύμα ιόντων ως συνάρτηση της κεντρικής συχνότητας Stokes με προσαρμογη σε κορεσμένη Lorentzian με FWHM 0.51 GHz.

Abstract

Tunable and spectrally pure lasers at visible wavelengths are key tools for many applications in physics, metrology and quantum technology. Integrating these laser sources on wafer-scaled devices is necessary for scaling the technology, allowing for powerful quantum tools. Current implementations however, are composed by complex, bulky systems that are in no way suitable to be used in the mentioned applications. To tackle this, we propose monolithic diamond Raman resonators as scalable, tunable, single-frequency laser sources. In these resonators, lasing happens through stimulated Raman scattering, which under certain conditions allows for the production of narrow-linewidth Stokes laser fields. Diamond-bulk temperature changes are used here to tune the Stokes center frequency and a model is developed to predict its performance. Moreover the rate of change of the Stokes center frequency with temperature allows for precise measurements of the thermo-optic coefficient of diamond, and also shines light on the temperature-dependent average phonon frequency of the material. Furthermore, when pumped by single mode lasers, we study the periodic narrowing of the single-mode profile of the output laser due to double resonance which is modeled and analysed. Lastly, we demonstrate its use for high-resolution spectroscopy showing an achieved spectral resolution of 0.51 GHz, establishing its suitability for precise measurements and ion excitation, and paving the way for a scalable photonic source for quantum technology applications.

Statement

This thesis is based on four papers, three published and one under review, where the author of this thesis stands as main author or co-author. The three papers describe the effects of temperature on the single longitudinal mode laser fields of monolithic diamond Raman resonators, while the fourth one deals with a high-resolution spectroscopy demonstration using these resonators. These papers are:

1. Tunable spectral squeezers based on monolithically integrated diamond Raman resonators [3], published in Applied Physics Letters, vol. 120, issue 15, p. 151101 (2022).

2. Influence of phonon harmonicity on spectrally pure resonant Stokes fields [6] published in Physical Review A, vol. 106, p. 023504 (2022).

3. Spectral purification of single-frequency Stokes pulses in doubly resonant integrated diamond resonators [5] published in Optics Letters, vol. 47, issue 16, p. 3976 (2022).

4. High-resolution demonstration in PI-LIST (in preparation).

The first paper is discussed in section 4.1 and the author's contribution was focused on the development of the numerical model of the article that is described in appendix B. The second paper is described in section 4.2. The author contributed to the assembly of the experimental setup, to the data acquisition system, and to the analysis and modeling of the data, while also contributing in the manuscript. Lastly, the third paper is discussed in section 5.2. The author's contribution included assembling the experimental setup, setting the data acquisition, while also analysing and modeling the data.

Finally, the thesis is also based on a high resolution spectroscopy demonstration where the monolithic diamond resonator is used. The author contributed in the experimental setup and setting the data acquisition system and analysing and modeling the data. At the same time, a manuscript is in progress.

Acknowledgements

This work and all the efforts behind it would not be possible without the help, support and knowledge of Dr. Granados. I am deeply indebted to him for the hours he dedicated teaching and educating me as an aspiring scientist and a person. Hopefully the excellent results helped me obtain can be considered a small repayment.

Additionally, this work would not be possible without the support of the RILIS team, offering their support and expertise whenever it was needed. I would like to express my deepest gratitude to the team for dedicating their time to develop my skills and contributing in my scientific career.

Furthermore, I could not have undertaken this journey without Dr. Vlastou from my home institute, the National Technical University of Athens. Her support and counselling have been a much needed assistance throughout the completion of this work.

Last but not least, I would like to extend my sincere thanks to my closest friends, colleagues and family. Special thanks goes to my partner for supporting me on my academic career and encouraging me to overcome the difficulties and achieve the best results possible.

Contents

List of Figures

Chapter 1

Introduction

1.1 Spectrally narrow lasers

Laser light differentiates from other light sources due to its four basic features which are monochromaticity, directionality, coherence and high brightness. In general, the spectral composition of a laser can vary depending on the requirements imposed by its manufacturers and users. Naturally however, the most sensitive applications require laser sources with the purest possible spectrum. Such spectrally pure sources are commonly referred to as single-longitudinal-mode (SLM) or single-frequency or narrow-linewidth lasers. As their name suggests, their defining feature is that they operate on a single resonator mode, emitting quasi-monochromatic radiation of very narrow linewidth. Narrow-linewidth lasers are characterised by low phase and intensity noise while also offering stabilised output center frequency. A visual approach to tell apart the spectrum of a SLM laser from the spectrum of a multimode laser can be seen in Fig. 1.1. In this figure, it is important to note that the FWHM linewidth of a multimode laser $\Delta\omega_m$ is much larger than the linewidth of its SLM counterpart $\Delta\omega_s$ ($\Delta\omega_m >> \Delta\omega_s$).

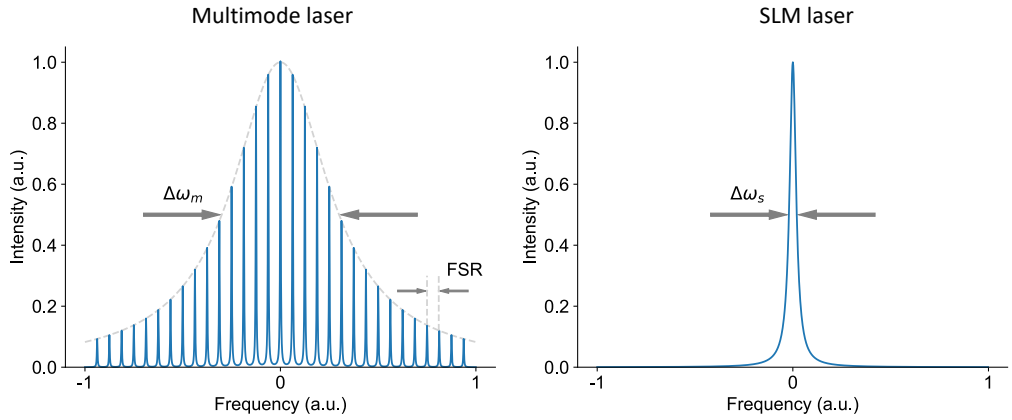

FIGURE 1.1: Example of the spectral profile of a multimode (left) and a SLM laser (right).

Due to these features, single-frequency lasers have a pivotal role in high-sensitivity applications. Their narrow linewidth can drive applications like atomic clocks [7], matter and anti-matter cooling [8] and ion trapping and manipulation [9] which can be used in quantum computing and quantum memories. Moreover, the spectral characteristics of such laser sources allow for great selectivity in terms of energy and as a result they are crucial for high-resolution spectroscopy that is mainly limited by the laser linewidth. As a result, spectroscopy of radioactive elements can be performed [10], enabling hyperfine structure studies and isotope-shift measurements,

which infer information about the nucleus, like spin, electro-magnetic moments and shape. Finally, SLM lasers allow for advanced LIDAR systems [11], that can perform simultaneous range and velocity measurements using quantum effects.

Besides the single-frequency output, these demanding applications also require other functional features like operation in a wide spectral range and as a consequence they need a widely tunable output. Furthermore, since most of these applications involve light-atom interaction, ns-pulses are needed to ensure the necessary intensity levels. It is important then, to consider the state-of-the-art and study how the requirements on ns-pulsed narrow-linewidth laser sources are met today.

1.2 Current SLM implementations

Even though single-frequency lasers in the nanosecond regime are not easy to implement, there are some notable approaches worth mentioning. We start by discussing the use of fiber lasers as a means to produce narrow-linewidth nanosecond pulses [12].This was achieved by following two different approaches, one based on an all-fiber active Q-switched cavity and one based on a modulated single-frequency continuous-wave fiber laser. Both approaches though, used single-mode phosphate fibers, highly doped with Er/Yb. The achieved results composed of Fourier-limited nanosecond pulses at 1550 nm with power more than 50 kW. The demonstrated FWHM linewidth was 35 MHz which corresponds to the Fourier-limit of a 20 ns pulse. In Fig. 1.2 a graphic representation of the Q-switched approach can be seen.

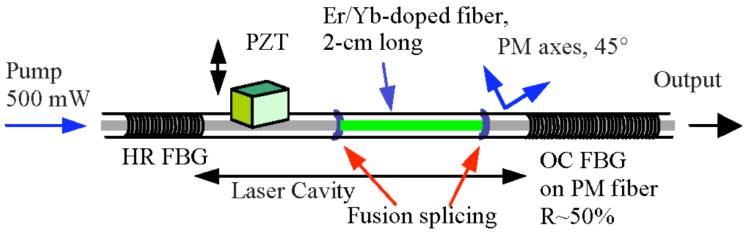

FIGURE 1.2: Graphic representation of an active Q-switched all-fiber laser with a piezoelectric actuator (PZT), operating at 1550 nm. [12]

Continuing, another important approach to SLM laser fields in the ns-pulsed regime comes from injection-locked VCSELs (Vertical Cavity Surface Emitting Laser) [13]. Using a setup similar to the one depicted in Fig. 1.3 they achieved ns-pulses of different durations with linewidths up to hundreds of MHz.

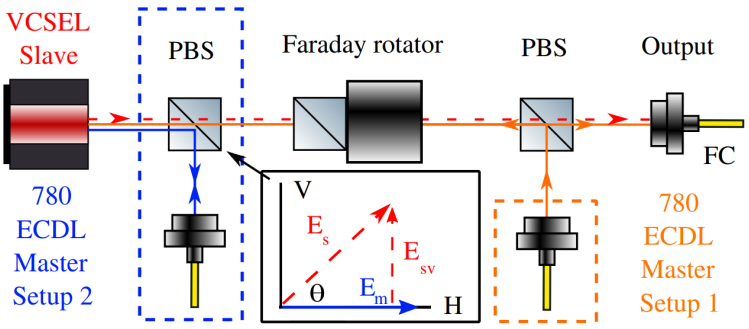

FIGURE 1.3: Diagram of an injection-locked VCSEL with two external cavity diode laser (ECDL). [13]

Last but not least, Fourier-limited nanosecond-pulses have been achieved through injection-locking Ti:Sapphire lasers [14]. By seeding a ring cavity Ti:Sa laser with a continuous-wave (CW), single-frequency operation was achieved with a linewidth smaller than 30 MHz at 532 nm and ouput power at 1.4 W. The experimental setup producing the laser field can be seen in Fig. 1.4.

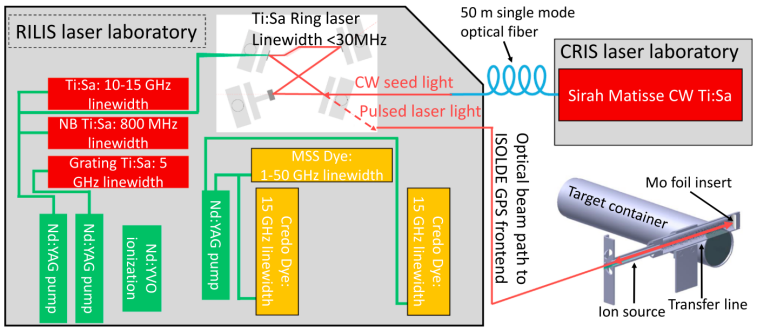

FIGURE 1.4: Graphical representation of an injection-locked Ti:Sa laser. [14]

Moving forward, after presenting some of the available implementations for Fourier-limited ns-pulsed laser sources, it is important to examine their shortcomings in respect to modern demands.

1.3 Limitations of SLM sources

In general, the state-of-the-art is quite capable on producing narrow-linewidth laser fields. However, despite the fact that we presented some ns-pulsed single-frequency lasers, there is actually a market gap that is characterised by a lack of variety for such lasers [2]. Additionally, the aforementioned approaches are usually bulky systems that are complicated and time and money-costly to work with.

In addition to that, applications like the ones mentioned above, besides single-frequency output (in the kHz to hundreds of MHz linewidth) in the ns regime, require a laser source that is also widely-tunable, stable and power-tolerant. It can be understood then, that adding these capabilities to the lasers mentioned in section 1.2 would further increase complexity and would make the laser even more difficult to work with.

Usually these disadvantages are not detrimental for research and industry. However with the recent progress in quantum sensing and technology, there is a need for scaling the sate-of-the-art in order to achieve greater capabilities. As a consequence this would require scalable laser systems as well, rising the need for novel laser sources that combine the aforementioned features while maintaining scalability. Wafer-scale, coherent light sources are equivalent to the diminution of the transistor and have the potential to pave the way to scalable quantum computing in room temperature conditions, revolutionising technology and inducing a paradigm-shift similar to the one brought by computers.

Due to the necessity surrounding such coherent laser sources, this thesis was centered around research done on a monolithic diamond Raman resonator that emits a single-frequency laser field. The narrow-linewidth laser field was generated by stimulated Raman scattering (SRS) inside a mm-long diamond bulk. The laser system had great stability and offered precise tunability capabilities while emitting ns-pulses. Due to its monolithic design and small length, this innovative resonator is

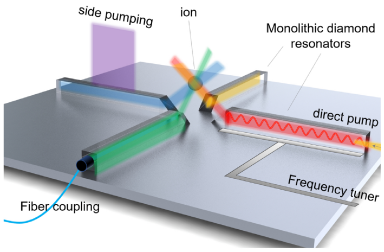

FIGURE 1.5: Monolithic diamond Raman resonators used on-chip for laser-ion manipulation [2].

considered a great candidate for coherent, on-chip laser sources for scaling applications like the aforementioned ones. In Fig. 1.5, we can see an example of how such a monolithic diamond resonator can be integrated on-chip for ion manipulation.

To start our study, first we discuss about the Raman effect and its use as a lasing method in integrated photonics. Then we proceed to analyse single-frequency operation and tuning of the monolithic diamond resonator. We examine thoroughly thermal effects on the integrated diamond resonator, and we develop a precise model for its response with temperature changes. Lastly we use the results of the previous studies to conduct a demonstration of high resolution spectroscopy using the diamond bulk, showing that it's suitable to be used in ion-manipulation applications.

Chapter 2

Raman lasers

In this chapter, we are going to examine the physics of the Raman effect, explaining the dynamics behind this scattering phenomenon. After establishing its working principle, we are going to elaborate on the idea of stimulating the scattering process, resulting in a laser beam through stimulated Raman scattering (SRS). After a brief discussion about its advantages over stimulated emission, we review the existing implementations of diamond Raman lasers with a scope on the integrated approaches.

2.1 Raman effect

As it was mentioned above, the first step for this study is to understand how and why SRS is used for integrated lasers and for this purpose it is important to discuss the Raman effect. This effect is one of the four basic scattering effects that take place during the propagation of light in matter with the other ones being Rayleigh, Mie and Brillouin scattering. Rayleigh and Mie scattering are categorised as elastic and Brillouin and Raman scattering as inelastic. In contrast to their elastic counterparts, Brillouin and Raman scattering involve loss of energy during the process. A simple explanation of the inelastic process in the above two regimes goes as follows: as light goes through a transparent material, it is partially absorbed and emitted back by the material, with some of the energy of the photon being retained by the lattice of the material.

The two inelastic effects are very similar in the underlying physics governing them, both being inelastic processes due to phonon absorption. Focusing on Raman scattering, the photons get absorbed by a material and excite its lattice to a virtual energy level. The lattice then de-excites to a higher energy level than before the absorption, emitting a photon of reduced energy which is called a Stokes photon. The energy relationship relating incident E_{inc} and Stokes E_S photon with the absorbed energy E_{abs} is:

$$E_{inc} - E_S = E_{abs} \tag{2.1}$$

The absorbed energy that stays in the lattice takes the form of vibrational modes, also known as phonons. In Fig. 2.1 we can see a graphical depiction of the described effect.

The main difference between Raman and Brillouin scattering lays in which lattice structure vibrates. In Brillouin scattering, the absorption happens by large scale lattice structures with acoustic phonons of very low frequencies. On the other hand, Raman scattering is happening through vibrational and rotational excitations in the bonds of neighbouring atoms. The result is that Raman scattering induces much

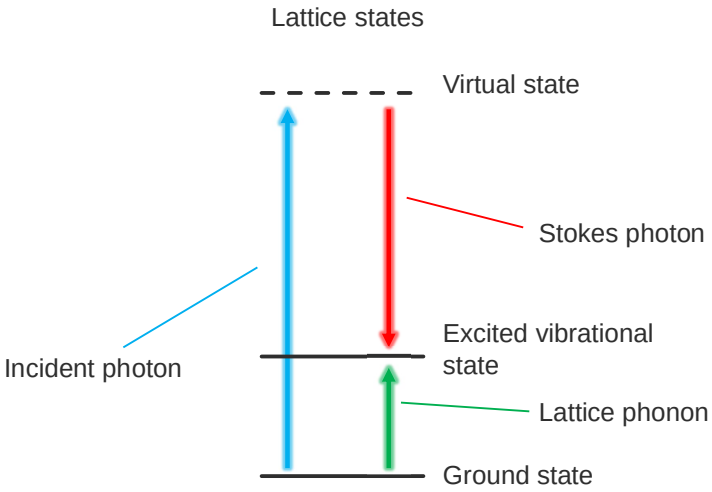

FIGURE 2.1: An incident photon gets absorbed by the lattice, exiting it to a virtual state which then de-excites to vibrational energy level emitting a Stokes photon of lower frequency.

larger frequency shifts on the incident light than Brillouin scattering, creating infrared optical photons.

Historically, the phonon absorption effect was first theoretically predicted by Adolf Smekal in 1923. C. V. Raman however, first observed the effect, inspired by the work of Arthur Compton on the nature of light and the discovery of the Compton effect. Compton won the Nobel Prize in 1927 for the observation that X-rays can inelastically interact with atoms, giving them a portion of their energy. Raman's idea was that X-ray inelastic scattering can also be applied to optical wavelengths, which earned him the Nobel Prize in 1930 for proving it.

The Raman effect, since its discovery, has found wide applications in spectroscopy for chemical analysis of materials. It can be used for solids, liquids, gases and even biological tissue. By detecting the Raman phonon shift of a molecule or lattice, it is possible to determine the excited vibrational modes, leading to an identification method for substances. This effect is characterised by versatility since it can be used with infrared, visible, ultraviolet and even X-ray light sources.

2.2 Stimulated Raman scattering

As established above, the effect Raman is an absorption-emission process happening spontaneously with a rate given by the appropriate probability factors. With the development of quantum mechanics however, Albert Einstein suggested the idea of a different emission mechanism, happening at a much higher rate than the spontaneous one. It was named stimulated emission and it required the presence of a photon with energy E_{ph} equal to the energy that would be emitted during spontaneous emission.

It is possible to apply these principles to the Raman effect, by stimulating the scattering process. By applying strong pump fields, we can eventually reach a threshold where the spontaneous Stokes light can actually stimulate the emission of more

Stokes light, attaining the lasing characteristics, like coherence, directionality, monochromaticity and high brightness. The result is the effect called stimulated Raman scattering (SRS) which produces Stokes laser fields. In Fig. 2.2 we can see how SRS differs from Raman scattering.

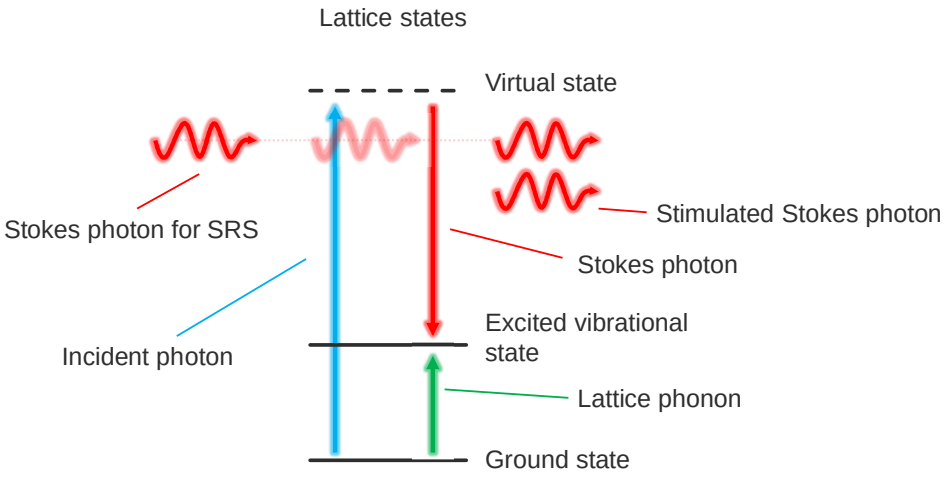

FIGURE 2.2: Graphical depiction of stimulated Raman scattering where a pre-existing Stokes photon stimulates the scattering process.

As we can see in Fig. 2.2, Stokes photons are created by the scattering of pump photons. This means that increasing the number of pump photons and therefore increasing the pump intensity I_p will immediately increase the scattering events and as a result the Stokes laser intensity I_S showing the dependence between two beams. In order to describe both beam intensities, a system of differential equations is needed, since the Raman laser signal follows the fluctuations in the population of both pump and Stokes photons:

$$\begin{cases} \frac{dI_S}{dx} = g_R I_p I_S - a I_s \\ \frac{dI_p}{dx} = -\frac{\omega_p}{\omega_S} g_R I_p I_S - a I_p \end{cases} \tag{2.2}$$

were ω_p and ω_S are the pump and Stokes frequencies respectively, g_R is the Raman gain and a the loss coefficient [15].

In this system of equations, we have made an important assumption which limits the influence of SRS on the lasing process. The assumption is that, the Stokes field is not strong enough to create cascaded Stokes laser beams. In reality, when it reaches a threshold intensity level, it can indeed act as a secondary pump, generating its own Stokes laser. The cascading process is only limited by the available energy and intensity, and it can keep happening as long as the appropriate conditions are satisfied. Of course in the cascading regime the system of equations will have to change accordingly, adding the 2^{nd}, 3^{rd}... n^{th} Stokes terms.

Continuing, SRS is characterised by a fundamental difference in comparison to its population inversion counterparts. The Raman effect doesn't involve any real energy levels since the pump energy is mediated to the Stokes field only through the pump's propagation. This comes with great advantages for the spectrum of a Raman laser for several reasons which will be examined below.

As stated above, the Raman process happens through virtual energy states. The key property here is that these energy states can take any arbitrary value without

quantum limitations that typically appear in other lasing mechanisms. These quantum limitations usually arise by the quantised nature of real energy levels in atoms and molecules, limiting the potential transitions and therefore limiting the achievable wavelengths. It becomes clear then, that no wavelengths are prohibited for SRS, as long as the pump and the Raman medium transparency allow for it. Because of this property, Raman lasers are tested to be used in combination with the great frequency range of Ti:Sapphire lasers, so that exotic parts of the optical spectrum can become accessible without of complicated laser systems [16].

Another advantage Stokes laser fields have over their population inversion counterparts concerns the spatial hole burning effect. In inversion lasers, the energy is stored in the atoms of the gain medium, through excitement to higher states and leading to population inversion of the ions, and is depleted following the spatial wave pattern of the resonating light. The resulting gain distribution along the lasing medium length, is a wave-like formation with a wavelength similar to the one of the laser output. This effect is called spatial hole burning and it results in secondary lasing longitudinal modes, competing over the available gain energy with the main mode and as a result making single frequency operation difficult. SRS on the other hand doesn't rely on energy storage since no real energy levels are required but is rather mediated through the propagation of the pump field. As a result, gain depletion has a homogeneous profile and thus it's not subjected to spatial hole burning or axial mode competition [17] and therefore the spectral output consists of an intrinsically stable frequency light. These dynamics can be seen in Fig. 2.3.

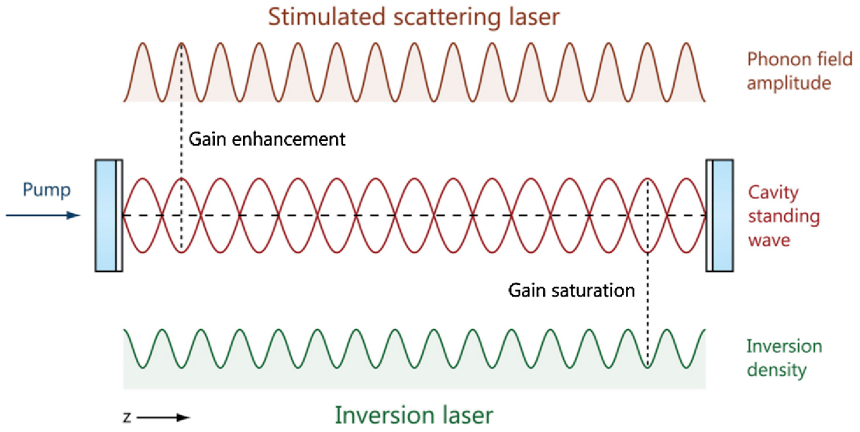

FIGURE 2.3: In population inversion lasers, the gain of the material (bottom) depletes on the anti-nodes of the laser (middle) leading to mode competition. In SHB-free gain, the phonon field (top) is maximal in the anti-nodes, amplifying mainly the main mode. [18]

Considering the variety of SRS advantages, it is natural to expect implementation of this phenomenon in laser systems. Usually, integration of the Raman-active medium takes place either on an optical fiber or by a bulk crystal, with most common methods including gases.

Optical fiber Raman lasers, are characterised by long interaction lengths between pump and gain medium. The gain threshold for lasing therefore, tends to be very low, making continuous wave CW operation easily accessible. This is attributed to the fact that for the same average power, pulsed lasers have much higher peak power than continuous pumps and can reach the high lasing threshold. For low threshold however, even a continuous pump is enough, ensuring a continuous output. Besides CW operation, fiber lasers can also offer wavelength selectivity. Through the use of

a fiber Bragg grating, we can significantly reduce the emission bandwidth, obtaining great spectral features, even though single longitudinal mode operation is not easily feasible due to nonlinear interactions.

When in comes to bulk crystal Raman lasers, there are both intractivity and external cavity approaches for the Raman conversion. In these resonators, the gain crystal is usually centimeters long, much shorter than their optical fiber counterparts, resulting in a high lasing threshold. For this reason they are usually operated in the ps and fs-pulsed regime. An exception to the high threshold can be seen in low loss cavities, where CW operation is achievable [19]. Single crystal Raman lasers can also incorporate other nonlinear processes inside the lasing cavity, like adding a doubling crystal for second harmonic generation etc. [20] for further wavelength diversification.

Raman lasers have a variety of applications, from spectroscopy to quantum computing. A very notable one is their use in astronomy. Modern astronomical telescopes have great sensitivity and detection potential due to huge mirrors and high surface quality. It is understood then that the optics used in these telescopes are no longer a bottleneck in the resolution capabilities but it is rather the atmosphere itself, distorting the captured images. Space based telescopes can bypass this issue, but they can never be as big and precise as earth based ones and thus this problem requires solving.

In order to tackle this issue, appropriate calibration is required. Either Q-switched neodymium based Raman lasers or fiber Raman lasers are employed and focused on a set spot at a high altitude. The atmospheric air gets ionised on that spot and ends up emitting a light signal, similar to a virtual stellar object. Since the characteristics of the virtual object are known, calibration to the atmosphere's disturbances becomes possible, allowing even greater resolution. In Fig. 2.4 we can see this system being used in the European southern observatory (ESO).

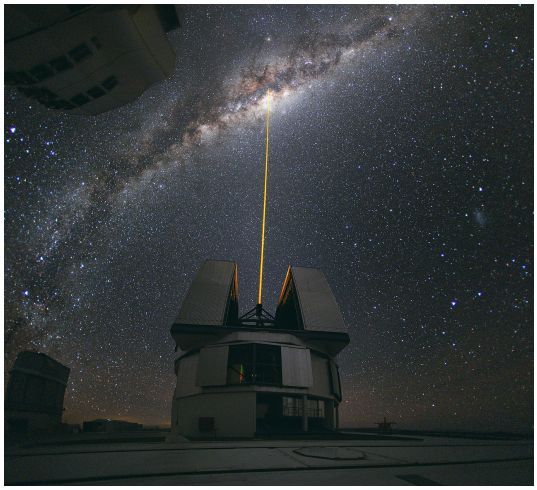

FIGURE 2.4: Raman laser guide star system using a sodium crystal, operating at 589 nm [21]

The applications of Raman lasers, can be further broadened by the production single-frequency laser fields [22]. SLM lasers unlock the way for atom cooling, atomic clocks and high resolution spectroscopy. Using diamond as the Raman active medium, SLM Stokes fields have been used to successfully demonstrate their suitability in LIDAR systems [23]. Lux et al. used a stable, tunable, single-frequency Raman laser to detect water vapors in the atmosphere, which play a significant role in

global warming. The experimental setup can be seen in Fig. 2.5. The laser beam had a central frequency from 1483 to 1488 nm and a frequency stability of 40 MHz without active stabilization. The achieved FWHM of the spectral profile was 4.5 GHz.

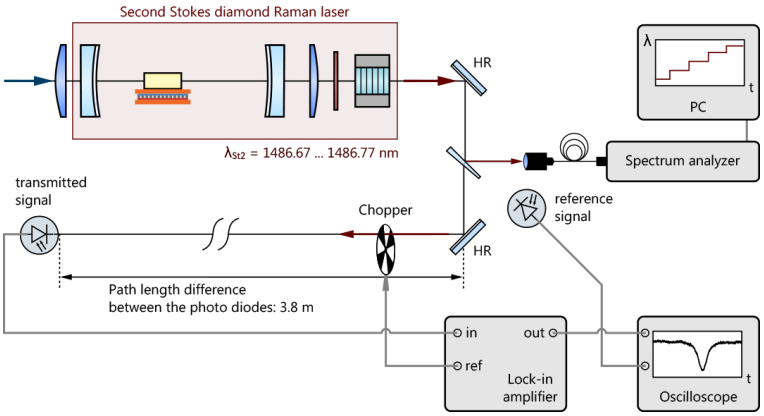

FIGURE 2.5: Water vapor detection system, using a SLM Raman laser [23].

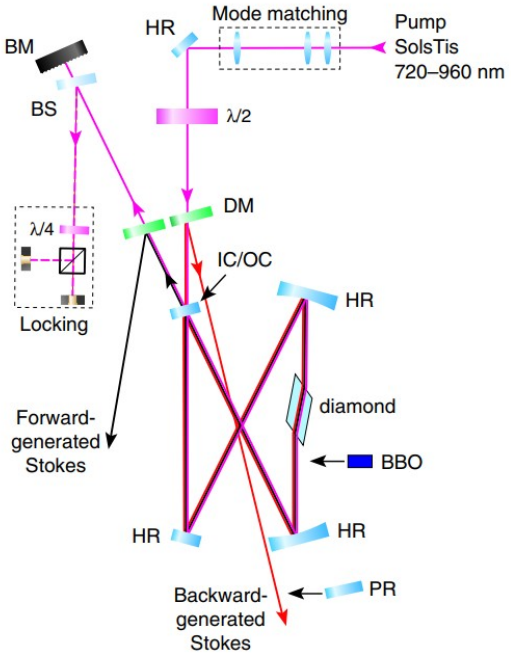

FIGURE 2.6: Ring diamond Raman laser [24].

Another great demonstration was the generation of SLM Raman in a diamond crystal, using a ring resonator that can be seen in Fig.2.6 [24]. Their main aspiration was, using the Raman effect, to extend the wavelength emission of titanium sapphire (Ti:Sa) lasers. This is important because due to Ti:Sa's role in spectroscopy since it's the most widely tunable laser so far. The emission range is between 650 to 1050 nm while in combination with the Raman effect it could reach up to 1220 nm. The Stokes cascading process would also extend the range to an astounding 1450 nm making it an indisputable tool.

Besides their spectral reach properties, SLM diamond Raman lasers appeal also in high power applications. Using diamond's properties Yang et al. [22] were able to pump the Raman crystal with a Nd:YAG laser operating at an astounding power

of 321 W. This resulted in a Stokes laser of 38 W at 620 nm and through a doubling crystal they got 11.8 W at 1240 nm. These performance characteristics in combination with the above advantages can eventually make diamond Raman lasers a go to solution for problems where high power and excellent spectral features are required.

2.3 Integrated photonics

Raman lasers have shown to have many benefits, playing an important role in a plethora of applications. All the advantages of these lasers however, are shown inside sensitive and bulky cavities which is in contrast with the current flow of progress: integration and scaling of devices. Achieving these two objectives is a crucial landmark for Raman lasers, since they could combine all the cited capabilities, like single-frequency emission, stability, tunability and even great power yield in a scalable, ready to be used device. Needless to say, this would be an excellent tool, extending current capabilities and realizing applications only theoretically speculated so far.

The Raman laser integration process started by using silicon as the Raman-active medium [25]. Silicon was the material of choice because of the preexisting research and use on passive photonic devices. Boyraz et al. wanted to design an active photonic device, namely a laser system. They realized that silicon's large Raman gain, made it a great material for use in an integrated waveguide, since it was enough to allow lasing, despite the waveguide's limited length.

One of the main challenges silicon lasers faced, was the two photons absorption (TPA) effect. This is a nonlinear process where two pump photons are absorbed simultaneously sending lattice elements to an excited state. TPA competes with the Raman effect for the available gain but also creates further secondary competing effects. In a semiconductor such as silicon, TPA can generate free carries which then allow for extra absorption phenomena. Free carrier absorption (FCA) results in an intraband transitions of the carriers which, combined with TPA has detrimental effects on SRS since they lower the effective gain, significantly increasing the required lasing threshold and thus rendering CW operation impossible.

Along with TPA, silicon has a limited transparency range which negates one of the most important advantages of Raman scattering and its low thermal conductivity doesn't permit high power operation. This leads us to the idea that is not one of the main candidates for efficient SRS. By considering Table 2.1, a very interesting Raman-active crystal is diamond which can overshadows silicon in more than one ways. First of all, diamond, is subject to both TPA and FCA which could potentially reduce the effective gain. However, unlike silicon, diamond only starts showing these effects under deep ultraviolet radiation. Even in that regime though, it has been shown that efficient lasing is possible [26] since the Raman gain of diamond significantly increases as wavelength decreases.

Furthermore, as we have stated above, one of the important advantages SRS has over other lasing mechanisms, is the absence of any limitations in terms of output wavelength due to the operation through virtual states instead of real ones. Any wavelength is attainable under the presence of the appropriate pump wavelength and transparency of the material. For this reason, diamond is a great Raman laser material due to its hyper-broad transparency range. It starts from the deep ultraviolet and reaches the far infrared with an exception between 2.6-6 μm due to multiphonon-induced absorption [31]. In comparison, silicon extends from the near infrared to the far infrared, significantly reducing the available wavelength range.

TABLE 2.1: Characteristics of Raman crystaline materials like Raman shift ω_R, Raman gain g_0 (at 532 nm), Raman linewidth $\Delta\omega_R$ (HWHM) and transparency range T.R..

Material	$\omega_R\ (cm^{-1})$	$g_0\ (cm/GW)$	$\Delta\omega_R\ (GHz)$	*T.R.*
Diamond [27]	1332	40	22	DUV-FIR
Silicon [28, 25]	520.2	$3.7 \cdot 10^{-8}$	50	NIR-FIR
KGW [29]	768	11.8	96	UV-MWIR
$BaWO_4$ [30]	926.5	27.1	24.1	DUV-MWIR
$Ba(NO_3)_2$ [29]	1047	47	6	UV-NIR

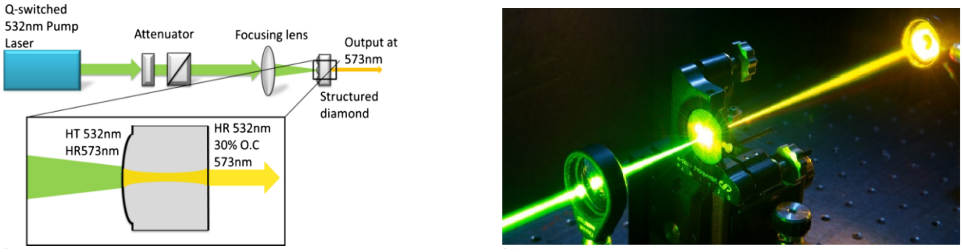

FIGURE 2.7: Diagram of the optical setup and demonstration used in [33].

The spectral bandwidth capabilities of a diamond Raman laser are further increased due to its giant Raman shift, which has been measured to be 1332 cm^{-1} at 0 K. The advantage of this can be easily understood in terms of using the Raman converter as an extension to a laser with a wide emission spectrum, like a Ti:Sa. Its spectrum is between 650 to 1180 nm and with the addition of non-linear crystals, that show sum frequency generation (SFG) capabilities, it can reach lower wavelengths, with certain gaps. The Raman laser extension can extend the range, up to 1400 nm and through SFG, completely fill these spectral gaps.

All the aforementioned characteristics, render diamond an ideal Raman-active crystal. Indeed, SRS in diamond has been achieved successfully in the pulsed regime using a ring cavity [32]. It became known then, that diamond was a suitable material for that, offering a pump to Stokes conversion efficiency similar to other crystals. This demonstration was soon followed by attempts to integrate diamond Raman resonators into a monolithic device. Sean at al. [33] finally achieved creating the first integrated diamond Raman laser.

The monolithic resonator was pumped by a Q-switched laser at 532 nm which went through an attenuation and focusing optical system before being guided on the resonator itself. The monolithic cavity had an etched microlens on its injection edge, which further focused the pump beam. The resonator resulted in a 573 nm Stokes field with output energy of 3.7 μJ. The setup used in the experiment is shown in Fig. 2.7 along with a demonstration photograph.

The next step was full on-chip integration of the resonators. Taking advantage of diamond's characteristics, Latawiec et al. [1] created the first CW, on-chip diamond Raman laser, integrated on a silicon chip. The laser had tunability properties over the bandwidth of 100 nm with its center wavelength at 2 μm. The Raman medium was implemented in the form of a waveguide, rendering CW operation possible (Fig. 2.8. In this setup, tunability was achieved by changing the pump frequency either

in a coarse way, due to mode hopping or through a finer way within thermally red shifted pump resonances.

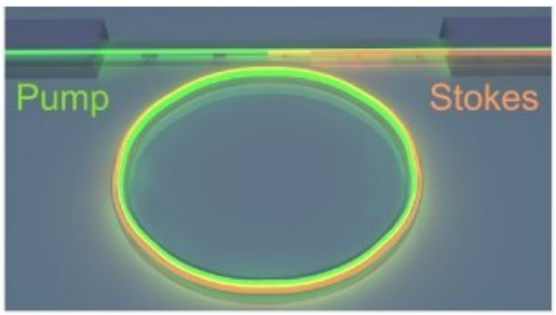

FIGURE 2.8: Integrated waveguide for CW, on-chip, diamond Raman laser [1].

These achievements lead to the nomination of diamond not only as a prominent material for Raman lasing but also as a protagonist in integrated photonics. The creation of on-chip Raman lasers has the potential to revolutionise major aspects of technical methodology, allowing for scalable systems in harsh environments for LIDAR or spectroscopy measurements where compactness and sturdiness are critical.

The presented integrated diamond Raman lasers, despite their innovations, didn't promote SRS's spectral advantages and were only steps to the realization of single-frequency, integrated diamond Raman resonators. In this work, we show the use of a bulk diamond resonator in a Fabry-Pérot configuration, as a source of finely tunable, narrow-linewidth, ns-pulsed Stokes fields, taking the field of on-chip Raman lasers one step further.

Chapter 3

The Fabry-Pérot diamond resonator

In this chapter we are going to focus on the technical aspects of the integrated diamond Raman resonator. We start by analysing the benefits of using diamond as a medium for monolithic Raman lasers and the ways it allows for optimal operation. We continue by elaborating on the details of the resonators parameters and how they are adjusted for efficient lasing. Then we explain the mechanism behind SLM operation and lastly we present an overview of how the single-frequency output can be tuned without increasing the complexity of the system.

3.1 Diamond for a monolithic resonator

Diamond has been an intriguing material for civilization since its discovery, having a role in many different domains, from luxury items to industry. As we have seen in the previous chapter, diamond has also applications in optics, while today it stands under the focus of researchers as a novel and revolutionising photonics material. This is due to its extraordinary mechanical and optical properties, compared to other materials, which we will examine in the following paragraphs.

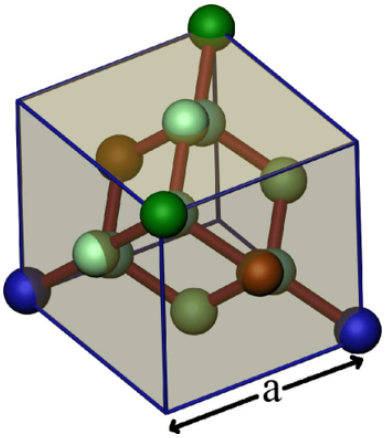

FIGURE 3.1: Diamond lattice [34].

Besides diamond's properties as a Raman-active material, it is a great resource of monolithic laser resonators. Firstly, diamond exhibits great thermal properties which is important because it ensures durability and spectral stability. Starting by it's low thermo-optic coefficient, which is in the order of $10^6\ K^{-1}$, dispersion relationships change much less than other materials for the same temperature shift. Its thermal expansion coefficient is also in the range of $10^6\ K^{-1}$ reinforcing the emission stability of the resonator. Continuing, diamond is a very prominent material

for high power applications due its large damage threshold. Diamond has an unsurpassed thermal conductivity of 1800 W/m/K at 300 K, ensuring no temperature accumulation which eventually causes damage even at kW ranges.

Last but not least, diamond's excellent spectral features and power tolerance are the effect of the near perfect symmetry in its lattice, which can be seen in Fig. 3.1. Along with the aforementioned properties, the symmetric lattice also has negligible birefringence and piezoelectric properties. For this reason, diamond as a lasing material allows for dispersion limited beam quality. As a result, considering all the properties that diamond combines, it becomes clear that it is an ideal material for high spectral quality, power-tolerant integrated Raman lasers.

3.2 Fabry-Pérot configuration

Despite diamond's exceptional characteristics, using it as a resonator demands focus on other aspects than just its opto-mechanical properties. In this work we are using the diamond bulk as a resonator, operating in a Fabry-Pérot (FP) configuration. A FP resonator typically consists of two mirrors parallel to each other, while the lasing medium rests between them. The monolithic diamond resonator in this configuration, consists of a single cuboid diamond crystal, built using CVD technology. Its two opposing flat surfaces, using the Fresnel reflectivity effect ($R_1, R_2 \approx 18\%$), play the role of the edge mirrors while the diamond bulk is the Raman-active medium. The FP resonator has dimensions of $6 \times 2 \times 2\ mm^3$ and its edge mirrors were polished to ensure a parallelism better than $0.5\ \mu m$/mm. Finally, the Raman conversion efficiency is heavily dependent on the diamond lattice orientation and in order to guarantee efficient operation the diamond bulk was plane-cut for propagation along the $\langle 100 \rangle$ crystallographic axi while the polarisation of the pump was parallel to the $\langle 111 \rangle$ axis

Generating SLM Stokes laser fields inside an integrated FP diamond resonator is nowhere near trivial, being in fact a delicate procedure that depends on many sensitive factors. One of the main concepts of a FP resonator that require understanding before establishing the operating principles of single-frequency operation, is the idea of free spectral range (FSR).

The concept of FSR is related to the existence of discreet laser wavelength outputs from a FP resonator. The reason for this phenomenon lies on the obvious fact that resonators need to actually resonate the lasing wavelength which results in standing electromagnetic waves inside the cavity. For a given optical length L_{eff}, the resonant condition can be expressed as follows:

$$q \cdot \frac{\lambda}{2} = L_{eff} \tag{3.1}$$

where q is an integer and λ the resonating wavelength. For a constant L_{eff}, we can see that there can be an infinite number of resonating frequencies as long as q remains integer. An important terminology note is that each q number represents a resonant longitudinal mode. Practically there can never be infinite modes because of the limitations set by the material's spectral amplification properties.

In order to achieve SLM operation, it is usefull to measure the spectral distance between the modes. Combining the fundamental equation $\lambda \cdot \nu = c$, where ν is the frequency of the wavelength and c the speed of light in vacuum, with eq. 3.1 we get that:

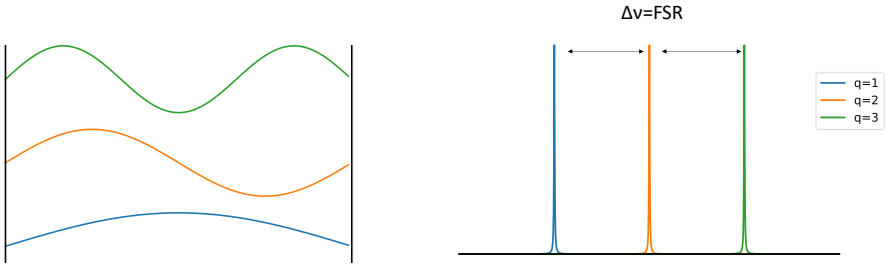

FIGURE 3.2: Resonating wavelength and frequency (left and right respectively) in a FP cavity

$$\nu = q \cdot \frac{c}{2L_{eff}} \tag{3.2}$$

and the mode spacing $\Delta\nu = FSR$ is found as:

$$FSR = \frac{c}{2L_{eff}} \tag{3.3}$$

3.3 SLM operation

After establishing a basic understanding for the FSR we are now ready to examine the idea of SLM emission. We start by considering a multimode pump field E_F with 2m+1 modes equally spaced in frequencies by a spectral distance Ω and a single-mode Stokes field E_S. These can be written as:

$$E_F \propto \sum_{l=-m}^{m} F_l e^{i\left(\omega_{F(l)}t - k_{F(l)}z\right)} \tag{3.4}$$

$$E_S \propto S_0 e^{i(\omega_S t - k_S z)} \tag{3.5}$$

where, F_l and S_0 are the complex amplitude of each field incorporating the real amplitude and phase while the k_i is the wavevector of the pump and the Stokes field. The term $\omega_{F(l)}$ is $\omega_{F(l)} = \omega_{F(0)} \pm \Omega l$ and it represents the different modes of the pump while ω_S the Stokes frequency.

Focusing on these two terms, the satisfying condition for single-mode operation is that every pump mode interacts with the appropriate Raman phonon in order to always give off the same Stokes frequency, which is mathematically written as:

$$\omega_{F(l)} = \omega_S + (\omega_R \pm \Omega l) \tag{3.6}$$

The term $\omega_R \pm \Omega l$ indicates a phonon that is slightly detuned from the center Raman phonon frequency in order to resonantly interact with the pump mode $\omega_{F(l)}$ while at the same time it is located within the Raman linewidth ($\Delta\omega_R > \omega_R \pm \Omega l$, $\forall l$). These dynamics are graphically depicted in Fig. 3.3

A notable remark is that, this process has a maximum efficiency when there is use of all the Raman phonons. This is achieved when the mode distribution of the pump covers the entire Raman spectrum with the ideal limit being $\Delta\omega_F = \Delta\omega_R$.

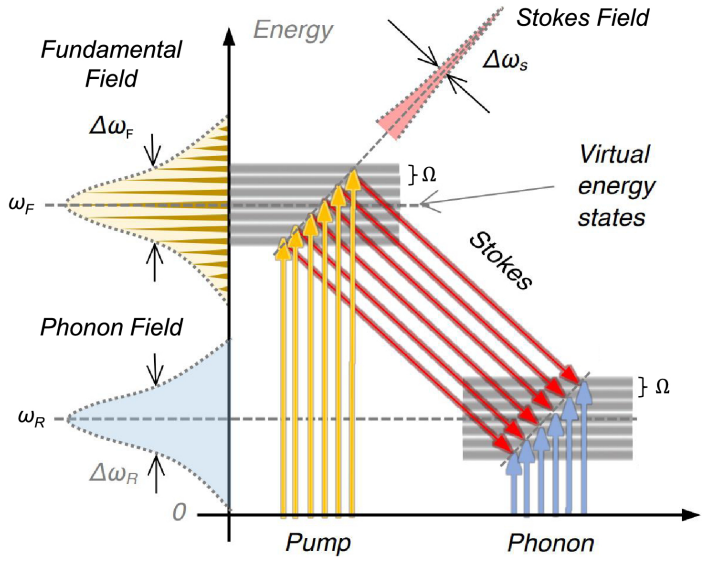

FIGURE 3.3: The pump modes virtually excite the lattice to different energies depending on the mode. The virtual energy states de-excite to the complementary phonons of each mode, emitting a monochromatic beam [2].

In general, fulfilling eq. 3.6 requires a mechanism that prohibits Stokes side modes from lasing, while mainly amplifying the central mode. This would usually require the use of spectral filtering systems, like etalons and birefringent filters, however in a Raman-active Fabry-Pérot resonator the filtering is integrated in the working principle. To understand this, we need to know that since SRS has no spatial hole burning, the gain is homogeneously depleted with most of it going to the main mode. As a result side modes are left with much less gain in comparison to the main mode. This process cascades with each round-trip of Stokes field, consequently creating a Raman-active etalon that predominantly amplifies the main mode and eliminates the side-modes.

After the established spectral filtering, the final step to achieve single-mode Stokes light is to guarantee the appropriate spacing for Stokes side-modes. This is done by selectively setting the FSR of the resonator so that it's larger than the effective gain linewidth:

$$FSR > \Delta\omega_g \tag{3.7}$$

Concerning eq. 3.7, the effective gain linewidth $\Delta\omega_g$ can be approximated by the convolution between the spectrum of the pump, and the natural Raman spectrum of diamond, with respective lineiwdths $\Delta\omega_p$ and $\Delta\omega_R$. Under the assumption of Lorentzian distributions for both natural Raman gain and pump spectrum, we get that $\Delta\omega_g$ is given by:

$$\Delta\omega_g = \Delta\omega_R + \Delta\omega_p \tag{3.8}$$

Given the fact that $\Delta\omega_R = 45$ GHz, it becomes obvious that we need great FSR values to fulfill eq. 3.7. Through quick calculations we find that $\Delta\omega_g$ is broad enough to require micro-scale resonators. The optical path length needs to be less than milimeters and at the same time $\Delta\omega_p$ needs to be as small as possible, meaning

CW operation is necessary. These approaches are rather unpractical since microresonators cannot be easily handled without the need of special equipment.

A solution to this issue lies in operating in the high Raman gain regime [35]. In order to explain what this is, we need first to understand how the Raman gain is calculated. In general the effective gain coefficient G_S is en exponential of the pump intensity I_0 [36]:

$$G_S = e^{g_R I_0 L} \tag{3.9}$$

where g_R is the Raman gain coefficient and L the length of the cavity. Under great pump intensity, the gain is large enough to lead to pump depletion. As a consequence, any changes in pump intensity can no longer keep the exponential behaviour of G_S and instead result in a linear response. Effectively we observe that under great intensity pump fields, the Stokes laser follows linearly the temporal changes of the pump and therefore the temporal envelope of the Stokes field becomes an almost exact copy of the pump temporal envelope. As a result, eq. 3.8 no longer stands true but $\Delta\omega_g$ is rather only determined by the pump linewidth as $\Delta\omega_g \approx \Delta\omega_p$.

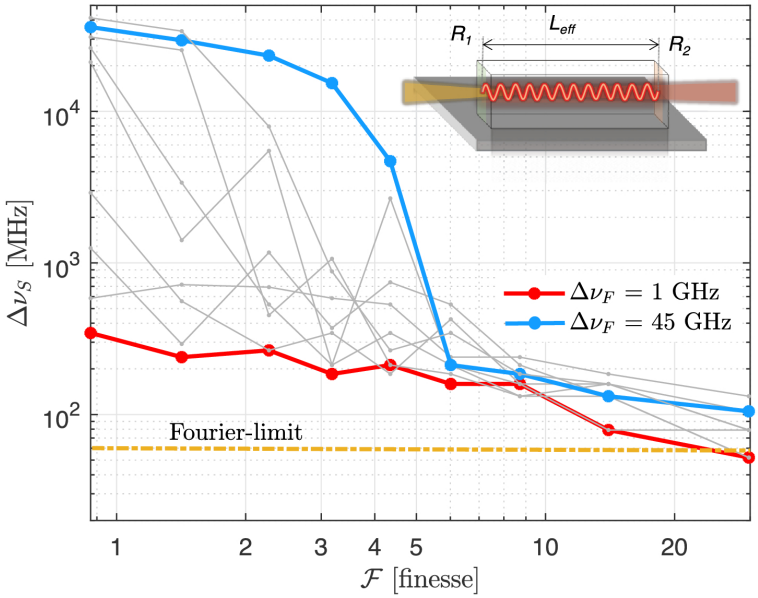

FIGURE 3.4: Simulations of Stokes laser linewidth from a monolithic diamond resonator with variable finesse for different pump linewidths [2].

In order to achieve this, a high gain, single-pass resonator is required, which is also characterised by a low Q number. When these conditions are applied, eq. 3.9 changes to:

$$FSR > \Delta\omega_p \tag{3.10}$$

This condition makes the situation much more favorable, because a GHz broad $\Delta\omega_p$ requires milimeter long resonators, that are much easier to handle with bare hands and non-specialised equipment.

To confirm the theoretical background, Granados et al. [2] simulated the behaviour of a 5 mm long monolithic diamond resoantor with variable finesse, under

various pump linewidths from 1 to 45 GHz . This resulted in Stokes linewidths down to the Fourier limit. The results of these simulations can be seen in Fig. 3.4.

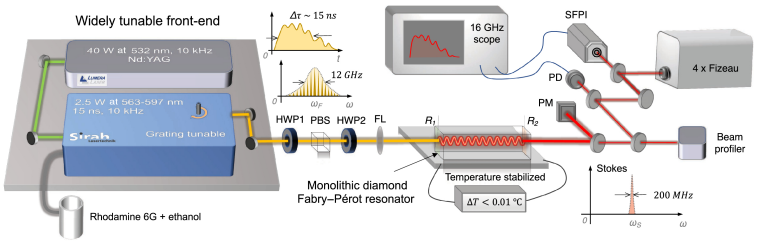

FIGURE 3.5: Experiment for the characterisation of the single-frequency Stokes field [2].

After the successful simulations, the next step was to devise an experiment and measure the resulting linewidth. A tunable dye laser was used with a wavelength between 563 and 597 nm and linewidth of $\Delta\nu_p = 11.9$ GHz at 570 nm. The output power was 2.5 W. The FSR of the 5 mm resonator was $FSR = 12$ GHz which is almost equal to $\Delta\nu_p$. The diamond resonator was placed inside a temperature stabilised oven and was pumped at 568 nm and with a Stokes field output at 614 nm. The Stokes laser was guide to diagnostic equipment for characterisation. The experimental setup can be seen in Fig. 3.5

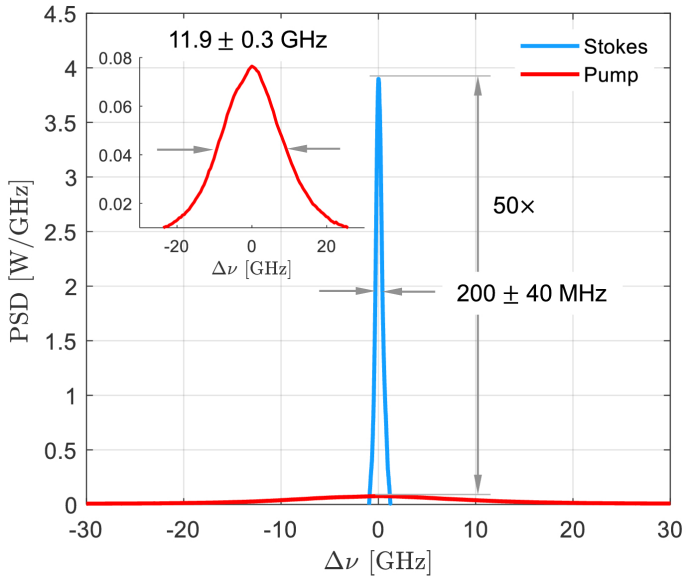

FIGURE 3.6: Comparison between the Stokes field and the pump linewidth. Inset: pump linewidth [2].

The results obtained from this experiment, can be seen in Fig. 3.6. The Stokes field had a measured linewidth of 200 MHz, increasing the power spectral density (PSD) by 50 times.

Finally, these results demonstrated that using a mm long monolithic diamond resonator which is operating in the high-gain regime and follows the condition described in eq. 3.10, we can obtain narrow-linewidth nanosecond laser fields, down to the Fourier limit.

3.4 Tuning methods

In general it is imperative that a SLM laser comes with adjustable output. Typically tuning of a conventional narrow-linewidth laser involves either tuning the pump laser or requires complex systems with a plethora of components that is usually time and money costly. As an advantage, due to its monolithic nature, the Raman converter allows much easier tuning methods for the Stokes output. As a rule of thumb, changing any of the parameters of the Raman medium which is the resonator itself, will result in adjustment of the single-frequency output.

An effective method of controlling the Stokes frequency is by adjusting the resonator's temperature as was done in the experiment presented in sec. 3.3. This can be implemented by placing the monolithic diamond inside a temperature stabilised oven that offers precise thermal control. The immediate result of this, is a combination of changes in the resonator physical length due to thermal expansion, in the group index of the material and in the refractive index for a single wavelength. Additionally the Raman shift of the medium will be changed as well, which in total results in adjustment of the Stokes center frequency.

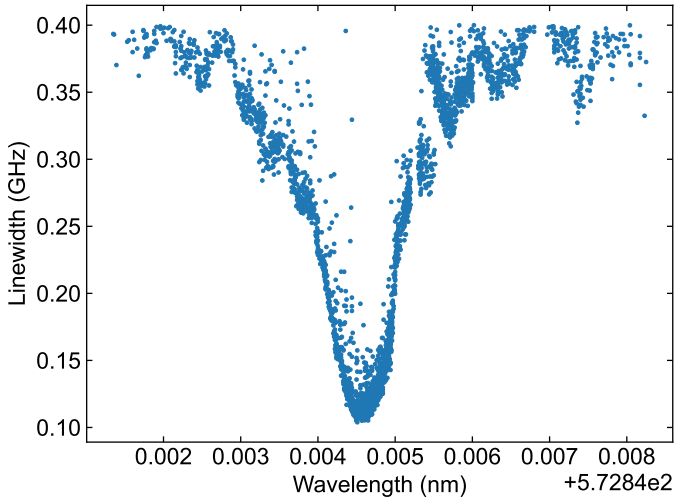

FIGURE 3.7: Scanning pump injection angle with 30 nm resolution motors, results in modulation of wavelength and linewidth.

Alternative Stokes wavelength control methods can be induced by varying other external factors, like pressure, electric and magnetic fields and pump injection parameters (position and angle). Stating with the pump injection parameters, and more specifically changes in the angle of pump injection, they will, for starters, lead to changes in the axis of pump laser propagation, switching for example the configuration from a linear resonator, to a ring resonator. Through this we can change the narrow-linewidth output, while we can also benefit from the polarization and gain adjustments. Indeed by scanning the injection angle we observed both wavelength and linewidth tuning. For the demonstration we used motor-mounted mirrors with a 30 nm resolution. The experimental results can be seen in Fig. 3.7.

Pressure variations, as mentioned above, can also adjust the single-frequency output. The principle of operation lies in the minimal birefringence and piezoelectric effect found in diamond. By affecting these properties, we change the refractive index and as a consequence the optical path of the resonator, which determines the

output Stokes field. Typically we need pressure changes in the order of GPa, although smaller variations can also work. Similar effects are induced by applying electric or magnetic fields on the diamond resonator. They take advantage of the electro-optic and the magneto-optic effect respectively and they require typical values of up to 10^6 V/cm and between 0.5 to 1.5 T. Lastly, acoustic waves can be used as well for analogous effects.

Chapter 4

Influence of non-linear thermal effects on diamond resonators

Continuing from the previous chapter, we elaborate on the tuning method we implemented, which is through temperature adjustments. We start by presenting in detail the working principle of temperature tuning which results in a theoretical and numerical model while we also present the experimental approach to demonstrate it's capabilities. We proceed by recognising the shortcomings of the current numerical approaches to model the resonator's behaviour and we create a new one focusing on precise measurements of the thermo-optic coefficient of diamond.

4.1 Tuning with temperature

In sec. 3.4, we saw several tuning methods for the Stokes output of the diamond resonator. In our approach we used temperature as the main tuning method. The driving cause of this choice was the low-value coefficients that dictate diamond's opto-mechanical changes with temperature. The coefficients we refer to, are the thermal expansion and thermo-optic coefficient, which determine the change of physical length and refractive index with temperature. Out of all crystaline materials appropriate for SRS, diamond has the lowest combinations of these with a thermal expansion coefficient $\alpha \approx 10^{-6}$ K^{-1} and a thermo-optic coefficient $1/n \cdot \partial n/\partial T \approx 10^{-6}$. It becomes clear then, that the availability of temperature control, along with the aforementioned coefficients, render it an ideal method for the tuning of the output laser field.

Before we start the implementation of temperature tuning we need to analyse the physics behind it. The key concept lies in the fact light sees a length different than the physical length. The effective length L_{eff} is given as a product between the physical length L and the refractive index n ($L_{eff} = L \cdot n$). Combining these premises with eq. 3.1 we get a system of equations.

$$\begin{cases} \nu_S = \frac{c}{\lambda_S} \\ L_{eff} = n \cdot L \\ q \cdot \frac{\lambda_S}{2} = L_e ff \end{cases} \tag{4.1}$$

where c is the speed of light, ν_S the Stokes frequency and λ_S the Stokes wavelength. By following perturbation theory and ignoring second order terms, we can find the rate of spectral change with temperature $\frac{\partial \nu_S}{\partial T}$ as:

$$\frac{\partial \nu_S}{\partial T} = -c \frac{\frac{1}{n}\frac{\partial n}{\partial T} + \alpha}{\lambda_S \left(1 - \frac{\lambda_S}{n}\frac{\partial n}{\partial \lambda}\right)} \tag{4.2}$$

where n is the refractive index of diamond. As it has been mentioned before, the exact value of the resonant Stokes frequency is determined by the opto-mechanical properties of the resonator. However, the range of the candidate frequencies is determined by the Raman phonons of diamond. The frequency of these phonons is temperature dependent and therefore the range of lasing frequencies is also changing with temperature. From literature [37], we find that the Raman phonon frequency with temperature is given as:

$$\omega_R(T) = 1332.7 - A_R \left(\frac{2}{e^{\frac{\hbar\omega_R}{2k_B T}} - 1} \right) \frac{10^7}{c} \, [\mathrm{cm}^{-1}] \tag{4.3}$$

where 1332.7 cm^{-1} is the value of the Raman phonons at 0 K, A_R is a constant related to the dispersion lines of diamond and be found fitting to the experimental data shown in [3] with a value of $A_R = 2.6 \times 10^3$ GHz, k_B is Boltzmann's constant and c is the speed of light in vacuum. As a result we get a temperature tuning of the resonant Stokes wavelength and at the same time we have a temperature dependence of the lasing range as seen in Fig. 4.1.

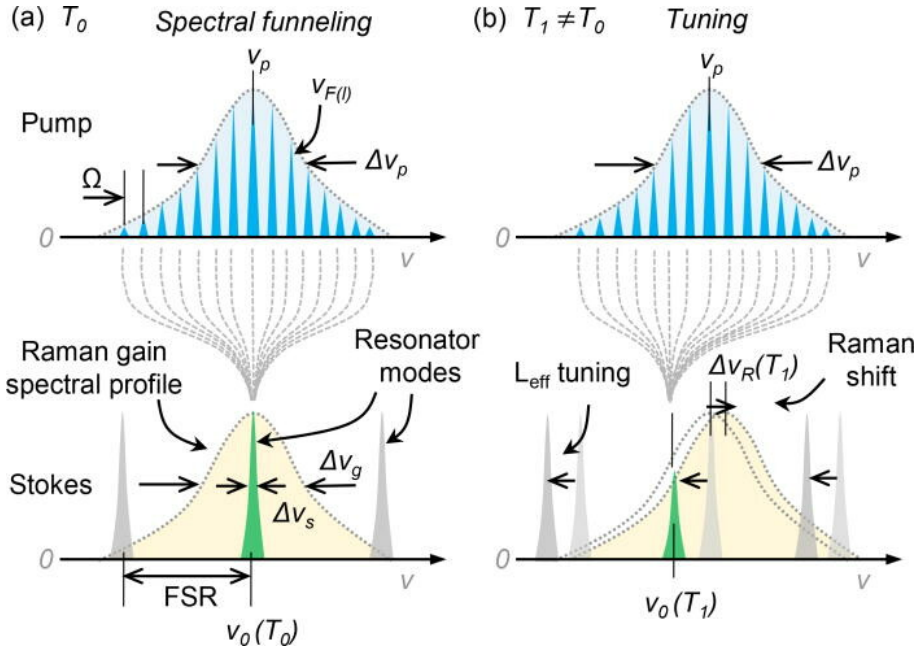

FIGURE 4.1: (a)Multi-mode pump creates a single-mode Stokes field. (b)Temperature changes shift both the Stokes field and the Raman gain [3].

To implement temperature tuning we put a 6 mm-long monolithic diamond resonator on top of a copper substrate inside a high precision oven ($\Delta T \approx 10$ mK). We pumped the diamond using a tunable, intracavity frequency-doubled, gain switched Ti:Sapphire laser with an output wavelength of 450 nm, similar to the one described in [38]. The Ti:Sapphire laser was pumped by a Q-switched Nd:YAG laser operating at its second harmonic (532 nm) with power of 18 W in pulsed configuration with a frequency of 10 kHz. The pump had a lineiwdth of 10 GHz and a 10 kHz repetition rate. The experimental setup can be seen in Fig. 4.2. After scanning the temperature of the resonator we obtained the results seen in Fig. 4.3.

The individual lines in Fig. 4.3 (a) are due to the the precise change of effective optical length with temperature determined by eq. 4.2. They showed an average

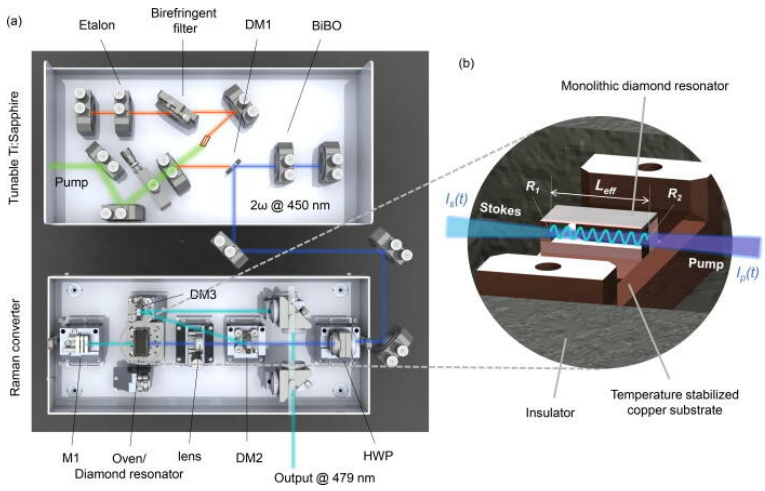

FIGURE 4.2: Ti:Sa laser pumps a temperature controlled monolithic diamond resonator [3].

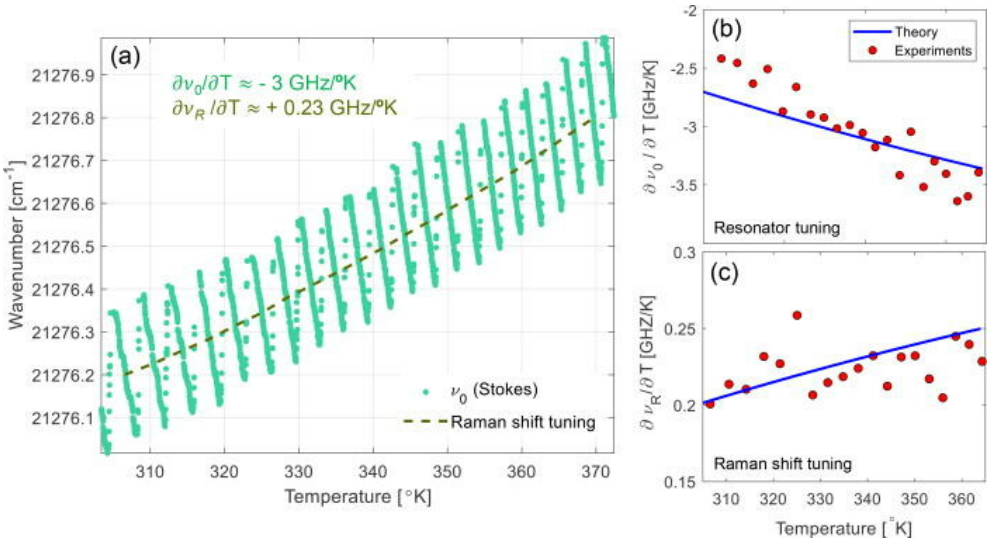

FIGURE 4.3: (a) Stokes wavelength as a function of temperature. (b) Comparison between measured $\frac{\partial\nu_S}{\partial T}$ and theoretically calculated from eq. 4.2. (c) Raman shift $\frac{\partial\nu_R}{\partial T}$ change with temperature [3].

slope of 3 GHz/K which is slightly different than the value predicted by eq. 4.2 as can be seen in Fig. 4.3 (b). The mode hops are determined by the lasing range and the overall upward trend is due to eq. 4.3 with an average slope of 0.23 GHz/K which agrees with the respective theory.

The obtained results can show us the resolution of our system. With a rate of change $\frac{\partial\nu_S}{\partial T} \approx 3$ GHz/K and a precision oven with an accuracy $\Delta T \approx$10 mK we can obtain a spectral accuracy of 30 MHz or 33 fm. These results show a great tuning capabilities and render temperature tuning the main method for monolithic diamond resonators.

4.2 Phonon harmonicity

The use of monolithic diamond resonators in demanding applications requires very precise knowledge of the resonant Stokes frequency and its response with temperature changes. We can see however that in Fig. 4.3 (b) the theoretical prediction of $\partial\nu_S/\partial T$ is diverging from the experimental findings. The deviation can only be attributed to the thermal response of either the resonator's length (thermal expansion coefficient α) or the resonator's refractive index (thermo-optic coefficient $1/n \cdot \partial n/\partial T$). A research through the available literature however, can show that the thermal expansion coefficient is well-documented while the same can not be said for the thermo-optic coefficient, with only a value of $1/n \cdot \partial n/\partial T = 5 \cdot 10^{-6}\ K^{-1}$ at 300 K for the low-frequency limit [39] and measurements up to 925 K in the far-infrared region [40]. However there is no information on the thermo-optic coefficient of diamond at visible wavelengths for a large temperature range. It is deemed necessary then, that in order to predict the spectral behaviour of a monolithic diamond resonator with temperature, a precise model for the thermo-opitc coefficient is required.

An analytical description of the thermo-opitc coefficient of diamond is hard to derive since it requires a model for the dielectric function which needs to be renormalized by the electron-phonon interaction and the thermal expansion of the lattice [40]. Another approach includes using empirical pseudo-potentials but due to carbon's (C) large Debye temperature $\Theta_D = 1880$ K, the thermo-optic coefficient varies significantly with temperature. This is attributed to the fact that a linear approximation of the temperature-dependent part of the refractive index $n(T)$ is true only for temperatures much larger than Θ_D, where the material can be described by a single oscillator frequency.

In our approach we study the thermo-optic coefficient, by separating the refractive index into two additive terms, one wavelength $n_\lambda(\lambda)$ and one temperature $n_T(T)$ dependent, following the steps of Ruf et al. [40]. We write the wavelength and temperature dependent index of refraction $n(\lambda, T)$ as:

$$n(\lambda, T) = n^0_\lambda(\lambda) + n_T(T) \tag{4.4}$$

In eq. 4.4, the term $n^0_\lambda(\lambda)$ refers to the Sellmeier equation at 0 K. Since the Sellneier equation is widely studied at room temperature (300 K), we need to apply a constraint in order to ensure that the refractive index is the one commonly known at 300 K. The constraint is formulated as:

$$n^0_\lambda(\lambda) = n_\lambda(\lambda) - n_T(300) \tag{4.5}$$

where $n_\lambda(\lambda)$ refers to the well-known Sellmeier equation at 300 K. For CVD diamond we followed the most recent study which used a single-term Sellmeier equation described in [41] as:

$$n_\lambda(\lambda) = \sqrt{1 + \frac{4.658 \cdot \lambda^2}{\lambda^2 - 112.5^2}} \tag{4.6}$$

For the temperature-dependent part $n_T(T)$, we begin by observing that it's value depends on the lattice energy which is proportional to the internal energy U of the system [40]. For a system of N oscillators with average frequency of ω_{avg}, U is given by:

$$U = N\left(\frac{1}{e^{\frac{\hbar\omega_{avg}}{k_B T}} - 1} + \frac{1}{2}\right) \tag{4.7}$$

where $\hbar$ is Plank's constant divided by π, and k_B is Boltzman's constant. Since diamond follows the Bose-Einstein distribution to describe the unit cell infrared active vibration [42], we can approximate $n_T(T)$ as:

$$n_T(T) = n_0 + A\left(\frac{1}{e^{\frac{\hbar\omega_0}{k_B T}} - 1} + \frac{1}{2}\right) \tag{4.8}$$

where n_0 and A are fitting constants related to the refractive index at 0 K and the dispersion lines of diamond respectively, and $\hbar\omega_0$ represents the average phonon frequency. These factors were estimated by Ruf et al [40] by fitting to their experimental data. This resulted in a numerical value of $A = 0.01902$ and an average phonon frequency of $\hbar\omega = 711\ cm^{-1}$, with no temperature dependence. However, the thermal expansion of the lattice and multiphonon coupling effects [43] change the phonon frequencies of the lattice and therefore induce a temperature dependence of the average phonon frequency which needs to be addressed.

Continuing with the thermal expansion coefficient $\alpha(T)$ of CVD diamond, we follow the approach presented in the work of Jacobson et. al [44], where it's modeled as:

$$\alpha(T) = \sum_{i=1}^{n} X_i\, E\left(\frac{\Theta_i}{T}\right) \tag{4.9}$$

where $E(x)$ is:

$$E(x) = \frac{x^2 e^x}{(e^x - 1)^2} \tag{4.10}$$

The values used for X_i and Θ_i are the experimental ones that can be found in reference [44].

Even though Raman phonons don't determine the exact Stokes frequency but rather determine the range of the potential lasing frequencies, it is important for completeness to analyse the effect. The model describing it, is based on the Klemens approximation [45] which assumes that the zone-center phonons decay into two acoustical phonons of opposite momentum. This has been shown by Debernardi et al. [46] to accurately describe the diamond lattice. Starting by the relaxation time τ of the Raman phonons we have that:

$$\tau \simeq 1 + \frac{2}{e^{\frac{\hbar}{k_B T}\frac{\omega_R}{2}} - 1} \tag{4.11}$$

where ω_R is the Raman shift. The relaxation time τ is proportional to the Raman linewidth $\Delta\omega_R$ and that later is linearly connected to the Raman shift [37]. The temperature-dependent Raman shift is then given by eq. 4.3 as has been mentioned previously.

After establishing all the terms of eq. 4.2 we can continue with the experiment that will measure $\partial\nu_S/\partial T$, allowing us to calculate the thermo-optic coefficient $\frac{1}{n}\frac{\partial n}{\partial T}$. During the experiment we used an array very similar to the one used in section 4.1 with the only difference in the pump laser as can be seen in Fig. 4.4. It was a

frequency-doubled Nd:YAG laser on single-frequency operation at 532 nm generating 10 ns pulses with a repetition rate of 100 Hz and energy of 50 μJ.

A single-frequency pump has the same effects as a multi-mode pump, with the only difference lying in a modification in the equations that describe the laser fields. SRS with a multi-mode pump is described by [2] as:

$$\frac{1}{u_S}\frac{\partial S_l}{\partial t} + \frac{\partial S_l}{\partial z} = 2cn_F\epsilon_0\frac{g_0}{2}\sum_r\sum_j F_{l-r}(S_j F^*_{j-r})\frac{\Delta\omega_R}{\Delta\omega_R - ir\Omega_F}e^{i[(l-j)\mu_\pm\Omega_F]z} \tag{4.12}$$

$$\frac{1}{u_F}\frac{\partial F_l}{\partial t} + \frac{\partial F_l}{\partial z} = -2cn_S\epsilon_0\frac{g_0}{2\eta}\sum_r\sum_j S_{l-r}(F_j S^*_{j-r})\frac{\Delta\omega_R}{\Delta\omega_R + ir\Omega_F}e^{i[(j-l)\mu_\pm\Omega_F]z} \tag{4.13}$$

Concidering a a single-mode pump and output laser would mean that $\{F_l, \quad S_l = 0\ \forall\ l \neq 0\}$ which would simplify eq. 4.12, 4.13 to:

$$\frac{1}{u_S}\frac{\partial S_0}{\partial t} + \frac{\partial S_0}{\partial z} = 2cn_F\epsilon_0\frac{g_0}{2}|F_0|^2 S_0 \tag{4.14}$$

$$\frac{1}{u_F}\frac{\partial F_0}{\partial t} + \frac{\partial F_0}{\partial z} = -2cn_S\epsilon_0\frac{g_0}{2\eta}|S_0|^2 F_0 \tag{4.15}$$

These equations effectively describe the dynamics of single-frequency pump and Stokes lasers, allowing us to continue with our experiment.

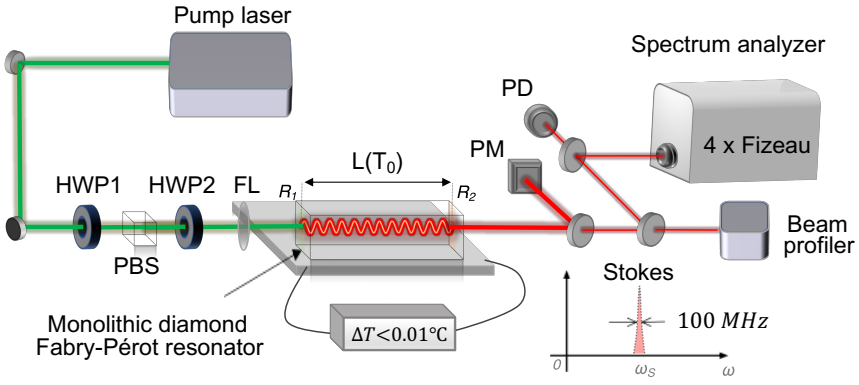

FIGURE 4.4: Experimental setup used of the measurement of the thermo-optic coefficient $\frac{1}{n}\frac{\partial n}{\partial T}$. HWP1, HWP2: half-wave-plates; PBS: polarizing beam splitter; FL: focusing lens, PM; power meter. [6]

The pump field, was guided through a power control system which was composed of a half-waveplate (HWP1) and a polarizing beam splitter (PBS) while the polarization of the pump was controlled using another half-wave plate (HWP2). This was important since Raman conversion efficiency is heavily dependent on polarisation and it maximises when the pump is parallel to the $\langle 111 \rangle$ axis. The pump light was then focused into the monolithic diamond resonator through a 150 mm focal length lens (FL) with a resulting waist of 50 ± 5 μm. After the Raman conversion took place, we generated both first and second Stokes field. We filtered out the second Stokes which resulted in a single-mode Stokes field at 573 nm.

The beam was then guided to a spectrum analyzer, a power meter (PM), a photodiode (PD) and a beam profiler (BP). The linewidth (FWHM) of the Stokes laser

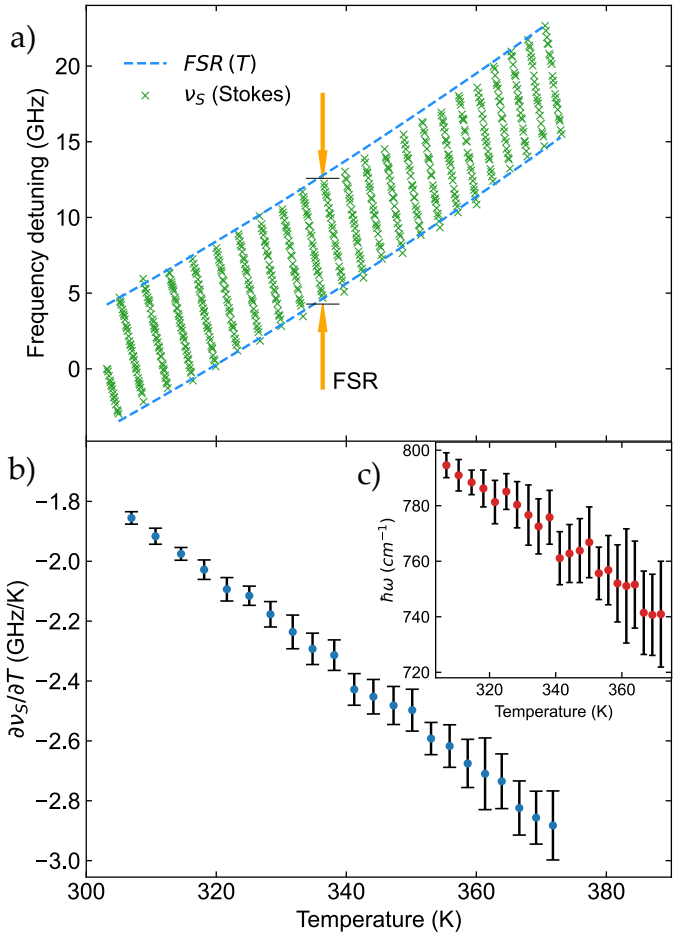

FIGURE 4.5: (a) Stokes center frequency (ν_S) detuning with temperature. Dashed blue line shows the change of lasing range with temperature. (b) Measured tuning slope for each FSP with temperature. (c) Calculated average phonon frequency by solving eq. 4.2. [6]

$\Delta\nu_S$ was measured by a wavelength meter, Atos LM-007 wavemeter, which uses four sensitive Fizeau interferometers for accurate measurements down to 50 MHz. Stokes lineiwdth was found to be $\Delta\nu_S = 100 \pm 20$ MHz averaged over ~ 1000 shots. The stability of the system was measured over 16 h and had a root-mean-square < 4 MHz as can be seen in Fig. 4.6

Using this setup a temperature scan from 300 K to 373 K was performed, using a high precision temperature controller with a resolution < 10 mK. The measurements can be seen in Fig. 4.5. It can be observed that the tuning slope increases in absolute value with temperature due to the thermal expansion and thermo-optic coefficient. It shows a significant change from -1.8 GHz/K to -2.8 GHz/K over a range of 70 K. The error bars in Fig. 4.5 (b) represent the 99% confidence interval. A noticeable correlation between temperature and error can be observed which can mislead us into thinking that the error is systematic. This is not the case but it is rather due to the fact that fewer measurements were taken because of the nonlinear speed of the temperature scan. The tuning range changes with temperature as $\partial\Delta\nu_R = 0.23$ GHz/K which is confirmed by the Klemens approximation that predicts a rate of change between 0.2 and 0.25 GHz/K.

Using the values of the average slope of each FSR (Fig. 4.5 (b)) we can solve eq. 4.2 in order to find the average phonon frequency $\hbar\omega$ of each FSR. This is shown in

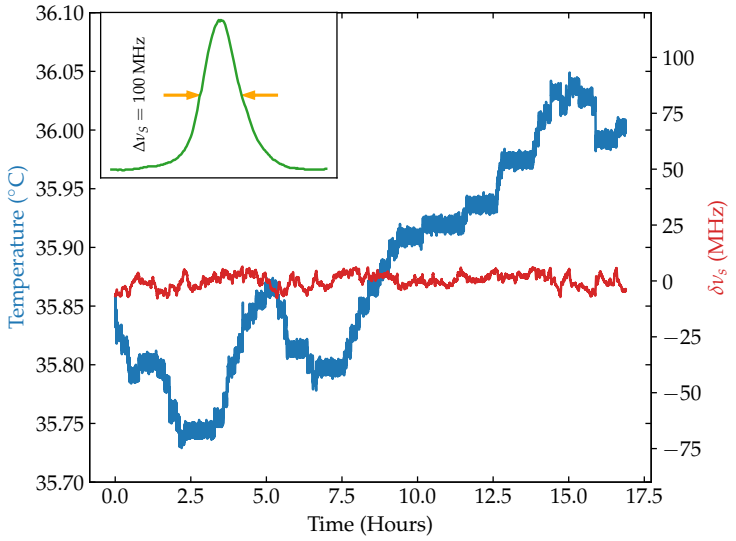

FIGURE 4.6: Temperature stabilized Stokes field over 16 h with $RMS < 4$ MHz. Inset shows Stokes linewidth. [6]

Fig. 4.5 (c). The calculated $\hbar\omega$ are then used in eq. 4.8 which results in the thermo-optic coefficient. The estimated values can be seen in Fig. 4.7.

In general the thermo-optic coefficient as a function of temperature is most non-linear between 300 and 400 K. Below 200 K, $\frac{1}{n}\frac{\partial n}{\partial T}$ tends to 0 while above 500 K it asymptomatically tends to constant value that we extrapolated to be $\sim 8 \times 10^{-6}\ K^{-1}$.

In conclusion, it has been shown that existing models can not accurately describe the temperature dependence of diamond's refractive index but they only approximate it to experimental data using a fixed average phonon frequency $\hbar\omega_0$. However this is an inaccurate approximation and therefore previous results deviate at this range. In this study however, we have experimentally measured the thermo-optic coefficient $(1/n)\partial n/\partial T$ since the Stokes detuning slope $\partial\nu_S/\partial T$ directly depends on it.

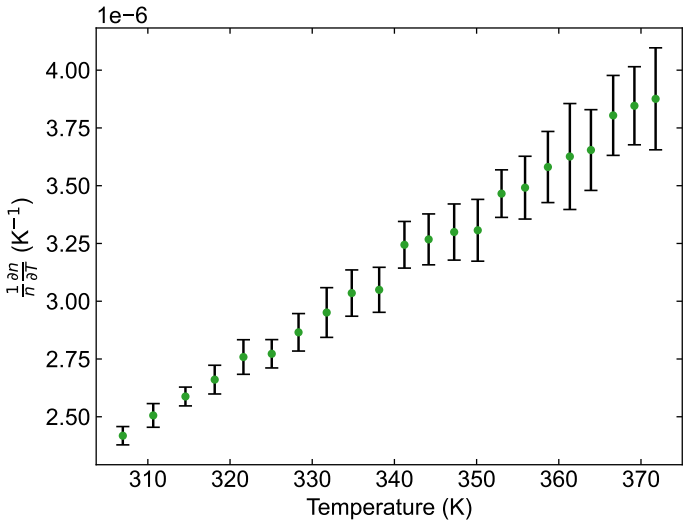

FIGURE 4.7: Thermo-optic coefficient with temperature in range between 300 and 370 K. [6]

As a result, we propose a method to calculate the thermo-optic coefficient of a material, where the temperature is scanned while at the same time the resonant Stokes wavelength is measured, in order to get accurate measurements of the coefficient. This is a very flexible method as it combines very narrow spectral bandwidth and resulting high spectral density from the resonator with the large transparency range of diamond. This renders our method very versatile, being usefull for a large range of wavelengths and temperatures.

Finally, we propose a model that can estimate the average phonon frequency of the diamond lattice under strong SRS. It is a promising model approximating parameters like the thermo-optic coefficient that can offer key information regarding research related to temperature sensitive integrated photonic devices in diamond or other similar materials.

Chapter 5

Further spectral purification

Tuning of the resonator can occasionally amplify it's spectral squeezing capabilities. In this chapter we delve into the physics governing this effect and we explain its appearance. After this, our next step is to model this effect and we attempt to observe it during the tuning of the monolithic diamond resonator. The experimental results show significant agreement with our prediction allowing for further linewidth-narrowing.

5.1 Double resonance effects

The tuning methods we talked about, operate by effectively changing the resonator's optical path either by changing the length, the refractive index or both. As a result the SLM output must follow the spectral behaviour of the resonator and of course it changes its value. As the monolithic diamond resonator is used in a Fabry-Pérot configuration, it's optical path is continuously changedand it's spectral behaviour is similar to a scanning Fabry-Pérot interferometer (FPI). The dominant effect observed in a FPI is that an external laser field will periodically resonate and it's intracavity intensity will periodically maximise. This is due to intracavity resonance of the laser field whenever it fulfills the resonant condition described in eq. 3.1. The periodic resonance effect in a scanning FPI can be seen in Fig. 5.1.

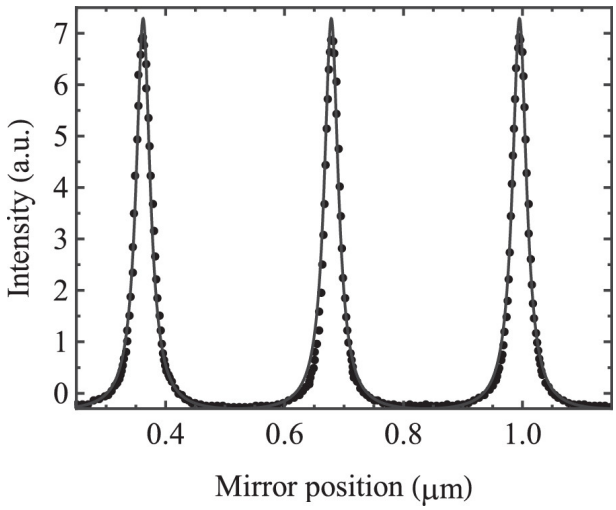

FIGURE 5.1: Periodic resonances as optical path changes [4].

In an similar manner, this phenomenon can appear in the monolithic diamond resonator when the pumping laser is single-mode (a single-mode pump laser doesn't change anything in the governing physics but it only changes m to 0 in eq. 3.4). From

the perspective of the single-frequency pump field that is characterised by a fixed wavelength, the resonator's optical path periodically matches its own wavelength. Pump resonance leads to constructive intracavity interference which effectively increases the pump power inside the Raman medium. This increase has a result of further narrowing the linewidth [2]. It is a valid hypothesis then, that under continuous tuning we will observe periodic linewidth-narrowing when both the Stokes and pump resonate meaning when there is the doubly resonant regime.

5.2 Double resonance

In section 5.1 it has been mentioned that under continuous tuning of the monolithic diamond resonator, periodic pump resonances will appear due to the continuous change of the optical path, transitioning to the doubly resonant regime. In the experiment described above, tuning is implemented through precise control of the resonator's temperature and therefore pump resonance should be observed with a periodic temperature change, i.e. it will happen every ΔT. The dominant hypothesis is that at the temperature points of double resonance T_i we will observe additional linewidth squeezing and at the same time increased power spectral density (PSD) [kW/GHz]. These dynamics can be seen in Fig. 5.2.

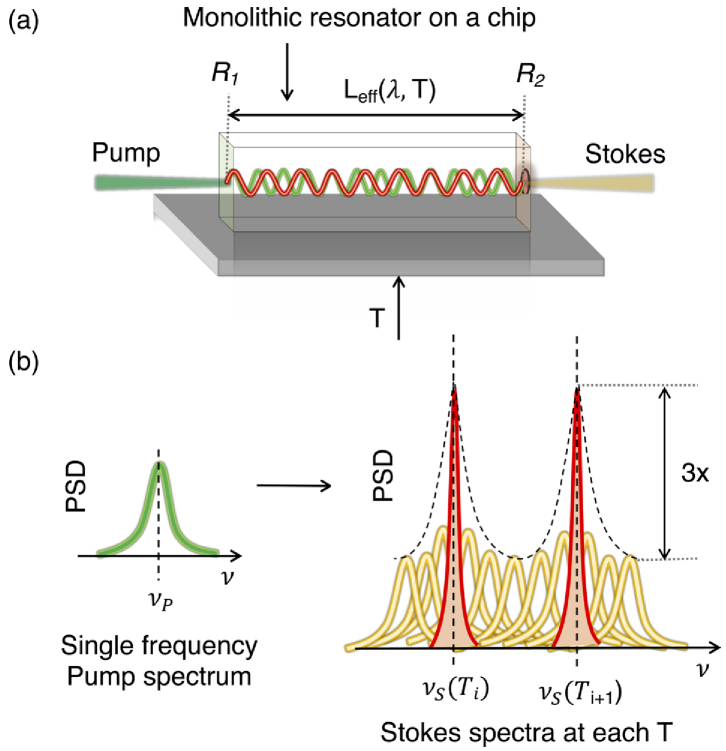

FIGURE 5.2: As the monolithic diamond resonator (a) is tuned, it periodically enters the doubly-resonant regime at certain temperatures T_i where the linewidth of the Stokes decreases and the PSD increases. [5]

To understand this effect it is necessary to model it. Starting by the Stokes field, it continuously follows the resonant condition as it changes following the change of optical path of the resonator, always remaining resonant while the single-frequency

pump periodically resonates when the optical path of the integrated resonator allows it, at certain temperatures T_i. These two conditions can be written as:

$$\begin{cases} \nu_S(T) = q_S \frac{c}{2L_{eff}(T,\nu_S)} \\ \nu_F = q_{Fi} \frac{c}{2L_{eff}(T_i,\nu_F)} \end{cases} \tag{5.1}$$

were q_S is the mode number of the Stokes and q_{Fi} the mode number of the pump. The effective length is $L_{eff} = n(T,\lambda)$ and can be calculated by the model presented in section 4.2. The first part of the model which requires knowledge of the resonant Stokes field with temperature, is already well-known from section 4.2. The second part demands numerical calculation of the pump resonant temperatures T_i. Combining these two, modeling the process is possible, were the crossings of the resonant Stokes frequency with the lines $x = T_i$ indicate the areas of double resonance. The model can be seen in Fig. 5.3.

To confirm the theoretical analysis we devised an experiment using the same setup as the one used in section 4.2. It is important to note that the pump laser used both in section 4.2 and here, was single-mode. The difference in this experiment compared to the one presented in section 4.2 is that the linewidth of the output Stokes field was continuously measured. The experimental data of the temperature scan can be seen in Fig. 5.4. The graph depicts similar data to Fig. 4.5 (a) with the addition of a colormap based on the linewidth of each point. The minimum Stokes spectral width was measured to be 130 MHz in the doubly resonant regime, while for the other cases it was found to be > 500 MHz.

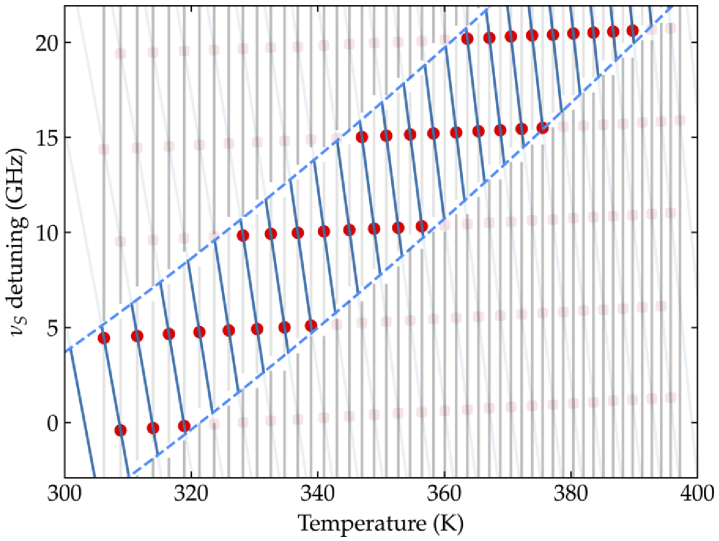

FIGURE 5.3: Predicted areas of double resonance. Blue lines show the center Stokes frequency while the grey lines show the temperatures T_i where the pump resonates. The red dots are the crossings of the blue and grey lines where double resonance happens. [5]

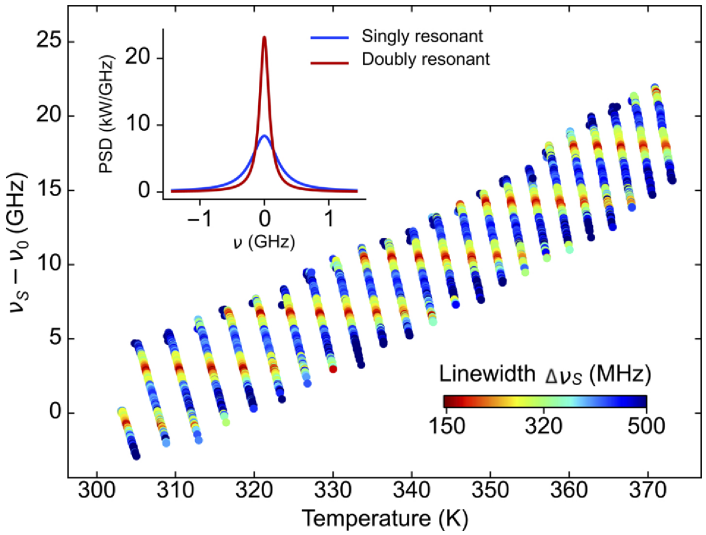

FIGURE 5.4: Measured Stokes frequency with linewidth-based colormap. Inset compares the PSD between single and double resonance. [5]

Using a different point view, Fig. 5.5 was plotted, showing the Stokes linewidth $\Delta\nu_S$ in respect to Stokes detuning $\nu_S - \nu 0$. The relationship between two quantities is quasi-linear for small temperature changes. An interesting feature of this plot is the second-order resonances that are attributed to higher resonator modes and are present in all doubly resonant ranges with a linewidth $\Delta\nu_S \approx 250$ MHz.

The periodicity observed in Fig. 5.5 (a) agrees with the one predicted in the theoretical model and even though it is variable with temperature, for the ranges studied here it is $\approx 3.7 \pm 0.1$ GHz. Lastly, we can observe that the minimum linewidth has a weak linear dependence on temperature as can be seen in Fig. 5.5 (c). This can be attributed to the Raman gain which linearly decreases with temperature at this temperature range.

Finally in Fig. 5.6 we can see the PSD which results from a combination of Stokes center frequency, lineiwdth and output power measurements. This graph was created assuming Lorentzian profiles for the Stokes laser as it was measured in [2]. The maximum PSD was measured to be 21.6 kW/GHz and the minimum 6.3 kW/GHz. From the inset of Fig. 5.6 we can see that to fulfill the double resonance condition we need a temperature stability < 0.07 K.

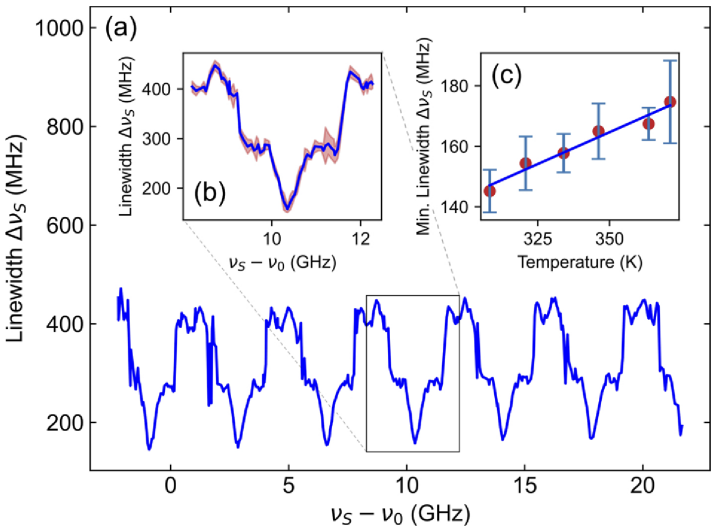

FIGURE 5.5: (a) Linewidth of Stokes field as a function of the Stokes center frequency detuning. (b) Average and deviation of the linewidth measured or a particular detuning range. (c) Average minimum linewidth and deviation as a function of temperature. [5]

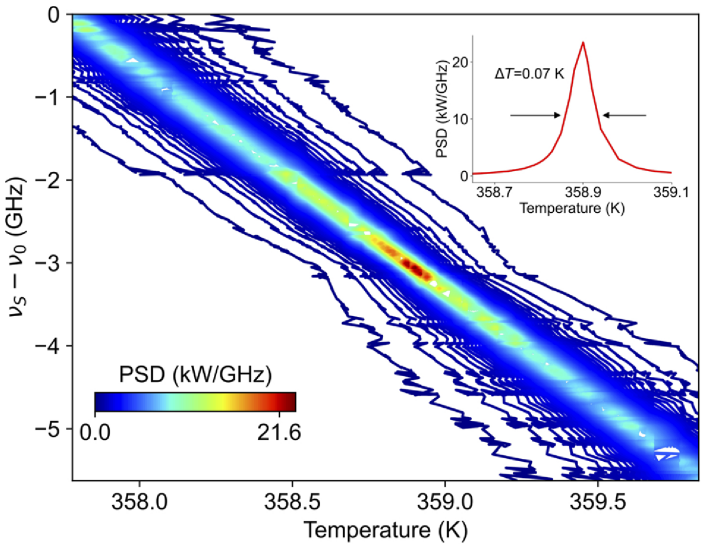

FIGURE 5.6: PSD as a function of temperature and Stokes center frequency detuning $\nu_S - \nu_0$. Inset shows the line-out of PSD as a function of temperature. [5]

In conclusion we can see that appropriate temperature tuning can significantly increase the brightness of the Stokes field. Temperature offers an easy access to the double resonance condition while the imperfect parallelism of the diamond's edges allows us to tune the doubly resonant condition over a wide range. These results combined with the low-quality characteristics of the monolithic diamond resonator, promise further improvement of the PSD when higher Q resonators are used along with suitable control systems.

Chapter 6

Demonstration of Doppler-free spectroscopy using a monolithic diamond resonator

This chapter comes at the end as the result of the previous studies and it focuses on a practical application of the monolithic diamond resonator. We use the single-frequency Stokes laser to perform high-resolution (HR) spectroscopy. We start by discussing what is HR spectroscopy and the requirements to achieve. We proceed by explaining how we fulfill them and we continue with the experimental part. After describing it, we present our results and discuss on them.

6.1 High resolution spectroscopy

In chapter 1 we have stated the importance of high resolution (HR) spectroscopy because of its applications and potential to revolutionize science. After studying in depth monolithic diamond resonators and their behaviour with temperature changes, we shall demonstrate that these laser system is suitable to be used in scalable narrow-linewidth spectroscopy experiments. In order to present the demonstration it is important to first analyse the operating principles behind it.

To start the demonstration it is necessary to talk about laser spectroscopy first. Laser spectroscopy in general is achieved through resonant ionization (RIS, resonance ionization spectroscopy). RIS takes advantage of the unique electronic structure of an element and offers the exact energies required by electrons for excitation to higher energy states, as can be seen in Fig. 6.1 (a). Step-wise excitations are induced that eventually lead to ionization similar to what is shown in Fig. 6.1 (b). Only one element species gets ionised and therefore is attracted by an applied electric field, which essentially translates to an isotope filtering method based on atomic number. When this process is combined with a mass separator, an additional mass-filtering of isotopes takes place, allowing us to obtain a pure isotope beam (Fig. 6.1 (c)). Lastly the beam of ionized isotopes goes on a Faraday cup that gives a current reading, based on the amount of ions.

HR laser spectroscopy is based on the same principles of selecting atomic species through their characteristic energy gaps. The difference in this technique though lies in the fact that the HR setup is sensitive to much smaller energy gaps, being able to differentiate energy levels that are very close to each other.

Achieving this, requires three major features. Initially, a laser with linewidth much smaller than the transition we want to measure. Secondly it is necessary that this laser is tunable in order to scan it along the transition and get measurements of the full spectral profile. The last demand we need for HR spectroscopy is to limit

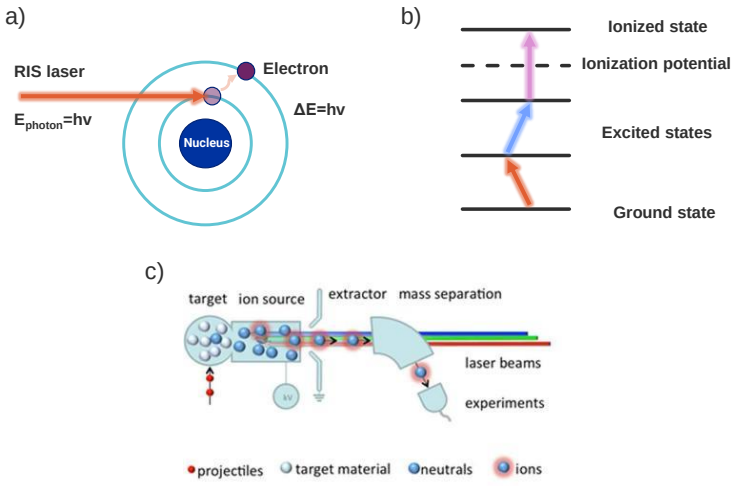

FIGURE 6.1: (a) RIS laser provides photons of the exact energy required for a transition. (b) Successive step-wise excitations lead to ionization. (c) Average minimum linewidth and deviation as a function of temperature.

any transition broadening effects enough so that the features of the natural transition profile are prevalent and the observed spectral profile is not dominated by the broadening. When these conditions are applied, we can measure the spectral profile of a transition as the convolution between the laser linewidth and the broadened transition.

While the necessity of the laser source requirements is obvious, it is also important to examine the broadening effects and why it is imperative to limit them. Firstly, the main reason broadening takes places is because of the Doppler effect. The roots of this lie in an important RIS requirement which demands high isotope temperatures ($T \approx 2100\ ^oC$) for maximizing isotope-laser interaction probability. This leads to high isotope velocities with the most probable one being:

$$v_{prob} = \sqrt{2k_B T/m} \tag{6.1}$$

were k_B is Boltzmann's constant and m the mass of the isotopes. This induces a great Doppler shift to the perceived photon frequencies. A random direction distribution for isotope velocities leads to a random Doppler shift distribution which adds up to effectively broaden the transition changing it from a narrow Lorentzian to a much broader Gaussian. This effect is called Doppler broadening and the resulting linewidth $\Delta\nu_{Dop}$ is usually in the order of tens of GHz for $T \approx 2100\ ^oC$. The relationship governing Doppler broadening $\Delta\nu_{Dop}$ is:

$$\Delta\nu_{Dop} = \nu_0 \sqrt{\frac{8k_B T\, ln(2)}{mc^2}} \tag{6.2}$$

were ν_0 is the center frequency of the transition. If left unchecked, this effect will engulf finer spectral characteristics rendering them indistinguishable from each other and therefore preventing us from detecting the neighboring energy states as seen in Fig 6.2 (a). It becomes imperative then to reduce Doppler broadening enough so that it no longer overshadows the distinct states and they can be observed Fig. 6.2 (b).

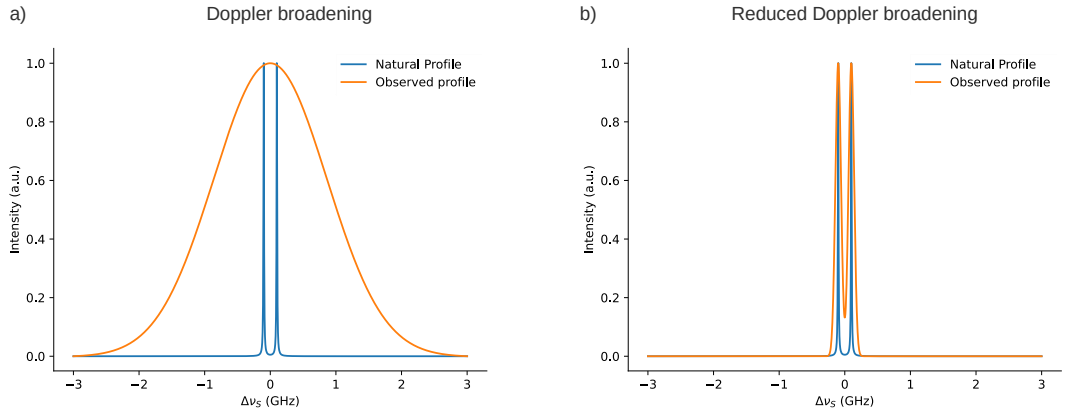

FIGURE 6.2: (a) Doppler broadening is large enough to engulf the two energy states, rendering them indistinguishable. (b) Reduced Doppler broadening renders the two energy states separable.

6.2 Reducing Doppler broadening

After understanding the requirements for HR spectroscopy, we proceed to ensure that they are fulfilled. The first two requirements, demanding a SLM and tunable laser source, are covered by the monolithic diamond resonator since it indeed provides a single frequency laser field as described in section 3.3 and is widely tunable which is analysed in section 4.1.

In order to satisfy the last requirement concerning Doppler broadening we employ the idea of crossed-beams spectroscopy. This concept takes advantage of the directional movement of isotopes along an axis e.g. z. When a laser beam is guided to the directional isotopes colinearly to axis z, the broadening effect remains unchanged. However a laser beam guided perpendicularly to axis z, will face a limited velocity spread because there is minimal isotope movement on this axis. Therefore the laser perpendicularly to axis z will face a much more limited Doppler broadening. When this laser is a tunable narrow-linewidth laser, HR spectroscopy is possible.

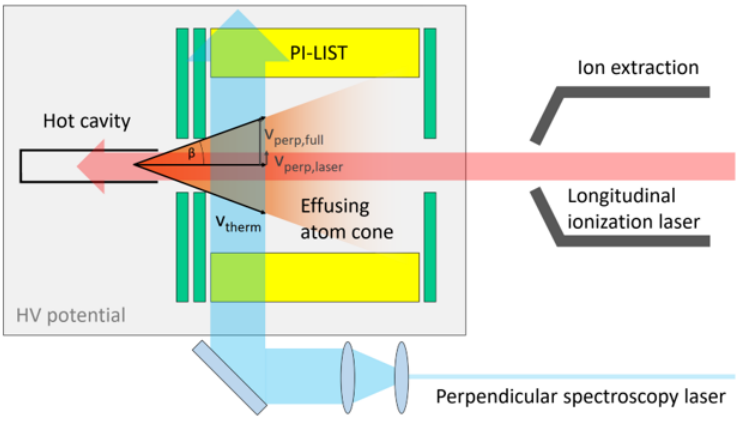

FIGURE 6.3: PI-LIST where the isotopes thermally effuse into a cone of directional movement. Two laser beams are targeted, perpendicularly to each other, allowing for HR spectroscopy. Electrodes serve to manipulate and extract isotopes [47] .

To achieve this, we used the PI-LIST (Perpendicularly Illuminated Laser Ion Source and Trap) system [47]. This system takes advantage of the high temperature of isotopes as mentioned in section 6.1 and allows them to thermally effuse out of the containment cavity through a tube. This results in an isotope cone with a highly directional movement parallel to the tube. The cone is target by two laser beams, one parallel to its movement and one perpendicularly to it. By keeping the colinear laser as is and scanning the narrow lineiwdth laser along the targeted transition, we can measure the spectral characteristics of a transition with high accuracy performing high resolution spectroscopy. A graphical representation of the PI-LIST can be seen in Fig. 6.3 where the dynamics described above are depicted.

For a simple estimation of the PI-LIST's broadening-reduction capabilities, we observe from eqs. 6.1, 6.2 that $u \propto \Delta\nu \propto \sqrt{T}$. Using the triangle equality we get:

$$u_{perp} = u_{long} \times sin(\beta) \tag{6.3}$$

with u_{long} being attributed to thermal effetcs and β the angle of the isotope cone. From eq. 6.3 we can see that with a $\beta = 20^o$, we obtain a linewidth reduction factor of 0.3. It has been demonstrated that the PI-LIST can reach much smaller cone angles, reducing Doppler-broadening from 2 GHz to 100 MHz. For this reason it is appropriate for use in high-resolution spectroscopy.

6.3 Experimental setup

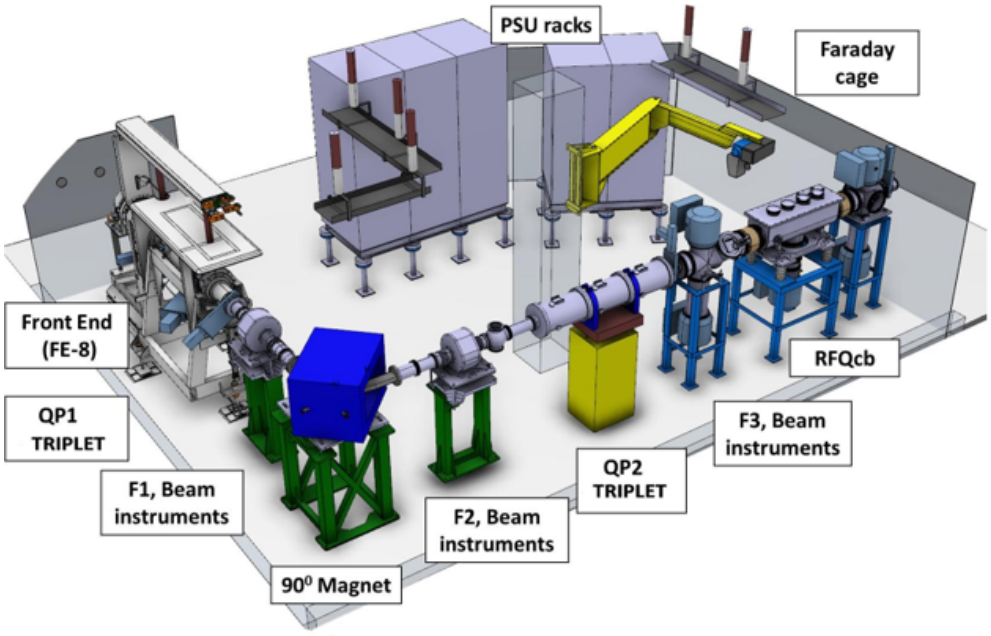

FIGURE 6.4: Shecmatic depiction of Offline-2. The PI-LIST is located on the front end. QP1, QP2: Quadrapole triplet; Beam insturments: Beam-Scanner and Faraday-Cup; RFQcb: Radio frequency cooling and bunching [48].

Having all the equipment required for HR spectroscopy, we continued by devising an experiment to demonstrate the scanning capabilities of the integrated diamond resonator. The experiment took place in the Offline-2 facility at CERN [48]. It has off-line mass separating and diagnostics equipment meant to mimic the on-line

facility of ISOLDE [49] so that it serves as testing ground for the development of new technologies. The PI-LIST is integrated in the facility and therefore it was the ideal environment for our experiment to take place. The facility offers many capabilities like isotope beam shaping and manipulation. It also allows for readout of the ionized isotopes through Faraday cups, allowing us to actually get measurements of the transition. A graphic depiction of the facility can be seen in Fig. 6.4

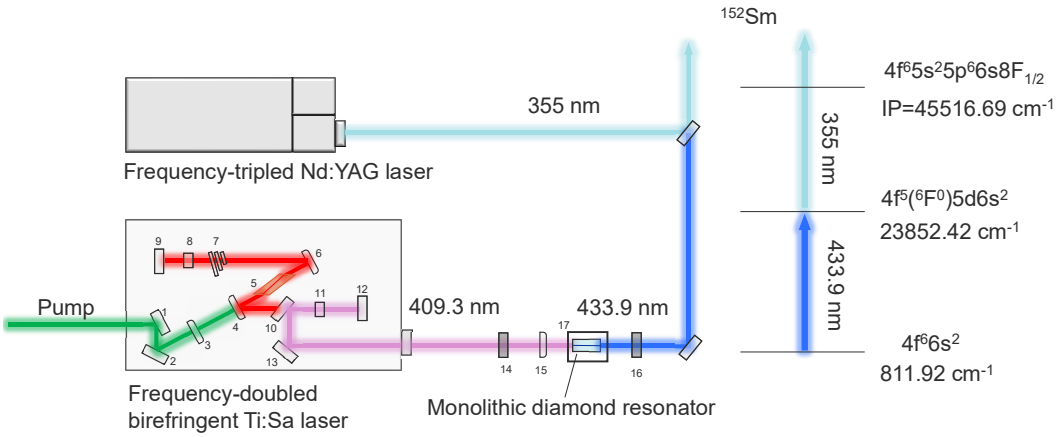

FIGURE 6.5: Optical setup for the experiment. The Stokes laser is guided in the perpendicular direction of the PI-LIST while the Nd:YAG laser in the parallel one. 1, 2, 9, 12, 13: mirrors; 3, 15: focusing lens; 4, 6: curved mirror; 5: Ti:Sa crystal; 7, 8: spectral filters; 10: dichroic mirror; 11: doubling crystal; 14, 18: HWP; 17: temperature controller.

For the HR spectroscopy demonstration we employ a two-step ionization scheme on ^{152}Sm. This isotope was chosen because it's ground state is characterised by a single peak, with no fine or hyperfine features and as a result, the natural linewidth of the transition is very narrow while the measured linewidth will give us the resolution of our setup. The Stokes laser at 433.9 nm output wavelength was used as the first ionization step, targeting the ground state of ^{152}Sm and inducing a resonant excitation. Since this was the single-frequency laser source, it was injected in the perpendicular axis of the PI-LIST. The monolithic diamond resonator, generating the Stokes field, was pumped by a pulsed, tunable, frequency-doubled Ti:Sapphire laser operating at 409.3 nm with a maximum power of 1 W and a repetition rate of 100 kHz. The second step targeted the excited population and leaded it to ionization non-resonantly. It was generated by a high power, frequency-tripled Q-switched Nd:YAG laser, showing a maximum power of 10 W at 355 nm. This laser was injected in the PI-LIST colinearly to the effusing cone. A detailed description of the experimental setup can be found in Fig. 6.5.

After setting the lasers we start the experiment by using a high precision oven to control the temperature of the monolithic diamond resonator. This was the same oven used in the previous experiments presented in sections 4.1, 4.2 and 5.2 and had an accuracy better than 10 mK which was used to tune the integrated diamond resonator. By scanning the temperature of the diamond and therefore the center Stokes frequency, we scan the transition measuring it's spectral profile.

6.4 Results

The integrated diamond resonator was scanned over a temperature range of $\Delta T = 4$ K. In Fig. 6.6 we can see the Stokes detuning with temperature while the inset shows the spectrum of the laser, with a measured linewidth at $\Delta\nu_S = 170$ MHz.

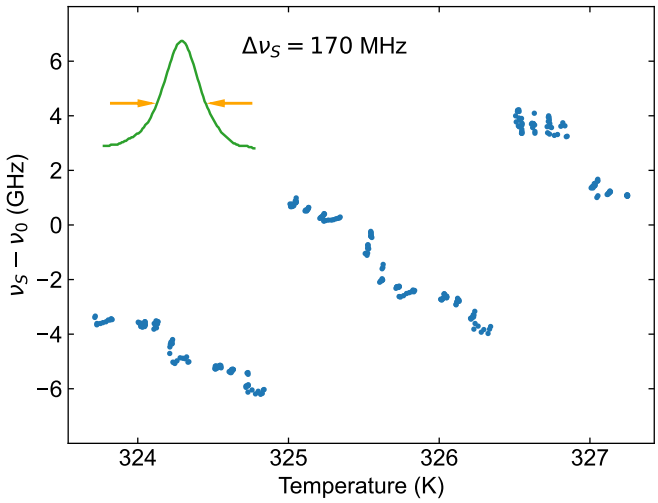

FIGURE 6.6: Stokes center frequency detuning with temperature. Inset: Spectrum of the Stokes output with a FWHM $\Delta\nu_S = 170$ MHz.

Compared to Figs. 4.3, 4.5 and 5.4, Fig. 6.6 appears irregular. The reason for this is due to the temperature scanning speed, which didn't allow for the resonator to fully stabilize before moving to the next temperature step.

By scanning the Stokes wavelength we obtain an ion current reading from the Faraday cups. In Fig. 6.7 we can see the ion current as a function of Stokes center frequency. The spectral response of the transition showed a Lorentzian profile with a FWHM linewidth around 1 GHz.

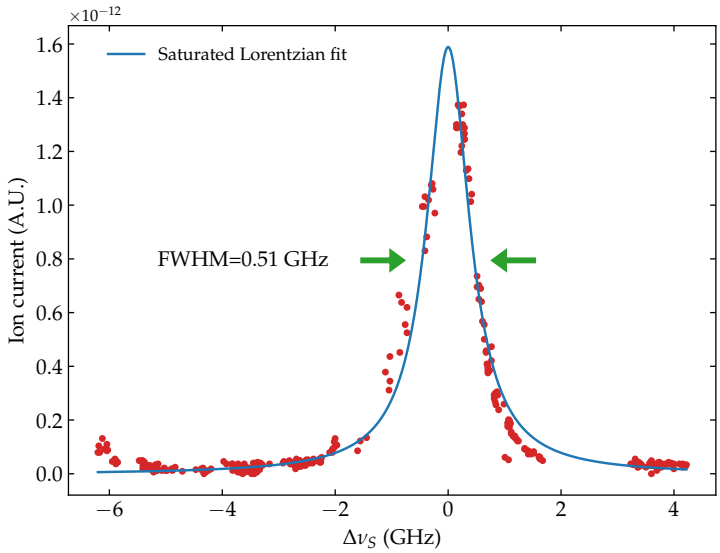

FIGURE 6.7: Ion current as a function of Stokes center frequency fitted with a saturated Lorentzian with FWHM 0.51 GHz.

The transition however was subjected to intense saturation due to high laser power which leads to broadening effects, increasing the linewidth. The function appropriate to account for the power broadening according to [50] is:

$$S(\omega, s) = \frac{1}{1 + L(\omega)/s} \tag{6.4}$$

were $L(\omega)$ is the Lorentzian profile and s the saturation constant. The fitting function was:

$$F(\omega, s) = L(\omega) \cdot S(\omega, s) \tag{6.5}$$

Fitting with this more appropriate function instead, resulted in a transition linewidth of 0.51 GHz. This resolution is appropiate of HR spectroscopy, allowing for hyperfine spectroscopy and isotope shift measurements. The demonstration establishes the role of the monolithic diamond resonator as a very promising tool for such experiments and related applications similar to ones mentioned in chapter 1.

Chapter 7

Conclusions and future work

7.1 Conclusions

Spectrally pure laser fields are of pivotal importance to high-precision applications. These laser sources have the potential to drive revolutionising technologies like quantum memories and quantum computers as well as play a crucial role in quantum metrology and nuclear physics research.

Ideal single-frequency laser sources are required to be characterised by widely-tunable, and highly-stable output while power-tolerance is not required but it's a very useful feature. This way, they can indeed be used effectively in the aforementioned applications. However, in conventional laser setups, adding these features, drastically increases complexity and results in bulky, time and money consuming devices that are in no way scalable, reducing the impact that these devices can have. For this reason we propose monolithic diamond resonators as a SLM source that fulfills all the above requirements while operating with Fourier-limited ns-pulses.

The tuning of the Stokes output of the integrated diamond resonator takes place through precise temperature control which results in a rate of change of $\partial\nu_S/\partial T \approx 3$ GHz/K at wavelength 479 nm and temperature 300 K. Stabilisation also happened through temperature, giving a stability better than < 52 MHz RMS when measuring for 16 hours. Overall this proved to be a reliable method for effective wavelength control and it should be the tuning method of choice for future experiments.

To hone the accuracy of our model, we further studied the not so well-known thermo-optic coefficient of diamond, emphasizing on the evolution of phononic vibrations with temperature. By using this data we developed an accurate model for $\partial\nu_S/\partial T$ which shall allow for use in even more sensitive applications.

Additionally we show that even though higher Q-resonators can further decrease the Stokes linewidth, this can already happen inside the monolithic diamond resonator. By operating in the doubly-resonant regime, we demonstrate a linewidth decrease of more than $\times 3$. This indicates that, using two tuning method at the same time, like temperature and pump injection angle, can potentially allow us to always operate in this regime, resulting in optimal spectral performance.

Finally, after establishing how to use the monolithic diamond resonator, we demonstrate its suitability for precision applications by performing high-resolution spectroscopy with it. The experiment scanned the spectral profile of the ground state of ^{152}Sm which naturally is a single narrow peak. The result was a peak with FWHM ≈ 1 GHz which was heavily affected by power broadening. By accounting for this, the scanned profile had a FWHM of 0.51 GHz, showing that HR spectroscopy is possible with this setup.

Concluding, we demonstrated the appropriate ways to tune this very useful and

versatile tool while at the same time we demonstrated that it is capable of performing HR spectroscopy. These results hold a strong promise to revolutionise technology by incorporating monolithic diamond resonators in scalable quantum applications.

7.2 Future work

The completion of this study paved the way to many potential implementations of this technology. A major step is incorporating it in RIS experiments at the ISOLDE facility of CERN, as a method for hyperfine and isotope shift measurements. This will shine light on some fundamental questions about the strong nuclear force by determining the shape, size, spin and electro-magnetic moments of the nucleus.

Moreover, the monolithic diamond resonator can be further improved in terms of spectral properties. A simple approach to this is increasing the Q factor of the cavity, i.e. by coating the edges of the resonator for a reflectivity higher than the Fresnel one. As a consequence the Stokes linewidth will decrease even more allowing for higher PSD values. When this is combined with appropriate control systems for constant doubly-resonant operation, we can expect to see very narrow-linewidths, appropriate for even the finest applications.

Last but not least, there are plans to render Stokes output more stable by operating in cryogenic temperatures. As indicated by [6], the thermo-optic coefficient tends to 0 at low temperatures, which renders $\partial \nu_S / \partial T$ much smaller allowing for extra stability.

As we have seen, the monolithic diamond resonator is an exceptional tool which also has room for great improvements. Concluding, science and technology will be greatly benefited by using this tool while at the same time developing it further.

Appendix A

Peer-reviewed articles

A.1 Influence of phonon harmonicity on spectrally pure resonant Stokes fields

Influence of phonon harmonicity on spectrally pure resonant Stokes fields

Georgios Stoikos [*] and Eduardo Granados [†]
CERN, 1217 Geneva, Switzerland

(Received 16 March 2022; accepted 21 July 2022; published 3 August 2022)

Due to their highly coherent emission, tunability, and compactness, integrated single-frequency diamond Raman lasers are interesting tools for applications in integrated quantum technology, high-resolution spectroscopy, or coherent optical communications. While the fundamental emission linewidth of these lasers can be Fourier limited, their thermo-optic characteristics lead to drifts in their carrier frequency, posing important challenges for applications requiring ultrastable emission. We propose here a method for measuring accurately the temperature-dependent index of refraction of diamond by employing standing Stokes waves produced in a monolithic Fabry-Pérot diamond Raman resonator. Our approach takes into account the influence of temperature on the first-order phonon line and the average lattice phonon frequency under intense stimulated Raman scattering conditions. We further utilize this model to calculate the value of the average phonon frequency and then the temperature-dependent thermo-optic coefficient. The theory is accompanied by the demonstration of tunable Fourier-limited Stokes nanosecond pulses with a stabilized center frequency deviation of less than 4 MHz.

DOI: 10.1103/PhysRevA.106.023504

I. INTRODUCTION

Spectrally pure, tunable, and ultrastable light sources have become one of the main tools for advancing scientific and technological quantum applications. These include the development of atomic clocks, LIDAR, or quantum ion computers to name a few [1,2]. The interest in building and integrating such light sources indicates the need for scalable architectures to cool, trap, and manipulate multiple ions simultaneously [3]. The main challenge here is in the complexity of producing widely tunable, high-performance narrow-band lasers (in tens of MHz and below) at a range of wavelengths from the UV to the near-IR.

In this regard, the field of diamond Raman lasers has experienced a renaissance since they can provide directly single-frequency light at nearly any optical wavelength [4–7]. Stimulated Raman scattering (SRS) has specific advantages that make it interesting for this task. For instance, the nonlinear process is mediated by propagating pump photons rather than via energy storage in localized ions, so there is no spatial hole burning or axial mode competition [7]. The phase-matching condition between pump and Stokes beams is automatically satisfied, and therefore the energy transfer relationship between waves depends on the shape and overlap of their temporal envelopes instead of their spectral distribution or phase characteristics. In certain cases, the Stokes spectrum can be driven to duplicate that of the pump spectrum in the so-called high-gain regime [8,9], which underpins the production of single-frequency nanosecond pulses when using spectrally broad pump lasers [10].

In addition, optical devices such as cavities, resonators, and optomechanical components realized in single-crystal diamond are poised to benefit from its extraordinary material properties. The interest in diamond is further propelled by its wide use for quantum applications [11], including quantum computing, generation of single photons [12], quantum sensing [13], and quantum memories [14]. Moreover, the production of tunable narrow-linewidth output from a Fabry-Pérot (FP) integrated diamond resonator was recently demonstrated, without the need of external mechanical feedback loops to control the cavity length [15].

Within this framework, knowledge of the thermo-optic coefficient is of paramount importance for integrated photonic devices based on diamond, and the present research was conducted with the purpose of gaining insight into accurate prediction of tuning the Stokes resonant frequency in integrated diamond resonators. Unfortunately, the existing approximations for the index of refraction render them insufficient for the level of accuracy required in the aforementioned applications.

When it comes to the refractive index of diamond, there have been many works relative to the optical and Raman properties of diamond, but there is a scarcity of information regarding the index of refraction under strong vibrational fields and at different temperatures. The work of Ruf *et al.* [16] provided valuable information for estimating the thermo-optic coefficient; however, it did not take into account the overall contribution of the different temperature-dependent vibrational modes that can be produced in diamond, and thus it needs to be expanded upon.

[*]Also at School of Applied Mathematics and Physical Sciences, National Technical University of Athens.
[†]eduardo.granados@cern.ch

We propose here an alternative methodology for measuring and calculating the thermo-optic coefficient. Our methodology includes the use of a monolithic single-frequency FP diamond Raman resonator operating at visible wavelengths. Here the accurate measurement of the output Stokes frequency as a function of temperature allows us to retrieve the temperature-dependent index of refraction that produced a frequency shift in the Stokes field output. For this method to be efficient, the use of diamond Raman monolithic resonators is important because they provide an ultrastable environment that depends exclusively on the resonator thermo-optic properties and not the pumping laser characteristics or the environment.

Additionally, we demonstrate that the production of tunable Fourier-limited Stokes few nanosecond pulses with a stabilized center frequency deviation of less than < 4 MHz is readily available, where the temperature stability of the bulk crystal is a key parameter for enhanced performance. Our theoretical model suggests that cooling the diamond resonator below 200 K may have additional advantages due to the reduced thermo-optic coefficient in that temperature range, enhanced gain, and reduced Raman linewidth.

II. MEASUREMENT PRINCIPLE

In terms of using the diamond bulk as a Raman laser material, its unique optical properties has enabled the development of lasers operating over a wide spectrum due to its giant Raman frequency shift (1332 cm^{-1}), large Raman gain ($>$ 40 cm/GW at 532 nm), and ultrawide transparency window (from deep ultraviolet all the way to THz, except for a lossy window from 2.6–6 μm due to multiphonon-induced absorption [8,17–21]). Furthermore, the excellent thermal properties afforded by diamond (unsurpassed thermal conductivity of 1800 W/m/K at 300 K and low thermo-optic coefficient of the order of 10^{-5} K^{-1}) along with negligible birefringence [22] make it an ideal material for high-power Raman lasing with greatly reduced thermal lensing effects at the kW average power level [23].

The generation of single longitudinal mode (SLM) or narrow linewidth light via SRS in diamond remained elusive until relatively recently [5,7,24–26]. Such bulk cavity systems also require precise alignment, elaborated feedback loops, and maintenance of optical components for the laser to function robustly. The further integration of SLM Raman lasers in diamond was recently demonstrated [10], showing that by embedding the laser resonator in the Raman media, it was possible to produce frequency stable output from a FP diamond resonator without the need of external mechanical feedback loops to control the cavity length. Moreover, these resonators performed complex functions such as "linewidth squeezing" when pumped by few GHz linewidth multimode lasers. Such mechanism, supported by phonon-resonant Raman interactions, directly enhanced the available power spectral density of broadband nanosecond lasers by nearly two orders of magnitude.

The frequency stabilization of these FP diamond resonators was carried out by adjusting the temperature of the diamond substrate, which simultaneously influenced the index of refraction, size, and Raman shift of the Raman resonator [15].

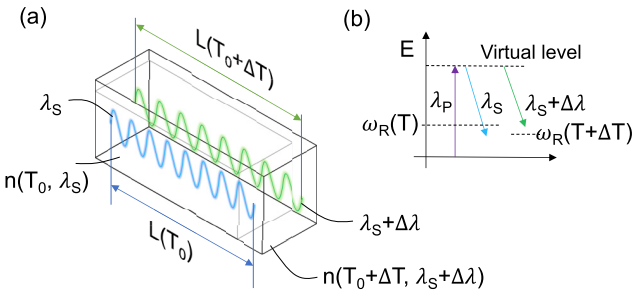

FIG. 1. (a) Schematic depiction of main thermal effects influencing the resonant Stokes frequency in a monolithic Raman resonator, and (b) depiction of the temperature effect on the photon and optical phonon energies.

In this work we shine light into that complex interplay of thermo-optical and Raman effects by studying their dependency on temperature, allowing us to construct a theoretical model capable of predicting with accuracy the resonating Stokes frequency. Our model is accompanied by an experimental demonstration showing excellent agreement with the proposed theory.

We start by identifying the main factors affecting the resonant Stokes frequency as well as their temperature dependency. Those are depicted in Fig. 1, where we have separated the temperature effects on the material optical properties and size [Fig. 1(a)] and the effects on the Raman shift center frequency ω_R [Fig. 1(b)]. In terms of the Stokes resonating frequency, the index of refraction depends simultaneously on the temperature and the chromatic dispersion $[n(T, \lambda)]$ due to the shifted Stokes wavelength $\lambda_S' = \lambda_S + \Delta\lambda(T)$. Note that all wavelengths used in this work are in vacuum. The thermal expansion process simultaneously affects the resonating wavelength due to the variable boundary condition [the diamond length $L(T)$ shifts to $L(T + \Delta T)$]. Likewise, the Raman shift center frequency $\omega_R(T)$ tuning with temperature does not establish the resonating wavelength or the tuning slope as a function of temperature, but it does affect the location of the boundaries of the longitudinal mode hopping in frequency. We describe all these effects in detail in the following sections, followed by the experimental results.

III. SINGLE-FREQUENCY OPERATION OF MONOLITHIC FABRY-PÉROT DIAMOND RAMAN RESONATORS

The production of single-frequency resonant Stokes fields depends on many factors, but most importantly on the characteristics of the pump laser intensity, wavelength, and linewidth, resonator optical length, and temporal envelope of the interplaying pump and Stokes pulses.

The temporal features of these laser fields, in both amplitude and phase on timescales shorter than the resonator round-trip time, are caused by the interference of its spectral longitudinal modes. These modes, however, generally vary in amplitude and phase on the timescale of the round-trip time or slower. Since the longitudinal modes vary slowly (much slower than the phonon dephasing time, in diamond $T_2 \approx 6.8$ ps), we can use steady-state Raman theory, even if interference of the modes produces structures that would

need transient Raman theory if modeled in the time domain. This approach has been used widely used to analyze SRS with broad-band lasers [27–33], and here we employ this method to model the diamond Raman resonator since it is computationally efficient for nanosecond pulses with GHz-class linewidths.

To construct the frequency domain model we follow the same strategy as in [10,27], but ultimately adapted to single-frequency pump fields. Nevertheless, the mathematical treatment is analogous, and here we include it for completeness. We start by writing the general equations for a fundamental field (or "pump") with $2m+1$ modes spaced in frequency by Ω_F, and a multimode Stokes field with $2m+1$ modes spaced in frequency by Ω_F:

$$\tilde{E}_F = \sum_{l=-m}^{m} F_l e^{i(\omega_{F(l)}t - k_{F(l)}z)} + \text{c.c.}, \tag{1}$$

$$\tilde{E}_S = \sum_{l=-m}^{m} S_l e^{i(\omega_{S(l)}t - k_{S(l)}z)} + \text{c.c.}, \tag{2}$$

in which c.c. represents the complex conjugate of the preceding term, $\omega_{S(l)} = \omega_{S(0)} + \Omega_F l$, and $\omega_{F(l)} = \omega_{F(0)} + \Omega_F l$. In these equations, S_l and F_l are complex amplitudes describing the amplitude and phase of the modes traveling inside the diamond. The approximations for the mode wave vector $k_{F(l)} \approx k_{F(0)} + \Omega_F l/u_F$ accounts for the group velocity difference between the fundamental wave packets, but neglect group velocity dispersion within each wave packet. Analogously for the Stokes field the mode wave vector $k_{S(l)} \approx k_{S(0)} + \Omega_F l/u_S$.

In the following we assume that the central Stokes mode S_0 is centered within the Raman gain linewidth so that it accesses the highest or monochromatic Raman gain. Note that in our model the following identity is always true:

$$\omega_{F(l)} = \omega_{S(l)} + \omega_R; \tag{3}$$

here ω_R is the frequency of the Raman shift at the line center. This essentially is to say that the modes of fundamental and Stokes fields are paired. In order to describe the coupling between this set of modes, we rely on steady-state Raman formalism and write it in a nondegenerate mode for four generic modes F_{l_1}, F_{l_2}, S_{l_3}, and S_{l_4}:

$$\frac{1}{u_S}\frac{\partial S_{l_4}}{\partial t} \pm \frac{\partial S_{l_4}}{\partial z} \propto F_{l_1}\left(F_{l_2}^* S_{l_3}\right). \tag{4}$$

This was interpreted in [27] as two modes $(F_{l_2}^* S_{l_3})$ driving a phonon field and a third mode F_{l_1} scattering off the phonon field to drive a fourth mode S_{l_4}. For fundamental and Stokes pulsed fields with many longitudinal modes or broadband modes, in principle all types of interactions can drive a polarization at the frequency of a generic mode S_{r_2}, given that they satisfy the equation

$$\omega_{S_{r_2}} = \omega_{F_{l_1}} - \omega_{F_{l_2}} + \omega_{S_{r_1}}. \tag{5}$$

Now Eq. (4) can be used as template to reformulate the amplification of a generic Stokes mode S_l and the depletion of the fundamental modes F_l as a function of the other three interacting waves as follows:

$$\frac{1}{u_S}\frac{\partial S_l}{\partial t} + \frac{\partial S_l}{\partial z} = 2cn_F\epsilon_0\frac{g_0}{2}\sum_r\sum_j F_{l-r}(S_j F_{j-r}^*) \times \frac{\Delta\omega_R}{\Delta\omega_R - ir\Omega_F} e^{i(l-j)\mu_\pm\Omega_F z}, \tag{6}$$

$$\frac{1}{u_F}\frac{\partial F_l}{\partial t} + \frac{\partial F_l}{\partial z} = -2cn_S\epsilon_0\frac{g_0}{2\eta}\sum_r\sum_j S_{l-r}(F_j S_{j-r}^*) \times \frac{\Delta\omega_R}{\Delta\omega_R + ir\Omega_F} e^{i(j-l)\mu_\pm\Omega_F z}. \tag{7}$$

The parameter $\mu_\pm$ is the group delay difference per meter between the fundamental and Stokes waves. The positive part μ_+ accounts for copropagating waves or forward SRS and the negative μ_- for the backward SRS:

$$\mu_\pm = \frac{1}{u_F} \mp \frac{1}{u_S}. \tag{8}$$

Equations (6) and (7) account for all the combinations between pump and Stokes modes. The resulting spectra for the Stokes field are dependent on the relative amplitudes of the resonant and nonresonant terms. The resonant terms ($r = 0$) have the phonon driving term exactly resonant with the phonon frequency and can access the highest gain, while other nonresonant interactions have a detuning $r\Omega_F$ that reduces gain and causes a phase rotation. For our model, both resonant and nonresonant interactions need to be taken into account since $\Delta\omega_R > \Omega_F$.

Degenerate terms ($j = l$) have no phase mismatch terms ($\Delta k = 0$) even in the presence of dispersion, and because of the degeneracy these terms must always have the correct phase to provide gain. Nondegenerate modes, however, can be neglected in dispersive media where the phase mismatch is $\Delta k \approx (l-j)\Omega_F\mu_\pm$, and so these terms will oscillate in and out of phase with the waves they drive. Here we assume that dispersion in diamond is large enough in the UV and visible spectral ranges to neglect nondegenerate mixing modes without loss of accuracy. With this approximation, we can rewrite Eqs. (6) and (7) forcing $j = l$. Likewise, for the specific case of single longitudinal mode pumping, the equations can be further simplified to

$$\frac{1}{u_S}\frac{\partial S_l}{\partial t} + \frac{\partial S_l}{\partial z} = 2cn_F\epsilon_0\frac{g_0}{2}F_0(S_l F_0^*)\frac{\Delta\omega_R}{\Delta\omega_R + il\Omega_F}, \tag{9}$$

$$\frac{1}{u_F}\frac{\partial F_0}{\partial t} + \frac{\partial F_0}{\partial z} = -2cn_S\epsilon_0\frac{g_0}{2\eta}\sum_r S_r(F_0 S_r^*)\frac{\Delta\omega_R}{\Delta\omega_R + ir\Omega_F}. \tag{10}$$

The term $\Delta\omega_R/(\Delta\omega_R - ir\Omega_F)$ reduces the gain of off-resonant terms by a Lorentzian factor $1 + (r\Omega_F/\Delta\omega_R)^2$, and therefore the most efficient interaction is always for doubly degenerate resonant interactions.

Let's assume now that the combination of pump intensity and resonator losses is adequate so that the amplification is highly preferential for the central mode S_0 as in [10] and is capable of depleting the fundamental field. This configuration will produce the minimal linewidth for a given resonator round-trip loss and can also occur when the FSR of the

diamond resonator is larger than the effective Raman gain linewidth. A way of calculating the resulting Stokes linewidth is by further simplifying Eqs. (9) and (10) by implying $\{S_l = 0 \forall l \neq 0\}$:

$$\frac{1}{u_S}\frac{\partial S_0}{\partial t} + \frac{\partial S_0}{\partial z} = 2cn_F\epsilon_0\frac{g_0}{2}|F_0|^2 S_0, \tag{11}$$

$$\frac{1}{u_F}\frac{\partial F_0}{\partial t} + \frac{\partial F_0}{\partial z} = -2cn_S\epsilon_0\frac{g_0}{2\eta}|S_0|^2 F_0. \tag{12}$$

We can now use Eqs. (11) and (12) to model the dynamic interplay between fundamental and Stokes waves in the Raman resonator when the fields are located at the Raman gain line center. Intuitively, it is possible to see in Eq. (11) that the temporal envelope of the Stokes field depends only on the amplitude of the fundamental pumping pulse and not its phase, whereas the resonating Stokes wavelength will depend only on the resonator geometry and optical characteristics and not the pump field. The resulting Stokes linewidth, however, will be directly linked to the pump pulse temporal envelope and dispersion characteristics of the resonator, the generation of nearly Fourier-limited pulses when low-noise pump pulses are used is relatively straightforward.

For the case of a temperature tuned Stokes frequency, the mismatch between the Raman gain line center and the resonating Stokes field will produce a reduced gain by a factor $1 + (\Delta\omega_S(T)/\Delta\omega_R)^2$ due to the detuned Stokes mode. Here $\Delta\omega_S(T)$ is the frequency shift produced in the resonator due to temperature. The calculation of this shift is described in the next section.

IV. RELATIONSHIP BETWEEN THE STOKES CENTER FREQUENCY AND THE REFRACTIVE INDEX

Knowledge of diamond's optical and mechanical properties runs deep for most factors, with an exception being the temperature dependence of the refractive index (also known as thermo-optic coefficient), despite its importance for optical applications or integrated photonic devices in diamond. In the literature it is usually found as a single value of $(1/n)\partial n/\partial T = 5 \times 10^{-6}$ K^{-1} at 300 K for the low-frequency limit [34] or in the far-infrared range for a temperature range of up to 925 K [16]. Precise information regarding the thermo-optic coefficient of diamond at visible wavelengths and at extended temperature ranges remains relatively unknown.

A thorough theoretical description on the thermo-optic coefficient in diamond is a great challenge since it requires a working model for the dielectric function and its renormalization by the electron-phonon interaction and the thermal expansion of the lattice [16]. There have been models using empirical pseudopotentials for the thermo-optic coefficients of different semiconductors, but since C has a large Debye temperature $\Theta_D = 1880$ K, knowledge of the thermo-optic coefficient at 300 K does not provide meaningful information for higher temperatures [35]. The inaccuracy is caused by the fact that a linear approximation of the temperature-dependent index of refraction $n(T)$ is permitted at temperatures much larger than Θ_D where the material can be described by a single oscillator frequency.

In the following we present a methodology for the calculation of the Stokes frequency and its tuning slope for a generic monolithic Raman resonator longitudinal mode and its relation to the temperature-dependent refractive index. We start with the condition for resonance within the diamond FP resonator:

$$\nu_S(T_0) = q\frac{c}{2L_{\text{eff}}(T_0, \nu_S)}, \tag{13}$$

where q is the mode number, c is the speed of light in vacuum, and $L_{\text{eff}}(T_0, \nu_S)$ is the effective length of the resonator at the Stokes resonating frequency ν_S and at temperature T_0. L_{eff} can be calculated as $L_{\text{eff}}(T_0, \nu_S) = L(T_0)n(\lambda_S, T_0)$, where $n(\lambda_S, T_0)$ is the wavelength-temperature dependent index of refraction, and $L(T_0)$ is the resonator physical length at temperature T_0. In [16] the temperature-dependent part of the refractive index $n_T(T)$ was separated from the wavelength-dependent part $n_\lambda(\lambda)$. The two terms are added together to give the total index of refraction as

$$n(\lambda, T) = n^0_\lambda(\lambda) + n_T(T). \tag{14}$$

We note that $n^0_\lambda(\lambda)$ refers to the Sellmeier equation at 0 K, and $n_T(T)$ represents the change of index due to temperature at a fixed wavelength. For small shifts in temperature (ΔT) we can use a perturbation theory approach to estimate the resulting wavelength shift of the Stokes by

$$\lambda_S(T_0 + \Delta T) = \frac{2}{q}\left(L(T_0) + \frac{\partial L}{\partial T}\Delta T\right) \times \left(n(T_0, \lambda_S) + \frac{\partial n}{\partial T}\Delta T + \frac{\partial n}{\partial \lambda}\Delta\lambda_S\right). \tag{15}$$

Here the term $\partial L/\partial T$ can be expressed in terms of the linear thermal expansion coefficient (α in the following) as $\partial L/\partial T = \alpha L(T_0)$. The shift in wavelength can be directly calculated by $\Delta\lambda_S = \lambda_S(T_0 + \Delta T) - \lambda_S(T_0)$. The terms $\partial n/\partial T$ and $\partial n/\partial\lambda$ correspond to the thermo-optic coefficient at T_0 and the chromatic dispersion at λ_S, respectively. Here we assume that dispersion terms do not change for small temperature increments ΔT.

Reorganizing Eq. (15) and neglecting second-order differential terms, we can obtain the tuning slope of the center Stokes wavelength as a function of temperature:

$$\frac{\partial \nu_S}{\partial T}\Big|_{T_0} = -c\frac{\frac{1}{n}\frac{\partial n_T}{\partial T} + \alpha(T)}{\lambda_S\left(1 - \frac{\lambda_S}{n}\frac{\partial n_\lambda}{\partial \lambda}\right)}, \tag{16}$$

where c is the speed of light in vacuum, n the index of refraction of diamond at the Stokes wavelength and at temperature T_0, and $\alpha(T)$ the temperature-dependent thermal expansion coefficient of CVD diamond. Jacobson *et al.* modeled $\alpha(T)$ in [36] having the following form:

$$\alpha(T) = \sum_{i=1}^{n} X_i E\left(\frac{\Theta_i}{T}\right), \tag{17}$$

where $E(x)$ corresponds to the function given by

$$E(x) = \frac{x^2 e^x}{(e^x - 1)^2}. \tag{18}$$

Experimental values for X_i and Θ_i can be found in [36], and those are the ones used here for the calculations.

Continuing, $\frac{1}{n}\frac{\partial n_T}{\partial T}$ is the thermo-optic coefficient. Typical values for this coefficient in the literature are approximately 5×10^{-6} K^{-1} [34]. The key part here is in the understanding of the temperature-dependent term $n_T(T)$, which requires one to identify the effects that influence it. In general, the index of refraction depends on the lattice energy, which here it is assumed to be proportional to the internal energy of the system [37]. For diamond, it is possible to use a Bose-Einstein distribution to describe the unit cell infrared active vibration [38].

As a consequence, we can refer to the approximation of the temperature-dependent index of refraction as $n_T(T)$ described in [16]:

$$n_T(T) = A\left(\frac{1}{e^{\frac{\hbar\omega_0}{k_B T}} - 1} + \frac{1}{2}\right) \tag{19}$$

with the first term being the Bose-Einstein distribution. Ruf *et al.* [16] estimated the values of A and $\hbar\omega_0$ based on fits of the data to their experimental measurements. Their results retrieved a value of $A = 0.01902$ and an average phonon frequency of $\hbar\omega_0 = 711$ cm^{-1}, independent of temperature. Even though the results in that work fit well their experiments, the influence of the thermal expansion of the lattice to the vibrational eigenfrequencies and multiphonon coupling effects (see, for example, [39]) were not taken into account, nor their contribution to the line shift of the average phonon frequency ω_0.

When it comes to the wavelength-dependent part of the index of refraction $n_\lambda(\lambda)$, we are basing our model in the most recent single-term Sellmeier equation found for synthetic diamond [40]. The Sellmeier equation is usually calculated at room temperature (300 K), but the separable equation for the index of refraction in Eq. (14) requires the index at absolute zero temperature. To that end, we approximated $n^0_\lambda(\lambda)$ as follows:

$$n^0_\lambda(\lambda) = n_\lambda(\lambda) - n_T(300). \tag{20}$$

The factor $n_T(300)$ was calculated using Eq. (14) at 300 K. In this way we also guarantee that the index of refraction is the one commonly known at room temperature.

In terms of the temperature dependence of the Raman shift, it defines the spectral range where the monolithic resonator will lase, although not the specific frequency of the Stokes standing waves. Having this in mind, we present here for completeness the dependency of the first-order phonon frequency (or Raman shift) on temperature. The Klemens anharmonic approximation assumes that the zone-center phonon decay into two acoustical phonons of opposite momentum is appropriate to describe the effects in the diamond lattice [41,42]. In that model the relaxation time τ is

$$\tau \simeq 1 + \frac{2}{e^{\frac{\hbar}{k_B T}\frac{\omega_R}{2}} - 1}, \tag{21}$$

where ω_R is the Raman shift. The relaxation time τ is proportional to the Raman linewidth $\Delta\omega_R$ and that later is linearly connected to the Raman shift [43]. The temperature-dependent Raman shift is then given by

$$\omega_R(T) = 1332.7 - A_R\left(\frac{2}{e^{\frac{\hbar\omega_R}{2k_B T}} - 1}\right)\frac{10^7}{c}\,[\text{cm}^{-1}], \tag{22}$$

where A_R depends on the dispersion lines of diamond [43]. A fit to the experimental data shown in [44] resulted in $A_R = 2.6 \times 10^3$ GHz. We are now ready to experimentally measure $\partial\nu_S/\partial T$ and fit it to our model, allowing us to extract the thermo-optical coefficient of diamond.

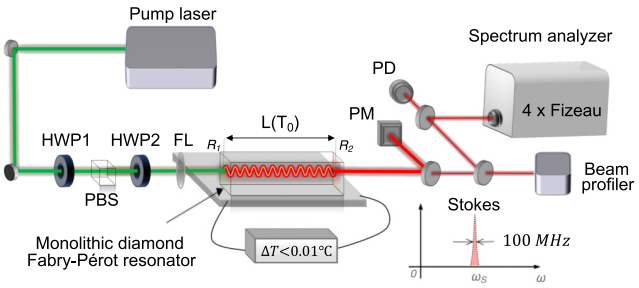

FIG. 2. Schematic layout of the experimental setup: A monolithic diamond resonator is pumped by a frequency-doubled Q-switched Nd:YAG laser. The output Stokes nanosecond pulse was characterized temporally and spectrally with a set of four high-resolution Fizeau interferometers, and a photodiode (PD) connected to a large bandwidth 16 GHz oscilloscope. HWP1, HWP2: half-wave plates; PBS: polarizing beam splitter; FL: focusing lens; PM: power meter.

V. EXPERIMENT

In order to confirm our method, we have set up an experiment to analyze the Stokes resonant frequency in the resonator as a function of temperature with high accuracy. From these data we can then relate the constants and tuning slope-related physical parameters.

A temperature-adjustable monolithic FP diamond resonator was used in our experiments as the tool for measuring

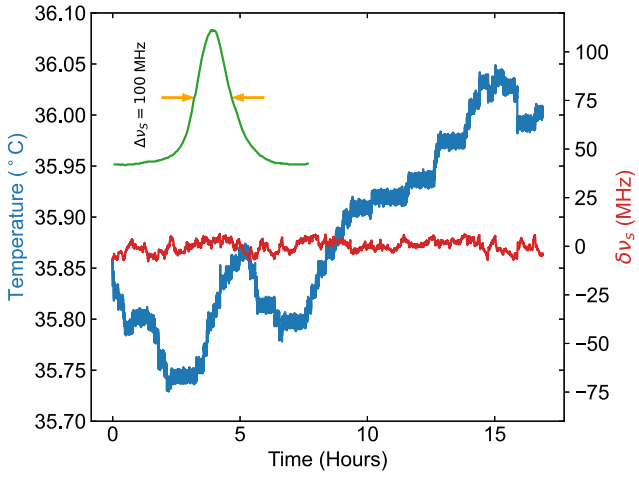

FIG. 3. Active temperature stabilization of the Stokes resonant frequency over more than 16 h. The RMS fluctuation of the Stokes frequency is less than 4 MHz. Inset: Measured Stokes field spectrum.

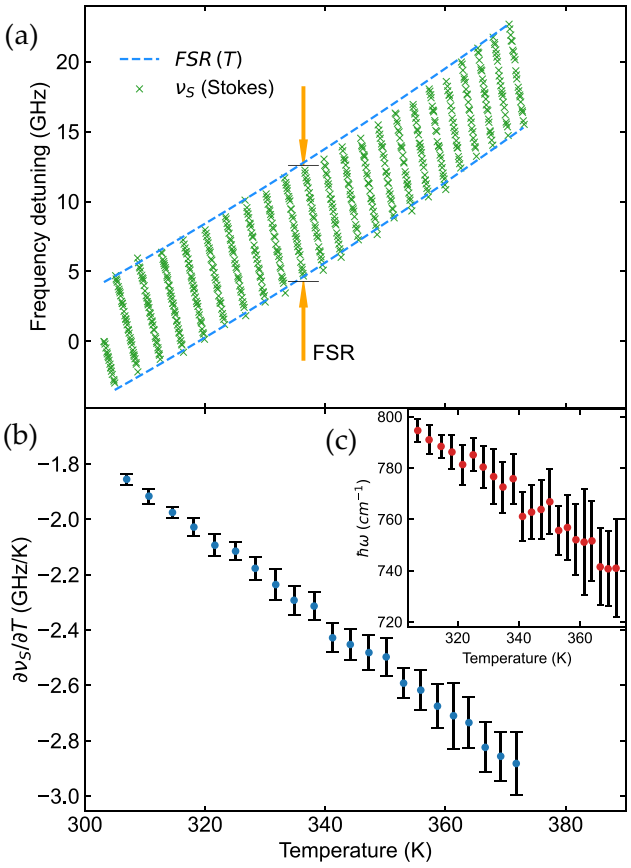

FIG. 4. (a) Stokes center frequency (ν_S) detuning as a function of measured diamond temperature. Dashed blue line represents the tuning range (FSR) of the Stokes frequency as a function of temperature. (b) Measured tuning slope for each FSR as a function of temperature. (c) Calculated average phonon frequencies by solving Eq. (16).

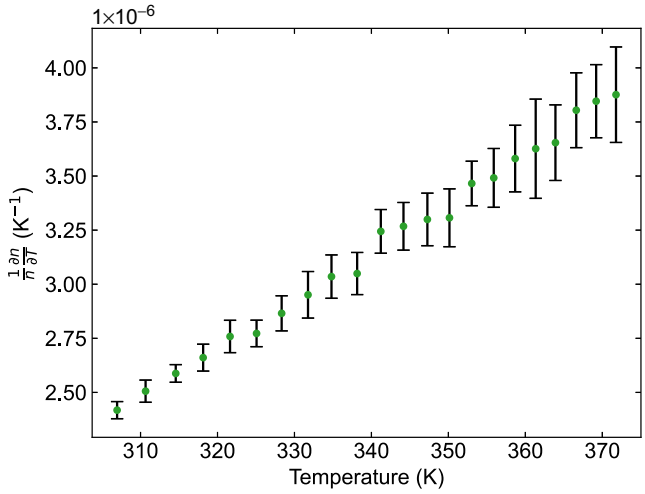

FIG. 5. Calculated thermo-optic coefficient of diamond as a function of temperature between 300 and 370 K using the solutions of Eq. (16).

the optical properties of diamond under stimulated Raman scattering conditions. The Raman medium was a synthetic diamond cuboid crystal with dimensions $7 \times 2 \times 2$ mm^3 (FSR at 573 nm ≈ 8 GHz), plane cut for beam propagation along the 110 axis, and end faces repolished with a parallelism better than 0.5 μm/mm. The experimental setup can be appreciated in Fig. 2.

Due to the high Raman gain of diamond at 532 nm, the Fresnel reflectivity of the uncoated surfaces ($R_1, R_2 \approx 18\%$) was sufficient to ensure highly efficient Raman operation. The diamond crystal was placed on a copper mount inside a high-precision oven (Covesion Ltd), with a temperature standard deviation of less than < 10 mK. Note that the relatively small thermal expansion coefficient of diamond [36,45] and dispersion [46] provided the necessary stability and robustness to perform our measurements accurately.

The pump is a frequency-doubled Nd:YAG 532 nm laser generating 10 ns pulses at a repetition rate of 100 Hz with an energy of 50 μJ. The pulses passed through a power control system consisting of a half-wave plate (HWP1) and polarizing beam splitter (PBS). The polarization was controlled by means of another half-wave plate (HPW2); note that the SRS process efficiency depends on polarization and is maximized when the pump polarization angle is parallel to the 111 crystallographic axis. The pump then arrives at the resonator and goes through the SRS process.

The pump was focused into the diamond crystal by a 150 mm focal length lens (FL), producing a waist of 50 ± 5 μm in diameter and a resulting intensity of 0.1 GW/cm^2. After the generation of the first and second Stokes we used dichroics to filter the undesired Stokes orders. The resulting 573 nm beam was then guided to the wavemeter, calibrated power meter (PM), photodiode (PD), and beam profiler. The linewidth (FWHM) of the 573 nm Stokes light was measured with a wavelength meter LM-007 wavemeter and was 100 ± 20 MHz averaged over ~1000 shots (shown inset in Fig. 3), whereas the center frequency deviation ($\delta\nu_S$) had an root-mean-square value < 4 MHz over more than 16 h when actively stabilized using temperature as shown in Fig. 3.

The results of the measurement of the resonating Stokes wavelength with temperature are shown in Fig. 4(a). The tests were carried out by adjusting the temperature setting of the oven in increments of 10 mK. The average frequency-temperature tuning slope within a FSR of the resonator was approximately $\partial\nu_S/\partial T \approx -2.3$ GHz/K, whereas the temperature dependence of the first-order Raman phonon line was about $\partial\nu_R/\partial T \approx +0.23$ GHz/K. This agrees reasonably with calculations resulting from the Klemens model ($\approx +0.2$ to 0.25 GHz/K between 300 and 400 K).

Figure 4(b) shows the measured slope in each FSR as a function of temperature. It can be appreciated that the overall tuning slope increases in absolute value as a function of temperature due to the temperature dependency of the thermo-optic coefficient. The slope in the tuning curves varies significantly from -1.8 GHz/K to -2.8 GHz/K in about 70 K. The error bars represent the 99% confidence interval. The noticeable correlation between temperature and error can lead to the misconception that error is systemic. In reality the reason is that fewer measurements were taken at higher temperatures due to the nonlinear speed of the temperature scan.

We used the values of the slope to calculate then the average phonon frequency $\hbar\omega(T)$ of each FSR by solving Eq. (16). Figure 4(c) shows the computed values for the phonon frequency $\hbar\omega(T)$ for each FSR.

We can now proceed to estimate the thermo-optic coefficient directly by deriving Eq. (19) with the values measured for the temperature-dependent average phonon frequency $\hbar\omega(T)$. The result of this is shown in Fig. 5. It is important to note that the apparent similarity between Figs. 4 and 5 is due to the weak temperature dependence of the factors of Eq. (16); however, the relationship between them is not linear. Interestingly, the range where the temperature-dependent index of refraction is nonlinear is most severe for temperatures in the range from 200 to 400 K. Below 200 K, $(1/n)\partial n/\partial T$ is nearly zero, whereas for values above 400 K it asymptotically tends to a constant value, and from our extrapolations tending to approximately 8×10^{-6} K^{-1} at high temperatures above 500 K.

VI. CONCLUSIONS

In this work we studied the relationship between the resonant Stokes wavelength inside a monolithic diamond Raman resonator and temperature. We found that existing models for the temperature dependency of diamond's refractive index correspond only approximately to observed experimental processes; however, the accuracy in their predictions is poorer in the 300–400 K range, and hence here we experimentally measured it. Since $\partial\nu_S/\partial T$ depends directly on the thermo-optic coefficient, we propose to scan the temperature while measuring the resonant Stokes wavelength to recalculate the thermal dependency of diamond's index of refraction in the visible spectral range.

Regarding the flexibility of the proposed method, the combination of very narrow spectral bandwidth and resulting high spectral density from the resonator, alongside the large transparency range of diamond, makes it very versatile and useful at a large range of wavelengths and temperatures. In fact, the constructed Raman laser is characterized by its modest requirements in terms of resonator quality factors, which readily allow for stable and portable operation usable in scientific applications.

Furthermore, we propose a model for estimating the average lattice phonon frequency of diamond under strong SRS conditions. We expect that the presented method and measured diamond thermo-optical parameters will be useful for research related to the development of temperature-sensitive integrated photonic devices in diamond.

[1] N. Chauhan, A. Isichenko, K. Liu, J. Wang, Q. Zhao, R. O. Behunin, P. T. Rakich, A. M. Jayich, C. Fertig, C. W. Hoyt, and D. J. Blumenthal, Visible light photonic integrated Brillouin laser, Nat. Commun. **12**, 4685 (2021).

[2] Y. Hu, M. Yu, D. Zhu, N. Sinclair, A. Shams-Ansari, L. Shao, J. Holzgrafe, E. Puma, M. Zhang, and M. Lončar, On-chip electro-optic frequency shifters and beam splitters, Nature (London) **599**, 587 (2021).

[3] K. K. Mehta, C. Zhang, M. Malinowski, T.-L. Nguyen, M. Stadler, and J. P. Home, Integrated optical multi-ion quantum logic, Nature (London) **586**, 533 (2020).

[4] X. Yang, Z. Bai, D. Chen, W. Chen, Y. Feng, and R. P. Mildren, Widely-tunable single-frequency diamond Raman laser, Opt. Express **29**, 29449 (2021).

[5] S. Sarang, O. Kitzler, O. Lux, Z. Bai, R. J. Williams, D. J. Spence, and R. P. Mildren, Single-longitudinal-mode diamond laser stabilization using polarization-dependent Raman gain, OSA Continuum **2**, 1028 (2019).

[6] X. Yang, O. Kitzler, D. J. Spence, R. J. Williams, Z. Bai, S. Sarang, L. Zhang, Y. Feng, and R. P. Mildren, Single-frequency 620 nm diamond laser at high power, stabilized via harmonic self-suppression and spatial-hole-burning-free gain, Opt. Lett. **44**, 839 (2019).

[7] O. Lux, S. Sarang, R. J. Williams, A. McKay, and R. P. Mildren, Single longitudinal mode diamond Raman laser in the eye-safe spectral region for water vapor detection, Opt. Express **24**, 27812 (2016).

[8] D. T. Echarri, K. Chrysalidis, V. N. Fedosseev, B. A. Marsh, R. P. Mildren, S. M. Olaizola, D. J. Spence, S. G. Wilkins, and E. Granados, Broadly tunable linewidth-invariant Raman stokes comb for selective resonance photoionization, Opt. Express **28**, 8589 (2020).

[9] K. Chrysalidis, V. N. Fedosseev, B. A. Marsh, R. P. Mildren, D. J. Spence, K. D. A. Wendt, S. G. Wilkins, and E. Granados, Continuously tunable diamond Raman laser for resonance laser ionization, Opt. Lett. **44**, 3924 (2019).

[10] E. Granados, C. Granados, R. Ahmed, K. Chrysalidis, V. N. Fedosseev, B. A. Marsh, S. G. Wilkins, R. P. Mildren, and D. J. Spence, Spectral synthesis of multimode lasers to the Fourier limit in integrated Fabry–Pérot diamond resonators, Optica **9**, 317 (2022).

[11] T. Teraji, Ultrapure homoepitaxial diamond films grown by chemical vapor deposition for quantum device application, in *Diamond for Quantum Applications Part 1*, Semiconductors and Semimetals, Vol. 103, edited by C. E. Nebel, I. Aharonovich, N. Mizuochi, and M. Hatano (Elsevier, Cambridge, MA, 2020), pp. 37–55.

[12] E. Neu and C. Becher, Diamond-based single-photon sources and their application in quantum key distribution, in *Quantum Information Processing with Diamond*, edited by S. Prawer and I. Aharonovich (Woodhead Publishing, 2014), pp. 127–159

[13] M. Markham, A. Edmonds, A. Bennett, P.-O. Colard, W. Hillman, and M. Jaszczykowski, CVD diamond for quantum applications, in *Symposium Latsis 2019 on Diamond Photonics—Physics, Technologies and Applications* (Optical Society of America, 2019), p. 135.

[14] D. D. Sukachev, A. Sipahigil, C. T. Nguyen, M. K. Bhaskar, R. E. Evans, F. Jelezko, and M. D. Lukin, Silicon-Vacancy Spin Qubit in Diamond: A Quantum Memory Exceeding 10 ms with Single-Shot State Readout, Phys. Rev. Lett. **119**, 223602 (2017).

[15] E. Granados, G. Stoikos, D. T. Echarri, K. Chrysalidis, V. N. Fedosseev, C. Granados, V. Leask, B. A. Marsh, and R. P. Mildren, Tunable spectral squeezers based on monolithically

integrated diamond Raman resonators, Appl. Phys. Lett. **120**, 151101 (2022).
[16] T. Ruf, M. Cardona, C. S. J. Pickles, and R. Sussmann, Temperature dependence of the refractive index of diamond up to 925K, Phys. Rev. B **62**, 16578 (2000).
[17] E. Granados, D. J. Spence, and R. P. Mildren, Deep ultraviolet diamond Raman laser, Opt. Express **19**, 10857 (2011).
[18] R. P. Mildren and A. Sabella, Highly efficient diamond Raman laser, Opt. Lett. **34**, 2811 (2009).
[19] D. J. Spence, E. Granados, and R. P. Mildren, Mode-locked picosecond diamond Raman laser, Opt. Lett. **35**, 556 (2010).
[20] W. Lubeigt, G. M. Bonner, J. E. Hastie, M. D. Dawson, D. Burns, and A. J. Kemp, Continuous-wave diamond Raman laser, Opt. Lett. **35**, 2994 (2010).
[21] A. Sabella, J. A. Piper, and R. P. Mildren, Diamond Raman laser with continuously tunable output from 3.38 to 3.80 μm, Opt. Lett. **39**, 4037 (2014).
[22] I. Friel, S. L. Geoghegan, D. J. Twitchen, and G. A. Scarsbrook, Development of high quality single crystal diamond for novel laser applications, Proc. SPIE **7838**, 783819 (2010).
[23] S. Antipov, A. Sabella, R. J. Williams, O. Kitzler, D. J. Spence, and R. P. Mildren, 1.2 kW quasi-steady-state diamond Raman laser pumped by an $m^2 = 15$ beam, Opt. Lett. **44**, 2506 (2019).
[24] O. Lux, S. Sarang, O. Kitzler, D. J. Spence, and R. P. Mildren, Intrinsically stable high-power single longitudinal mode laser using spatial hole burning free gain, Optica **3**, 876 (2016).
[25] O. Kitzler, J. Lin, H. M. Pask, R. P. Mildren, S. C. Webster, N. Hempler, G. P. A. Malcolm, and D. J. Spence, Single-longitudinal-mode ring diamond Raman laser, Opt. Lett. **42**, 1229 (2017).
[26] M. Li, O. Kitzler, and D. J. Spence, Investigating single-longitudinal-mode operation of a continuous wave second stokes diamond Raman ring laser, Opt. Express **28**, 1738 (2020).
[27] D. J. Spence, Spectral effects of stimulated Raman scattering in crystals, Prog. Quantum Electron. **51**, 1 (2017).
[28] G. P. Dzhotyan, Y. E. D'yakov, I. G. Zubarev, A. B. Mironov, and S. I. Mikhaĭlov, Influence of the spectral width and statistics of a stokes signal on the efficiency of stimulated Raman scattering of nonmonochromatic pump radiation, Sov. J. Quantum Electron. **7**, 783 (1977).
[29] V. G. Sidorovich, Reproduction of the pump spectrum in stimulated Raman scattering, Sov. J. Quantum Electron. **8**, 784 (1978).
[30] W. Trutna, Y. Park, and R. Byer, The dependence of Raman gain on pump laser bandwidth, IEEE J. Quantum Electron. **15**, 648 (1979).
[31] C. Warner and B. Bobbs, Effects of off-resonant Raman interactions on multimode Stokes conversion efficiency and output wave front, J. Opt. Soc. Am. B **3**, 1345 (1986).
[32] L. A. Westling and M. G. Raymer, Intensity correlation measurements in stimulated Raman generation with a multimode laser, Phys. Rev. A **36**, 4835 (1987).
[33] Y. Xiong, S. Murphy, J. L. Carlsten, and K. Repasky, Theory of a far-off resonance mode-locked Raman laser in H_2 with high finesse cavity enhancement, J. Opt. Soc. Am. B **24**, 2055 (2007).
[34] J. Fontanella, R. L. Johnston, J. H. Colwell, and C. Andeen, Temperature and pressure variation of the refractive index of diamond, Appl. Opt. **16**, 2949 (1977).
[35] P. Y. Yu and M. Cardona, Temperature coefficient of the refractive index of diamond- and zinc-blende-type semiconductors, Phys. Rev. B **2**, 3193 (1970).
[36] P. Jacobson and S. Stoupin, Thermal expansion coefficient of diamond in a wide temperature range, Diam. Relat. Mater. **97**, 107469 (2019).
[37] P. Hervé and L. K. J. Vandamme, General relation between refractive index and energy gap in semiconductors, Infrared Phys. Tech. **35**, 609 (1994).
[38] R. Loudon, The Raman effect in crystals, Adv. Phys. **13**, 423 (1964).
[39] J. González, E. Moya, and J. C. Chervin, Anharmonic effects in light scattering due to optical phonons in $CuGaS_2$, Phys. Rev. B **54**, 4707 (1996).
[40] G. Turri, S. Webster, Y. Chen, B. Wickham, A. Bennett, and M. Bass, Index of refraction from the near-ultraviolet to the near-infrared from a single crystal microwave-assisted CVD diamond, Opt. Mater. Express **7**, 855 (2017).
[41] P. G. Klemens, Anharmonic decay of optical phonons, Phys. Rev. **148**, 845 (1966).
[42] A. Debernardi, S. Baroni, and E. Molinari, Anharmonic Phonon Lifetimes in Semiconductors from Density-Functional Perturbation Theory, Phys. Rev. Lett. **75**, 1819 (1995).
[43] M. S. Liu, L. A. Bursill, S. Prawer, and R. Beserman, Temperature dependence of the first-order Raman phonon line of diamond, Phys. Rev. B **61**, 3391 (2000).
[44] V. Leask, A continuously tunable single longitudinal mode diamond Raman laser, Master's thesis, SUPA Department of Physics, University of Strathclyde, Glasgow, 2019.
[45] C. Moelle, S. Klose, F. Szcs, H. Fecht, C. Johnston, P. Chalker, and M. Werner, Measurement and calculation of the thermal expansion coefficient of diamond, Diam. Relat. Mater. **6**, 839 (1997).
[46] Diamond Materials, *The CVD Diamond Booklet* (Diamond Materials, Advanced Diamond Technology, Freiburg, 2004), https://www.diamond-materials.com/site/assets/files/1095/cvd_diamond_booklet.pdf.

A.2 Tunable spectral squeezers based on monolithically integrated diamond Raman resonators

Applied Physics Letters

Tunable spectral squeezers based on monolithically integrated diamond Raman resonators

Cite as: Appl. Phys. Lett. **120**, 151101 (2022); https://doi.org/10.1063/5.0088592
Submitted: 01 March 2022 • Accepted: 01 April 2022 • Published Online: 11 April 2022

E. Granados, G. Stoikos, D. T. Echarri, et al.

AIP Publishing

Applied Physics Letters ARTICLE scitation.org/journal/apl

Tunable spectral squeezers based on monolithically integrated diamond Raman resonators

Cite as: Appl. Phys. Lett. **120**, 151101 (2022); doi: 10.1063/5.0088592
Submitted: 1 March 2022 · Accepted: 1 April 2022 ·
Published Online: 11 April 2022

E. Granados,[1,a] G. Stoikos,[1,2] D. T. Echarri,[1,3] K. Chrysalidis,[1] V. N. Fedosseev,[1] C. Granados,[4] V. Leask,[1,5] B. A. Marsh,[1] and R. P. Mildren[6]

AFFILIATIONS

[1]CERN, 1217 Geneva, Switzerland
[2]National Technical University of Athens, Athens 106 82, Greece
[3]Universidad de Navarra, Tecnun, Manuel Lardizabal 13, 20018 Donostia, Spain
[4]Max-Born-Institut für Nichtlineare Optik und Kurzzeitspektroskopie, 12489 Berlin, Germany
[5]University of Strathclyde, 99 George Street, Glasgow G1 1RD, United Kingdom
[6]MQ Photonics Research Centre, Macquarie University, Sydney, NSW 2109, Australia

[a]Author to whom correspondence should be addressed: eduardo.granados@cern.ch

ABSTRACT

We report on the generation and tuning of single-frequency laser light in a monolithic Fabry–Pérot diamond Raman resonator operating in the visible spectral range. The device was capable of squeezing the linewidth of a broad multi-mode nanosecond pump laser ($\Delta\nu_p = 7.2 \pm 0.9$ GHz at $\lambda_p = 450$ nm) to a nearly Fourier-limited single axial mode Stokes pulse ($\Delta\nu_S = 114 \pm 20$ MHz at $\lambda_S = 479$ nm). The tuning was achieved by precise adjustment of the resonator temperature, with a measured frequency-temperature tuning slope of $\partial\nu_0/\partial T \approx -3$ GHz/K, and a temperature dependence of the first-order Raman phonon line of $\partial\nu_R/\partial T \approx +0.23$ GHz/K. The Stokes center frequency was tuned continuously for over 20 GHz (more than twice the free spectral range of the resonator), which, in combination with the broad Ti:Sapphire laser spectral tunability, enables the production of Fourier-limited pulses in the 400–500 nm spectral range. The Stokes center-frequency fluctuations were 52 MHz (RMS) when the temperature of the resonator was actively stabilized. Moreover, the conversion efficiency was up to 30%, yielding an overall power spectral density enhancement of >25× from pump to Stokes pulse.

Fourier-limited nanosecond pulses are important tools for applications exploiting light–atom interactions at high intensity. Beyond the requirement for a specific linewidth, precise tunability plays a crucial role for the spectroscopic study of narrow-band transitions,[1,2] atomic clocks and cooling,[3,4] or photonic quantum technology.[5–8] One key aspect hindering progress is in the complexity and scaling of individually and precisely tuned single-frequency laser sources at distinct wavelengths across the spectrum.

Beyond the problem of generating Fourier-limited pulses, realizing gigahertz-range frequency shifts with high accuracy while maintaining high efficiency and low loss—in particular, using a miniature and scalable device—is challenging because it requires efficient and controllable nonlinear processes. Typical integrated approaches used for this task are based on acousto-optics,[9,10] wave-mixing,[10,11] and electro-optics.[12] Acousto-optic modulators use phonon scattering to control the light center-frequency and can provide shifts in the kHz to few GHz range while being implemented on a silicon chip.[13] Wave-mixing can achieve efficient frequency conversion but requires stringent phase-matching conditions and is difficult to control due to a strong nonlinear dependence on optical power. The electro-optic effect typically produces parasitic side-bands, which requires additional spectral filtering elements to reduce spectral noise.

Alternatively, stimulated Raman scattering (SRS) and stimulated Brillouin scattering (SBS) can lead to the generation of highly coherent photons in a large variety of materials and at varied wavelengths,[14–16] some of which are suitable for integration on photonic chip

platforms.[17–19] Unlike typical inversion lasers, the emissions from stimulated-scattering lasers are not limited to specific wavelength ranges since no real energy levels are required; this provides unique advantages, such as access to unconventional wavelengths and compatibility with other integrated laser sources. In addition, the generation of the single longitudinal mode (SLM) laser light via SRS can directly provide an intrinsically stable single-frequency output without the parasitic effects of spatial hole burning mode competition,[20] although typically requires elaborated feedback loops to stabilize the cavity length.[21–24]

Recently, by embedding the laser resonator in the Raman media, it has been demonstrated that is possible to produce frequency stable output from a Fabry–Pérot (FP) diamond resonator without the need of external mechanical feedback loops to control the cavity length given that the temperature of the crystal is stabilized.[25] Moreover, these resonators can perform complex functions, such as "linewidth squeezing" when pumped by few GHz linewidth multi-mode lasers. Such mechanism, supported by phonon-resonant Raman interactions, directly enhances the power spectral density (PSD) of broadband nanosecond lasers by 50×. Furthermore, by operating in the so-called high Raman gain regime[14,16]—where the gain bandwidth is reduced to that of the pump laser, the constraints in the design of a resonator to support a single axial mode are further relaxed.

In this work, we build upon these recent demonstrations and present a tunable monolithic diamond Raman converter pumped by a frequency-doubled broadband nanosecond Ti:Sapphire laser. We demonstrate that the combination of FP diamond resonators with widely tunable multi-mode pump lasers not only is capable of producing a nearly Fourier-limited single-frequency pulses but also can be precisely tuned with an accuracy better than <52 MHz RMS over the entire spectral range of the pump laser tuning.

The monolithic Fabry–Pérot Raman medium was a synthetic diamond cuboid crystal with dimensions of $6 \times 2 \times 2\,\text{mm}^3$ [free spectral range (FSR) at 479 nm ≈ 9.5 GHz], plane-cut for beam propagation along the ⟨110⟩ axis, and end-faces re-polished with a parallelism better than 0.5 μm/mm. Thanks to the high Raman gain of diamond at 450 nm, the Fresnel reflectivity of un-coated surfaces ($R_1, R_2 \approx 18\%$) was sufficient to ensure highly efficient operation. A curved retro-reflector (M1) was used for circulating the pump pulse twice through the Raman medium, ensuring high conversion efficiency. The diamond crystal was placed on a copper mount inside a high precision oven (Covesion Ltd), with a temperature stability <10 mK.

The experiments were carried out using the tunable output provided by an intracavity frequency-doubled gain-switched Ti:Sapphire laser operating at 450 nm, similar to the one described in Refs. 14 and 26. Figure 1 shows a schematic diagram of the experimental setup. The Ti:Sapphire laser was pumped by the second harmonic of a Q-switched Nd:YAG laser (Innolas Nanio 532–20-V) producing up to 18 W of 532 nm light at a 10 kHz repetition rate, although only 8 W was used. The resulting pulse length of the Ti:Sapphire was 50 ns long, with a smooth temporal profile of asymmetric Gaussian shape. The second harmonic of the Ti:Sapphire laser was efficiently produced by intracavity frequency-doubling and exhibited a TEM_{00} Gaussian mode with an $M^2 < 1.3$. The second harmonic was then extracted from the Ti:Sapphire cavity by means of a dichroic mirror (DM1).

With this configuration, the system was capable of producing approximately 1.2 W of average power at 450 nm, with a continuously tunable output ranging from 350 to 470 nm. The output was focused into the diamond crystal by a 150 mm focal length lens, producing a waist of $57 \pm 5\,\mu$m in diameter and a resulting intensity of $0.1\,\text{GW/cm}^2$. The linewidth (FWHM) of the 450 nm light was measured with a wavelength meter LM-007 (CLUSTER LTD Moscow) and was 7.2 ± 0.9 GHz averaged over ∼1000 shots. In order to separate the pump from the Stokes output, a pair of dichroic mirrors (DM2 and DM3) were used, being possible to tune their angle to optimize the transmission of the pump and the reflection of the Stokes wavelength. The resulting tuning range depends both on the tunability of the pump laser as well as the spectral response of the dichroic mirrors in use.

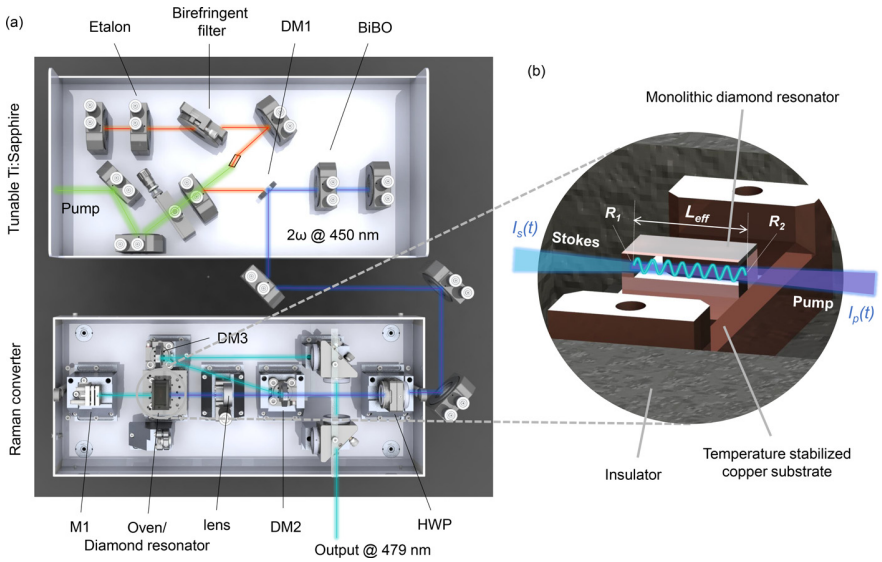

FIG. 1. Experimental setup. (a) A widely tunable frequency-doubled gain-switched Ti:Sapphire laser was used for pumping the Raman converter, its polarization control was performed using a half-wave plate (HWP) and a lens to focus it into the diamond resonator. (DM1) Dichroic mirror for separating fundamental and second harmonic beams, (DM2, DM3) Dichroic mirrors for separating pump at 450 nm and Stokes at 479 nm, (M1) curved retro-reflector. (b) Detail of the monolithic diamond resonator mounted on a temperature stabilized copper substrate within the insulated oven. R_1 and R_2 are the diamond surface reflectivites and L_{eff} the effective resonator length. $I_p(t)$ and $I_S(t)$ represent the intensity amplitude envelopes in the time domain of the pump and Stoke pulses, respectively.

The theory underlying the complex interplay between pump and Stokes spectral modes has been described in detail in Ref. 25. Here, we only discuss the most important modifications to adapt it to our experimental situation, in particular, regarding the effects of the temperature on the resonating Stokes mode frequency ν_0.

In contrast to previous works, our resulting Stokes frequency was precisely tunable (in the MHz range) using temperature while the pump laser modes were also tuned coarsely (in the multi-GHz domain) using intra-cavity spectral elements. The condition to obtain a spectral "funneling" effect described in Ref. 25, therefore, needs to be modified to

$$\nu_0(T) = \nu_{F(l)} - (\nu_R(T) \pm \Omega l). \quad (1)$$

Here, the term $(\nu_R(T) \pm \Omega l)$ accounts for a phonon that resonantly interacts with the fundamental field mode $\nu_{F(l)}$ and is within the Raman linewidth ($\Delta\nu_R > \Omega l \ \forall l$). Ω is the pump laser mode spacing. This situation corresponds to the sketch shown in Fig. 2(a) at $T = T_0$. The Raman shift $[\nu_R(T)]$ is temperature-dependent, and the resonating wavelength is determined by the mode closest to the peak of the temperature dependent Raman spectral gain as depicted in Fig. 2(b). Both effects and gain depletion dynamics interplay resulting in a specific Stokes center-frequency. Tuning adiabaticity is ensured by the continuous nature of the parameters involved in the process, with the exception of eventual mode-hops occurring at the edges of the resonator FSR. Meanwhile, the output linewidth is largely determined by the temporal characteristics of the fundamental field and the photon lifetime of the monolithic resonator, both of which are independent of temperature.

The sufficient conditions to ensure a single frequency operation of monolithic diamond resonators were studied in Ref. 25: First, the integrated resonator shall operate in the high Raman gain regime so that the Raman gain spectral width approaches the pump spectral width ($\Delta\nu_R \approx \Delta\nu_P$). Second, the free spectral range (FSR) of the diamond resonator needs to be larger than the pump laser linewidth (FSR $>\Delta\nu_P$). The high Raman gain regime condition is fulfilled here by adjusting the Raman gain to values similar to Ref. 25. In our experiments, the pump intensity was comparatively lower (0.1 GW/cm^2 compared to 0.3 GW/cm^2), but thanks to the favorable scaling of the Raman gain with shorter pump wavelengths,[27] the resulting gain was equivalent for both cases. The selected diamond had a FSR of 9.5 GHz compared to the 7.2 GHz linewidth of the pump laser ensuring single longitudinal mode operation.

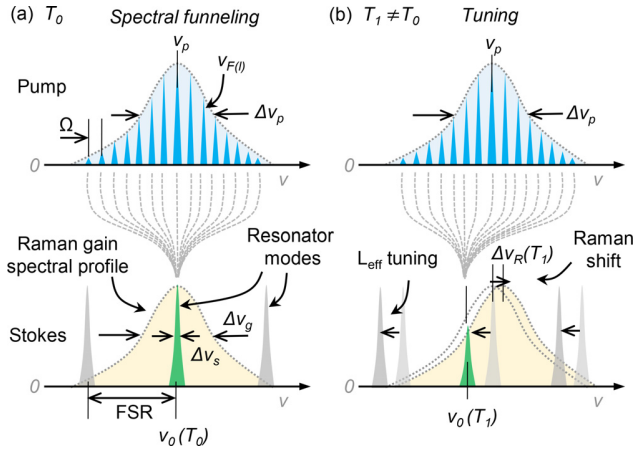

FIG. 2. Schematic depiction of (a) spectral funneling effect in monolithic diamond Raman lasers and (b) tuning of the funneling employing temperature.

The diamond converter produced a shifted Stokes output at 479 nm with <114 MHz linewidth at 30% power conversion efficiency (slope efficiency 58%), yielding a maximum peak power spectral density (PSD) enhancement of >25×, as shown in Fig. 3. The PSD normalization was carried out scaling the spectral curves so that their integrals correspond to the measured pulse energies.

The frequency stability results are shown in Fig. 4. Here, the diamond bulk was temperature stabilized with an accuracy <10 mK, and the resulting RMS fluctuation of the output Stokes center frequency was <52 MHz, measured over a period of two hours with a sampling rate of 15 Hz.

The measured peak-to-peak frequency fluctuation was <200 MHz. These fluctuations are assumed to be related to environmental factors, although a likely correlation between pump pulse energy and Stokes center frequency—due to the variable laser heat deposition in the crystal—also could render deviations in the resonator effective length. Likewise, the temperature gradient generated by the laser illumination of an area of only 160 μm^2 could in principle account for some discrepancy between the bulk temperature measurements and the actual diamond temperature at which the Raman interaction takes place. Such deviations, however, are assumed to be negligible due to the power stability of the pump laser (less than 1% RMS power fluctuations) and the high thermal conductivity of the diamond crystal, and so not affecting considerably the tuning slope.

In order to study the temperature dependency, we define "effective length" (L_{eff}) as the exact optical path length between

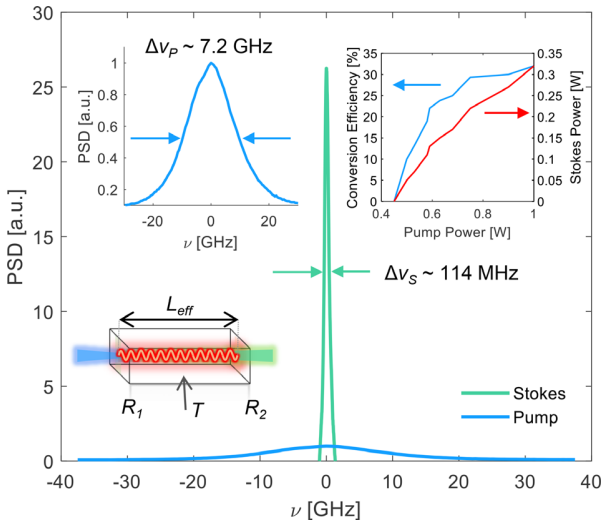

FIG. 3. Normalized power spectral density profile of the pump and Stokes pulses at maximum conversion efficiency. (Inset left) Pump pulse linewidth measurement. (Inset right) Slope and conversion efficiency. (Inset down) Sketch of the monolithic Fabry–Pérot diamond resonator, where R_1 and R_2 are the reflectivities of the parallel end-surfaces, T is the temperature setting, L_{eff} is the effective medium length at ν_0.

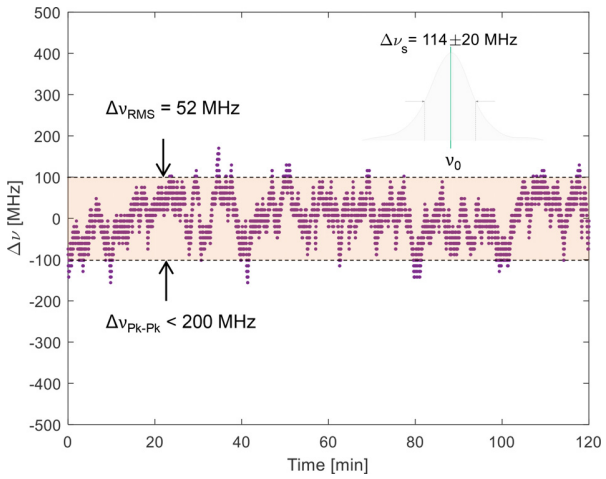

FIG. 4. Stokes frequency stability over a period of 2 h under constant temperature. (Inset) average measured Stokes linewidth during the same period.

resonator facets at a particular Stokes wavelength λ_S, which defines the resonating Stoke longitudinal modes frequencies. For Raman processes, the temperature dependence of the first-order Raman phonon line needs also to be taken into account to predict the output Stokes frequency accurately.

In general, it is possible to calculate separately the effects that produce a shift to the Stokes resonant frequency ν_0. The temperature affects the optical length of the resonator as well as the Raman shift. The effective length or optical path length at the wavelength λ_S and at temperature T_0 can be defined as

$$L_{\text{eff}}(T_0, \lambda_S) = L(T_0)n(T_0, \lambda_S). \tag{2}$$

The condition for resonance within the diamond resonator is

$$\lambda_S(T_0) = \frac{2}{q}L_{\text{eff}}(T_0, \lambda_S) = \frac{2}{q}L(T_0)n(T_0, \lambda_S), \tag{3}$$

where q is the mode number. Note that all wavelengths used in this mathematical formulation are in vacuum. For small shifts in temperature (ΔT), we can use a perturbation theory approach to estimate the resulting wavelength shift of the Stokes by

$$\lambda_S(T_0 + \Delta T) = \frac{2}{q}\left(L(T_0) + \frac{\partial L}{\partial T}\Delta T\right) \times \left(n(T_0, \lambda_S) + \frac{\partial n}{\partial T}\Delta T + \frac{\partial n}{\partial \lambda}\Delta\lambda_S\right). \tag{4}$$

Here, the term $\partial L/\partial T$ can be expressed in terms of the linear thermal expansion coefficient (α in the following) as $\partial L/\partial T = \alpha L(T_0)$. The shift in wavelength can be directly calculated by $\Delta\lambda_S = \lambda_S(T_0 + \Delta T) - \lambda_S(T_0)$. The terms $\partial n/\partial T$ and $\partial n/\partial\lambda$ correspond to the thermo-optic coefficient at T_0 and the chromatic dispersion at λ_S, respectively. Here, we assume that dispersion terms do not change for small temperature increments ΔT.

Reorganizing Eq. (4) and neglecting second order differential terms, we can obtain an approximate tuning slope of the center Stokes wavelength as a function of temperature. Changing variables from Stokes wavelength λ_S to resonating Stokes frequency ν_0, Eq. (4) becomes

$$\frac{\partial \nu_0}{\partial T} = -\frac{c}{\lambda_S}\frac{(1/n)(\partial n/\partial T) + \alpha}{1 - \lambda_S(1/n)(\partial n/\partial\lambda)}. \tag{5}$$

Note that, in general, the thermo-optic coefficient is a function of temperature and, therefore, the tuning slope will have a resulting temperature dependence; here, we take into account only the first-order term. It is apparent from Eq. (5) that in order to obtain an accurate and stable tune of the Stokes wavelength, materials exhibiting low thermo-optic coefficient and low thermal expansion coefficient α will present an advantage. Similarly, highly dispersive materials may further reduce requirements for temperature accuracy when high Stokes frequency stability is pursued.

Using Eq. (5), the expected values for the tuning slope in frequency ($\Delta\nu_0/\Delta T$) in the range from 300–400 K vary from −2.7 to −3.6 GHz/K as shown in Fig. 5(b). For this estimation, the thermo-optic coefficient was calculated using the model described in Ref. 28, whereas the dispersion was calculated using the two-factor Sellmeier equation for synthetic diamond found in Ref. 29 and the thermal expansion coefficient of $\alpha \sim 1.1 \times 10^{-6}$ K^{-1} found in Ref. 30.

The peak position ν_R and the linewidth of the first-order Raman mode of diamond at ∼1332 cm^{-1} are also a function of temperature. At a certain temperature T, the an-harmonic interactions can effectively change the unperturbed Raman frequency at 0 K. From a Klemens model, which assumes that the zone-center optical modes decay into two acoustical phonons of opposite momentum, the first order Raman line shifts by temperature as follows:[31]

$$\nu_R(T) = -B\left(\frac{2}{e^{\hbar\omega_0/2k_BT} - 1}\right), \tag{6}$$

where the unit-less scaling factor B depends on the details of the diamond dispersion curves.[31] A fit to the experimental data shown in Ref. 31 yields a value of $B = 1.3 \times 10^{12}$. Here, $\hbar\omega_0 = 1332.7$ cm^{-1} is the Raman shift at 0 K. It is worth noting that a negative $\nu_R(T)$ produces a higher Stokes frequency, and so the tuning slope of the Stokes center frequency will have a resulting positive sign. Differentiating Eq. (6), we obtain an analytical expression for the Raman shift tuning slope,

$$\frac{\partial \nu_R}{\partial T} = -B\frac{\hbar\omega_0 e^{(\hbar\omega_0/2k_BT)}}{k_BT^2(e^{(\hbar\omega_0/2k_BT)} - 1)^2}. \tag{7}$$

Using Eq. (7), the theoretical values for $(\partial\nu_R(T)/\partial T)$ in the range from 300–400 K induce a frequency shift in the center Stokes frequency from +0.2 GHz/K to +0.25 GHz/K as shown in Fig. 5(c).

From the calculated slope in Eq. (7), it is clear that for attaining a frequency stability below 100 MHz required for typical high-resolution spectroscopy or quantum applications, the temperature of the diamond resonator needs to be stabilized with an accuracy of at least <40 mK.

The tunability experimental tests were carried out by adjusting the temperature setting of the oven in increments of 10 mK, and the results are shown in Fig. 5(a). The average frequency-temperature tuning slope within a FSR of the resonator was approximately $\partial\nu_0/\partial T \approx -3$ GHz/K, whereas the temperature dependence of the first-order Raman phonon line was about $\partial\nu_R/\partial T \approx +0.23$ GHz/K. This agrees

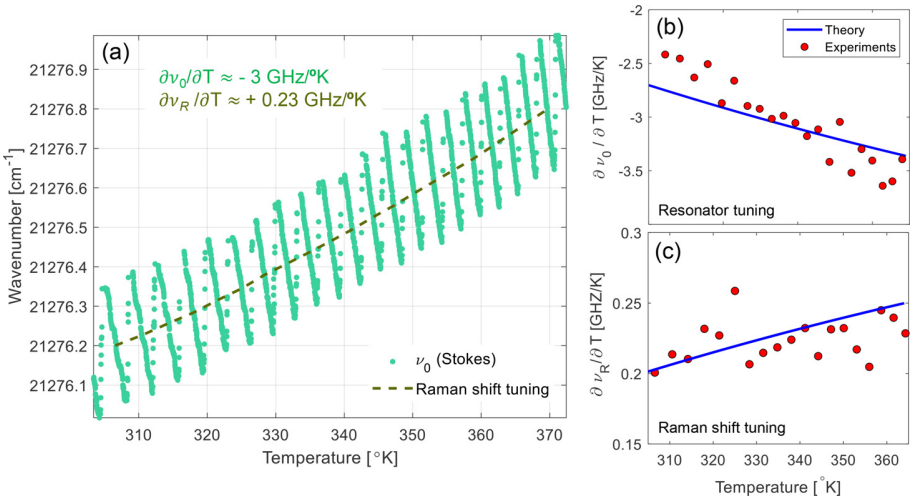

FIG. 5. (a) Stokes center frequency (ν_0) as a function of measured diamond surface temperature. Dashed line represents the tuning of the Raman shift as a function of temperature. Measured and calculated tuning slope due to (b) the variation of resonator effective length with temperature and (c) due to the Raman shift variation with temperature.

reasonably with previous calculations resulting from the Klemens model ($\approx +0.2$ to 0.25 GHz/K) and with the temperature dependent effective length calculations (-2.7 to -3.6 GHz/K) as shown in Figs. 5(b) and 5(c). It can be appreciated that the overall tuning slope is a nonlinear function of temperature due to the temperature dependency of the thermo-optic coefficient.[28] Interestingly, the range where the index of refraction is nonlinear is most severe for temperatures in the range from 200 to 400 K. Below 200 K, $(1/n)\partial n/\partial T$ is nearly zero, whereas for values above 400 K, it asymptotically tends to 7.1×10^{-6} K^{-1}. Within a small tuning ranges smaller than the FSR, the response was mostly linear, suggesting also that mode-pulling effects were essentially negligible.

The results portray also the possibility of selecting the optimal temperature range for ensuring that the Stokes frequency is at the center of the resonator FSR. This is thanks to the relatively small Raman shift temperature tuning compared to the thermo-optic and thermal expansion effects on the Stokes frequency. Such feature can be then exploited to facilitate pure single frequency operation without spectral side-modes, ensuring maximal output power and PSD simultaneously.

This work demonstrates that an inherently robust and simple monolithic diamond resonator can efficiently transform pulsed broad-band tunable laser radiation into a near-Fourier limited and continuously tunable output with significantly increased power spectral density. Our results show that tunable integrated FP diamond Raman resonators hold great promise for the on-chip generation of high intensity tunable narrow linewidth light across the optical spectrum, with broad ranging spectroscopy and quantum optics applications.

AUTHOR DECLARATIONS

Conflict of Interest

The authors have no conflicts to disclose.

DATA AVAILABILITY

The data that support the findings of this study are available from the corresponding author upon reasonable request.

REFERENCES

[1]P. Campbell, I. Moore, and M. Pearson, "Laser spectroscopy for nuclear structure physics," Prog. Part. Nucl. Phys. **86**, 127–180 (2016).
[2]K. Chrysalidis, S. Wilkins, R. Heinke, A. Koszorus, R. De Groote, V. Fedosseev, B. Marsh, S. Rothe, R. G. Ruiz, D. Studer, A. Vernon, and K. Wendt, "First demonstration of Doppler-free 2-photon in-source laser spectroscopy at the ISOLDE-RILIS," Nucl. Instrum. Methods Phys. Res., Sect. B **463**, 476–481 (2020).
[3]J. Hu, A. Urvoy, Z. Vendeiro, V. Crépel, W. Chen, and V. Vuletić, "Creation of a Bose-condensed gas of ^{87}Rb by laser cooling," Science **358**, 1078–1080 (2017).
[4]C. J. Baker, W. Bertsche, A. Capra, C. Carruth, C. L. Cesar, M. Charlton, A. Christensen, R. Collister, A. C. Mathad, S. Eriksson, A. Evans, N. Evetts, J. Fajans, T. Friesen, M. C. Fujiwara, D. R. Gill, P. Grandemange, P. Granum, J. S. Hangst, W. N. Hardy, M. E. Hayden, D. Hodgkinson, E. Hunter, C. A. Isaac, M. A. Johnson, J. M. Jones, S. A. Jones, S. Jonsell, A. Khramov, P. Knapp, L. Kurchaninov, N. Madsen, D. Maxwell, J. T. K. McKenna, S. Menary, J. M. Michan, T. Momose, P. S. Mullan, J. J. Munich, K. Olchanski, A. Olin, J. Peszka, A. Powell, P. Pusa, C. Ø. Rasmussen, F. Robicheaux, R. L. Sacramento, M. Sameed, E. Sarid, D. M. Silveira, D. M. Starko, C. So, G. Stutter, T. D. Tharp, A. Thibeault, R. I. Thompson, D. P. van der Werf, and J. S. Wurtele, "Laser cooling of antihydrogen atoms," Nature **592**, 35–42 (2021).
[5]M. Kues, C. Reimer, P. Roztocki, L. R. Cortés, S. Sciara, B. Wetzel, Y. Zhang, A. Cino, S. T. Chu, B. E. Little, D. J. Moss, L. Caspani, J. Azaña, and R. Morandotti, "On-chip generation of high-dimensional entangled quantum states and their coherent control," Nature **546**, 622–626 (2017).
[6]H.-H. Lu, J. M. Lukens, N. A. Peters, O. D. Odele, D. E. Leaird, A. M. Weiner, and P. Lougovski, "Electro-optic frequency beam splitters and tritters for high-fidelity photonic quantum information processing," Phys. Rev. Lett. **120**, 030502 (2018).
[7]K. K. Mehta, C. Zhang, M. Malinowski, T.-L. Nguyen, M. Stadler, and J. P. Home, "Integrated optical multi-ion quantum logic," Nature **586**, 533–537 (2020).
[8]J. M. Lukens and P. Lougovski, "Frequency-encoded photonic qubits for scalable quantum information processing," Optica **4**, 8–16 (2017).
[9]E. A. Kittlaus, N. T. Otterstrom, P. Kharel, S. Gertler, and P. T. Rakich, "Non-reciprocal interband Brillouin modulation," Nat. Photonics **12**, 613–619 (2018).
[10]D. B. Sohn, S. Kim, and G. Bahl, "Time-reversal symmetry breaking with acoustic pumping of nanophotonic circuits," Nat. Photonics **12**, 91–97 (2018).
[11]C. Joshi, A. Farsi, A. Dutt, B. Y. Kim, X. Ji, Y. Zhao, A. M. Bishop, M. Lipson, and A. L. Gaeta, "Frequency-domain quantum interference with correlated photons from an integrated microresonator," Phys. Rev. Lett. **124**, 143601 (2020).

[12]A. A. Savchenkov, W. Liang, A. B. Matsko, V. S. Ilchenko, D. Seidel, and L. Maleki, "Tunable optical single-sideband modulator with complete sideband suppression," Opt. Lett. **34**, 1300–1302 (2009).
[13]E. A. Kittlaus, W. M. Jones, P. T. Rakich, N. T. Otterstrom, R. E. Muller, and M. Rais-Zadeh, "Electrically driven acousto-optics and broadband non-reciprocity in silicon photonics," Nat. Photonics **15**, 43–52 (2021).
[14]K. Chrysalidis, V. N. Fedosseev, B. A. Marsh, R. P. Mildren, D. J. Spence, K. D. A. Wendt, S. G. Wilkins, and E. Granados, "Continuously tunable diamond Raman laser for resonance laser ionization," Opt. Lett. **44**, 3924–3927 (2019).
[15]E. Granados, D. J. Spence, and R. P. Mildren, "Deep ultraviolet diamond Raman laser," Opt. Express **19**, 10857–10863 (2011).
[16]D. T. Echarri, K. Chrysalidis, V. N. Fedosseev, B. A. Marsh, R. P. Mildren, S. M. Olaizola, D. J. Spence, S. G. Wilkins, and E. Granados, "Broadly tunable linewidth-invariant Raman Stokes comb for selective resonance photo-ionization," Opt. Express **28**, 8589–8600 (2020).
[17]Z. Bai, R. J. Williams, O. Kitzler, S. Sarang, D. J. Spence, Y. Wang, Z. Lu, and R. P. Mildren, "Diamond Brillouin laser in the visible," APL Photonics **5**, 031301 (2020).
[18]B. J. Eggleton, C. G. Poulton, P. T. Rakich, M. J. Steel, and G. Bahl, "Brillouin integrated photonics," Nat. Photonics **13**, 664–677 (2019).
[19]N. Chauhan, A. Isichenko, K. Liu, J. Wang, Q. Zhao, R. O. Behunin, P. T. Rakich, A. M. Jayich, C. Fertig, C. W. Hoyt, and D. J. Blumenthal, "Visible light photonic integrated Brillouin laser," Nat. Commun. **12**, 4685 (2021).
[20]O. Lux, S. Sarang, O. Kitzler, D. J. Spence, and R. P. Mildren, "Intrinsically stable high-power single longitudinal mode laser using spatial hole burning free gain," Optica **3**, 876–881 (2016).
[21]X. Yang, Z. Bai, D. Chen, W. Chen, Y. Feng, and R. P. Mildren, "Widely-tunable single-frequency diamond Raman laser," Opt. Express **29**, 29449–29457 (2021).
[22]S. Sarang, O. Kitzler, O. Lux, Z. Bai, R. J. Williams, D. J. Spence, and R. P. Mildren, "Single-longitudinal-mode diamond laser stabilization using polarization-dependent Raman gain," OSA Continuum **2**, 1028–1038 (2019).
[23]X. Yang, O. Kitzler, D. J. Spence, R. J. Williams, Z. Bai, S. Sarang, L. Zhang, Y. Feng, and R. P. Mildren, "Single-frequency 620 nm diamond laser at high power, stabilized via harmonic self-suppression and spatial-hole-burning-free gain," Opt. Lett. **44**, 839–842 (2019).
[24]O. Lux, S. Sarang, R. J. Williams, A. McKay, and R. P. Mildren, "Single longitudinal mode diamond raman laser in the eye-safe spectral region for water vapor detection," Opt. Express **24**, 27812–27820 (2016).
[25]E. Granados, C. Granados, R. Ahmed, K. Chrysalidis, V. N. Fedosseev, B. A. Marsh, S. G. Wilkins, R. P. Mildren, and D. J. Spence, "Spectral synthesis of multimode lasers to the Fourier limit in integrated Fabry–Perot diamond resonators," Optica **9**, 317–324 (2022).
[26]S. Rothe, B. A. Marsh, C. Mattolat, V. N. Fedosseev, and K. Wendt, "A complementary laser system for ISOLDE RILIS," J. Phys.: Conf. Ser. **312**, 052020 (2011).
[27]V. G. Savitski, S. Reilly, and A. J. Kemp, "Steady-state Raman gain in diamond as a function of pump wavelength," IEEE J. Quantum Electron. **49**, 218–223 (2013).
[28]T. Ruf, M. Cardona, C. S. J. Pickles, and R. Sussmann, "Temperature dependence of the refractive index of diamond up to 925K," Phys. Rev. B **62**, 16578–16581 (2000).
[29]G. Turri, S. Webster, Y. Chen, B. Wickham, A. Bennett, and M. Bass, "Index of refraction from the near-ultraviolet to the near-infrared from a single crystal microwave-assisted CVD diamond," Opt. Mater. Express **7**, 855–859 (2017).
[30]P. Jacobson and S. Stoupin, "Thermal expansion coefficient of diamond in a wide temperature range," Diamond Relat. Mater. **97**, 107469 (2019).
[31]M. S. Liu, L. A. Bursill, S. Prawer, and R. Beserman, "Temperature dependence of the first-order Raman phonon line of diamond," Phys. Rev. B **61**, 3391–3395 (2000).

A.3 Spectral purification of single-frequency Stokes pulses in doubly resonant integrated diamond resonators

Optics Letters

Spectral purification of single-frequency Stokes pulses in doubly resonant integrated diamond resonators

EDUARDO GRANADOS[1,*] AND GEORGIOS STOIKOS[1,2]

[1]CERN, 1217 Geneva, Switzerland
[2]School of Applied Mathematics and Physical Sciences, National Technical University of Athens, Greece
*Corresponding author: eduardo.granados@cern.ch

Received 26 May 2022; revised 6 July 2022; accepted 15 July 2022; posted 19 July 2022; published 2 August 2022

Pulsed spectrally pure light is required for applications in high-resolution spectroscopy, optical coherent communications, and quantum technologies. In this work, we report on the efficient generation of high peak power, single-frequency, and tunable nanosecond pulses utilizing stimulated scattering, with an increased spectral brightness by exploiting double resonances in an integrated diamond Raman resonator. The device is based on a miniature monolithic Fabry–Perot design pumped by a milliwatt-class average power Q-switched single-frequency pulsed laser at 532 nm. Our device was capable of enhancing the peak spectral brightness by greater than three times compared with conventional singly resonant diamond Raman lasers by tuning the effective resonator length at pump and Stokes wavelengths simultaneously. Our results facilitate the integration of pulsed and power scalable single frequency sources into hybrid photonic integrated platforms with a broad range of applications.

https://doi.org/10.1364/OL.464816

Introduction. The production of highly coherent radiation using integrated photonic sources at arbitrary wavelengths is a continuous endeavor. Miniaturized and microchip lasers have become the leading platforms in optical sensing and communication systems due to their small footprint, reliability, high stability, and beam quality. Several wavelength regimes, however, are not directly accessible with such lasers and require wavelength conversion using non-linear processes [1]. The ability to produce spectrally pure tunable light in integrated platforms remains a major paradigm, holding the promise to solve the scalability challenges of quantum technologies based on photons and ion excitations [2,3].

A potential solution relies in employing integrated stimulated Raman scattering (SRS) to shift the wavelength of available compact pump lasers [4]. Here the non-linear optical interaction is mediated via phonons, so that the pump photons are usually redshifted by the fixed phonon frequency. The frequency shift and the efficiency of the conversion process depend on the selection of Raman medium and in particular on the phonons involved. This technique has been widely used to produce nearly any laser wavelength given a suitable pump laser is available and the Raman media transparency allows it [5].

One key advantage of SRS is that the gain is mediated by propagating pump photons rather than via energy storage in localized inverted ions, so there can be no local regions of unextracted pump energy and therefore no spatial hole burning [6]. Diamond is a particularly good candidate thanks to its outstanding optical and thermal properties: large Raman gain (>40 cm/GW at 532 nm), large Raman shift (1332 cm^{-1}), and low thermal expansion coefficient ($\alpha \sim 1.1 \times 10^{-6}\ K^{-1}$) [7–9]. This large Raman shift enables wavelengths to be accessed for which no ideal solution exists in terms of cost, convenience, and output power [10,11]. Other advantages of diamond in this context are the wide bandgap of diamond, which prevents free carrier absorption minimizing optical losses in the visible and the ultraviolet wavelength regimes [12], and diamond's high thermal conductivity, which facilitates efficient heat management [13].

Diamond Raman lasers have also enabled the generation of single-frequency light at exotic wavelengths, e.g., the entire visible spectral range—where no common single mode laser diodes are available—and the infrared (IR) [6,14–16]. However, such lasers typically require elaborate feedback loops to stabilize the cavity length. Recently, by integrating the laser resonator within the Raman media, it was demonstrated that it is possible to produce frequency stable output from a Fabry–Perot diamond resonator without the need of external mechanical feedback loops to control the cavity length given that the temperature of the crystal is stable enough, opening the way to simple, integrated, and tunable single-frequency Raman lasers [17,18].

Advances in diamond nano-fabrication enabled the demonstration of integrated diamond Raman lasers using ring resonators at IR [19] and near-visible [20] wavelengths. The combination of high-quality factors with small mode volumes allowed for a significant reduction on the continuous wave (CW) lasing threshold in such schemes. Doubly resonant configurations have been used in the CW regime for low-threshold diamond Raman lasers using open microcavities, constructed by embedding a high-quality diamond membrane within the reflectors [21].

In this Letter, through a similar approach, we resonantly recirculate the pump beam in an integrated Fabry–Perot resonator

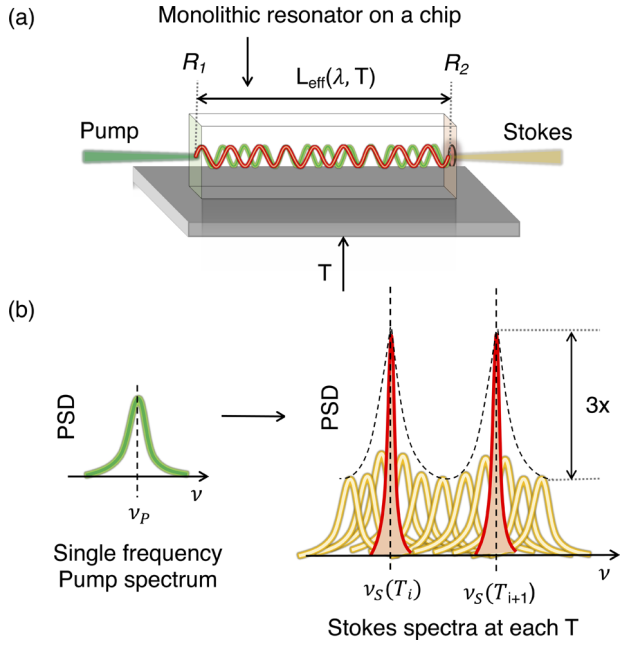

Fig. 1. (a) Schematic of a tunable monolithic Fabry–Perot diamond resonator, including a temperature stabilization, end-surface reflectivities R_1 and R_2, and effective length L_{eff} at wavelength λ and temperature T. (b) Representation of the power spectral density (PSD) enhancement of the Stokes fields at specific temperatures T_i by a factor of three.

in the pulsed regime. We demonstrate that using this technique it is possible to produce near-Fourier limited nanosecond pulses with very modest pump pulse energy requirements in the microjoule range (and corresponding milliwatt average powers in our setup), while reducing the Stokes pulse linewidth by a factor of greater than three when the doubly resonant condition is fulfilled.

Theory. The setup considered in this study is depicted in Fig. 1(a). Here R_1 and R_2 are the reflectivities at each diamond end, and L_{eff} the optical path length at wavelength λ and temperature T. For conventional resonators, the resonant wavelength changes linearly with the mirror separation. However, the diamond medium significantly alters the otherwise linear mode spectral structure.

The production of single frequency resonant Stokes fields depends on many factors, but most importantly on the characteristics of the pump laser intensity, wavelength, linewidth, the resonator optical length, and the temporal envelope of the pump and Stokes fields. It can be shown that for resonators with relatively low-quality factor (Q), such interplay between pump and Stokes fields produces nearly identical pulse envelopes in the temporal domain. This is because the temporal variations of nanosecond pulses are much longer than the resonator length. The calculation of the resulting Stokes linewidth can be further performed following the modeling approach described in Ref. [17].

The frequency stabilization of the resonator was carried out by adjusting the temperature, which simultaneously influenced its index of refraction, size, and the Raman shift. The resulting Stokes frequency and its tuning slope always fulfills the condition for resonance since it originates within the resonator and can be calculated following Refs. [18,22].

The resonant condition for the pump field follows a slightly different trend, since its center wavelength is readily stabilized externally. Thus, we only need to calculate the discreet set of temperatures T_i at which the resonant condition is fulfilled for the pump field. Mathematically these two conditions are expressed as

$$\begin{cases} \nu_S(T) = q_S \frac{c}{2L_{\text{eff}}(T,\nu_S)}, \\ \nu_F = q_{F_i} \frac{c}{2L_{\text{eff}}(T_i,\nu_F)}. \end{cases} \tag{1}$$

Here q_S is the longitudinal Stokes mode number, c is the speed of light in vacuum, and $L_{\text{eff}}(T,\nu)$ is the effective length of the resonator at either the Stokes or pump resonating frequency ν and at temperature T. Here L_{eff} can be calculated as $L_{\text{eff}}(T,\nu) = L(T)n(\lambda,T)$, where $n(\lambda,T)$ is the wavelength-temperature dependent index of refraction [22], and $L(T)$ the resonator physical length at temperature T. We numerically find values of the pump mode number q_{F_i} and T_i that fulfill the system of Eq. (1), corresponding to the case depicted in Fig. 1(b), where the PSD is enhanced due to double resonances.

We can also calculate the resonating Stokes frequency $\nu_S(T_i)$ at those selected temperatures T_i. Following [18], it can be shown that the temperature-frequency dependency for the Stokes fields follow the relation

$$\left.\frac{\partial \nu_S}{\partial T}\right|_{T_0} = -c\frac{\frac{1}{n}\frac{\partial n_T}{\partial T} + \alpha(T)}{\lambda_S\left(1 - \frac{\lambda_S}{n}\frac{\partial n_\lambda}{\partial \lambda}\right)}, \tag{2}$$

where $\alpha(T)$ is the temperature-dependent thermal expansion coefficient of chemical vapor deposition (CVD) diamond, and $(1/n)\partial n_T/\partial T$ the temperature-dependent thermo-optic coefficient. In fact, the non-linear or temperature-dependent thermo-optic coefficient plays an important role in the tuning slope of the Stokes field by producing a variable tuning slope of the Stokes field with temperature.

Results for a resonator equivalent to the one used in the experiments are shown in Fig. 2. The doubly resonant condition occurs at the intersections of the Stokes tuning curve, calculated using Eqs. (1) and (2), and the temperatures T_i. Here the lasing tuning extent of the Stokes pulse is limited by the free spectral range (FSR) of the diamond resonator, which at the limits produces a mode-hopping effect when jumping from mode q_S to $q_S + 1$, and is defined by the temperature-dependent Raman shift. Note

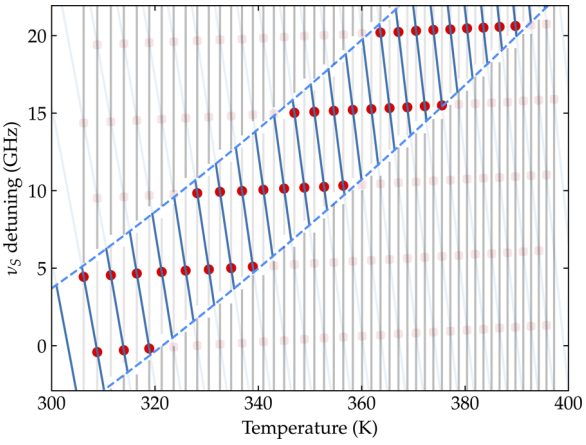

Fig. 2. Predicted Stokes frequencies at which double resonances occur. In blue the center frequency of the Stokes field as a function of temperature; in gray lines the resonant condition for the pump field at T_i. The crossing between these curves, depicted as red circles, are solutions for the doubly resonant condition in Eq. (1).

that the resonating frequencies depend directly on the physical length of the diamond L, and thanks to the imperfect parallelism between the resonator surfaces, it was easily tunable by displacing the resonator laterally.

When the laser operates in this regime, the pump experiences an intracavity field enhancement effect due to the coherent superposition of the recirculating fields. This enhancement factor A depends on R_1 and R_2 and can be calculated following Ref. [23]. For example, an uncoated diamond resonator such as the one used in our experiments ($R_1 = R_2 \approx 17\%$), results in a maximum enhancement factor of $A_{\max} = 1.45$, whereas out of resonance A can be as low as 0.73. This enhancement—even for very low Q resonators—accounts already for a factor of ~ 2 in the net Raman gain (which reduces the lasing threshold), and a spectral filtering of the pump pulse that further reduces its noise. Note that even though the lasing threshold was reduced, we observed no variation of the output power between doubly or singly resonant cases, due to the production of cascaded Stokes orders under doubly resonant conditions.

Experiments. The diamond that constitutes the Fabry–Perot resonator was 7 mm in length (Element Six Ltd.) and repolished to achieve an end-face parallelism better than 0.5 μm/mm. The resonator length produced an FSR of 8 GHz at 573 nm. The resonator was directly pumped at 532 nm by means of a 20 cm focal length lens, that produced a Stokes pulse at 573 nm. The experiments were performed with an uncoated diamond resonator which was temperature stabilized with a precision <0.01 K and within the range from 310–370 K.

The pump laser was an ultra-compact Cobolt Tor xs 532nm, producing a frequency stabilized Fourier-limited output with a pulse duration of around 8 ns. The pulses had an energy of 50 μJ at a repetition rate of 100 Hz. The laser beam was then focused onto the resonator with a waist size of 25 μm ($1/e^2$). The Rayleigh length of the beam was roughly matched to the resonator length. Under this condition, the output Stokes pulse energy was 10 ± 2 μJ, which corresponds to a conversion efficiency of nearly 19%, and did not depend on the resonator temperature.

To determine the spectral characteristics of the pump and Stokes pulses, we used a spectrum analyzer (Lambdameter LM-007, Cluster Ltd., Moscow) based on a set of four Fizeau interferometers allowing us to resolve linewidths below 100 MHz. A tuning slope of around −2.4 GHz/K was observed when adjusting the oven temperature, as can be seen in Fig. 3. The pump laser linewidth was essentially Fourier-limited and yielded a value of $\Delta\nu_F = 120 \pm 20$ MHz, and is Lorentzian in line shape. The results for the Stokes pulses are also depicted in Fig. 3, where we included the linewidth readout as a color gradient, and the obtained peak PSD for on resonance and off resonance in the inset plot. The resemblance between the theory depicted in Fig. 2, and the experimental results in Fig. 3, suggests that the effect behind the observed linewidth squeezing is related to the fulfillment of the doubly resonant condition in Eq. (1). The minimum Stokes spectral width measured was 130 MHz, whereas for non-resonant conditions the linewidth was >500 MHz. In all cases a single-mode Stokes output was produced.

The results concerning the linewidth of the Stokes fields as a function of Stokes detuning are depicted in Fig. 4(a). These are essentially the same data set as the one used for producing Fig. 3, but with a different point of view. Here we show instead the double resonance spectral extent as a function of Stokes frequency detuning. For small temperature increments,

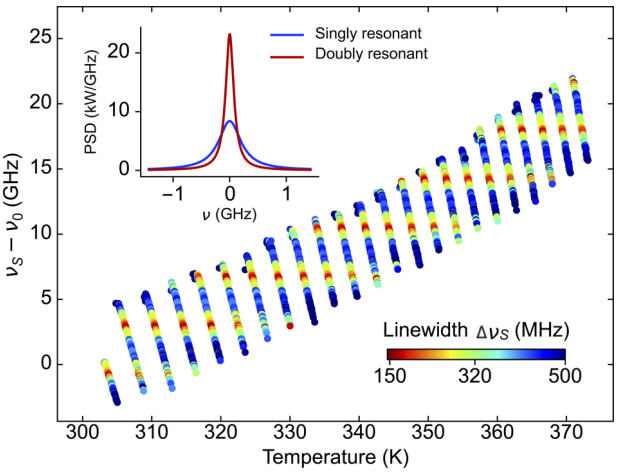

Fig. 3. Measured Stokes center frequency ν_S (circles) and linewidth (color) as a function of diamond resonator temperature. Inset: Stokes PSD for doubly resonant (red) and singly resonant (blue).

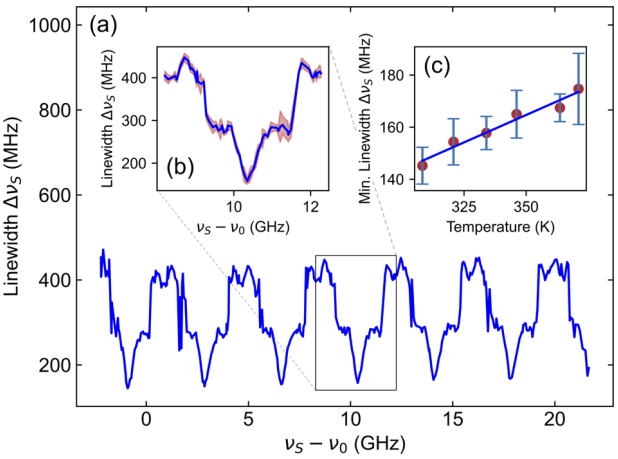

Fig. 4. (a) Linewidth of the Stokes fields as a function of Stokes center frequency detuning ν_S at a range of temperature between 310–370 K. (b) Average and deviation of the linewidth measured for a particular detuning range. (c) Variation of the average minimum measured linewidth (and deviation) as a function of temperature.

the relationship between the detuned Stokes frequency and the resonator temperature is quasi-linear. Another interesting feature is the appearance of second-order-like resonances. These peaks are associated with higher-order resonator modes, and can be observed in all the doubly resonant ranges as side-modes with a linewidth relative minima (approximately 250 MHz) in Fig. 4(b).

The observed periodicity in the double resonances as a function of Stokes frequency detuning matches well the results obtained from the theoretical model. This periodicity is variable with temperature and spectral range, and for the ranges studied here corresponded to approximately 3.7 ± 0.1 GHz. In addition, it is observed that the minimum linewidth attainable is a weak linear function of temperature, as shown in Fig. 4(c). This can be also consequence of the temperature dependency of the Raman gain, which in this range linearly decreases with temperature. Overall, the region for double-resonant enhancement

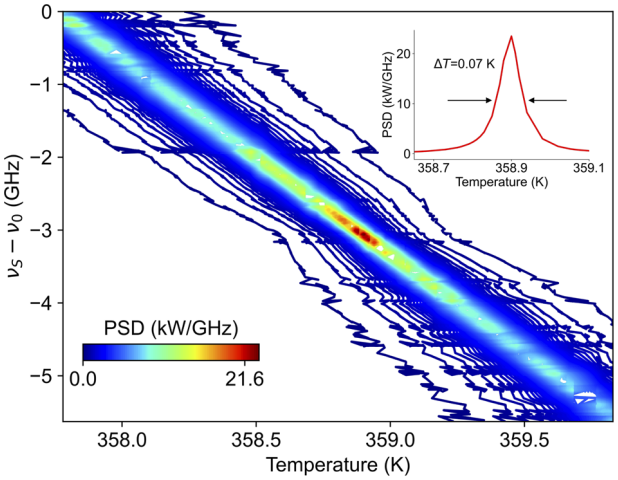

Fig. 5. Peak PSD as a function of resonator temperature and Stokes center frequency ν_S detuning. Inset: line-out of the PSD as a function of temperature variation.

occurred for detunings of approximately 0.5 GHz [full width at half maximum (FWHM)], corresponding to a temperature range of less than 0.2 K.

Figure 5 shows the PSD combining the measurements of the Stokes linewidth, center frequency, and output power. This approximation was performed assuming Lorentzian spectral profiles for the Stokes fields, in accordance to what was measured in Ref. [17]. A maximum PSD of 21.6 kW/GHz was recorded, compared with a minimum of 6.3 kW/GHz for singly resonant conditions. The doubly resonant condition requires a temperature stability better than 0.07 K, as can be seen inset of Fig. 5.

Conclusions. In conclusion, we demonstrate a power scalable, widely tunable, single-frequency system featuring doubly resonant-driven spectral brightness enhancement. Temperature tuning provides a convenient way to establish a double resonance condition in which both pump and Stokes fields are resonant within the resonator, while the imperfect parallelism of the diamond medium enables us to tune the doubly resonant condition over a wide range. The results, together with the low-quality factors of the resonator in the visible wavelength range, suggest that our technique can be further improved using higher Q resonators, potentially enhancing the PSD further.

These advancements pave the way to a universal, integrated, frequency-shifter with enhanced spectral brightness. Finally, we note that due to the generality of our findings, other wide-bandgap Raman laser materials such as silicon can use the same strategies explained here. Our results show that tunable integrated Fabry–Perot diamond Raman resonators hold great promise for the on-chip generation of high-intensity tunable narrow linewidth light across the optical spectrum, with broad ranging spectroscopy and quantum technology applications.

Funding. CERN (Knowledge Transfer - Singular Light).

Disclosures. The authors declare no conflicts of interest.

Data availability. Data underlying the results presented in this paper are not publicly available at this time but may be obtained from the authors upon reasonable request.

REFERENCES

1. A. Siddharth, T. Wunderer, G. Lihachev, A. S. Voloshin, C. Haller, R. N. Wang, M. Teepe, Z. Yang, J. Liu, J. Riemensberger, N. Grandjean, N. Johnson, and T. J. Kippenberg, APL Photonics **7**, 046108 (2022).
2. W. Loh, J. Stuart, D. Reens, C. D. Bruzewicz, D. Braje, J. Chiaverini, P. W. Juodawlkis, J. M. Sage, and R. McConnell, Nature **588**, 244 (2020).
3. N. Chauhan, A. Isichenko, K. Liu, J. Wang, Q. Zhao, R. O. Behunin, P. T. Rakich, A. M. Jayich, C. Fertig, C. W. Hoyt, and D. J. Blumenthal, Nat. Commun. **12**, 4685 (2021).
4. M. A. Ferrara and L. Sirleto, Micromachines **11**, 330 (2020).
5. H. Pask, P. Dekker, R. Mildren, D. Spence, and J. Piper, Prog. Quantum Electron. **32**, 121 (2008).
6. O. Lux, S. Sarang, R. J. Williams, A. McKay, and R. P. Mildren, Opt. Express **24**, 27812 (2016).
7. V. G. Savitski, S. Reilly, and A. J. Kemp, IEEE J. Quantum Electron. **49**, 218 (2013).
8. E. Granados, D. J. Spence, and R. P. Mildren, Opt. Express **19**, 10857 (2011).
9. P. Jacobson and S. Stoupin, Diamond Relat. Mater. **97**, 107469 (2019).
10. K. Chrysalidis, V. N. Fedosseev, B. A. Marsh, R. P. Mildren, D. J. Spence, K. D. A. Wendt, S. G. Wilkins, and E. Granados, Opt. Lett. **44**, 3924 (2019).
11. D. T. Echarri, K. Chrysalidis, V. N. Fedosseev, B. A. Marsh, R. P. Mildren, S. M. Olaizola, D. J. Spence, S. G. Wilkins, and E. Granados, Opt. Express **28**, 8589 (2020).
12. B. Sotillo, V. Bharadwaj, J. P. Hadden, M. Sakakura, A. Chiappini, T. T. Fernandez, S. Longhi, O. Jedrkiewicz, Y. Shimotsuma, L. Criante, R. Osellame, G. Galzerano, M. Ferrari, K. Miura, R. Ramponi, P. E. Barclay, and S. M. Eaton, Sci. Rep. **6**, 35566 (2016).
13. S. Antipov, R. J. Williams, A. Sabella, O. Kitzler, A. Berhane, D. J. Spence, and R. P. Mildren, Opt. Express **28**, 15232 (2020).
14. X. Yang, Z. Bai, D. Chen, W. Chen, Y. Feng, and R. P. Mildren, Opt. Express **29**, 29449 (2021).
15. S. Sarang, O. Kitzler, O. Lux, Z. Bai, R. J. Williams, D. J. Spence, and R. P. Mildren, OSA Continuum **2**, 1028 (2019).
16. H. Ma, X. Wei, H. Zhao, M. Zhang, H. Zhou, S. Zhu, H. Yin, Z. Li, Z. Chen, Y. Shen, N. Zong, S. Zhang, and S. Dai, Opt. Lett. **47**, 2210 (2022).
17. E. Granados, C. Granados, R. Ahmed, K. Chrysalidis, V. N. Fedosseev, B. A. Marsh, S. G. Wilkins, R. P. Mildren, and D. J. Spence, Optica **9**, 317 (2022).
18. E. Granados, G. Stoikos, D. T. Echarri, K. Chrysalidis, V. N. Fedosseev, C. Granados, V. Leask, B. A. Marsh, and R. P. Mildren, Appl. Phys. Lett. **120**, 151101 (2022).
19. P. Latawiec, V. Venkataraman, M. J. Burek, B. J. M. Hausmann, I. Bulu, and M. Lončar, Optica **2**, 924 (2015).
20. P. Latawiec, V. Venkataraman, A. Shams-Ansari, M. Markham, and M. Lončar, Opt. Lett. **43**, 318 (2018).
21. S. Flågan, D. Riedel, A. Javadi, T. Jakubczyk, P. Maletinsky, and R. J. Warburton, J. Appl. Phys. **131**, 113102 (2022).
22. G. Stoikos and E. Granados, "The influence of phonon harmonicity on spectrally pure resonant Stokes fields," arXiv:2204.11255 (2022).
23. N. Ismail, C. C. Kores, D. Geskus, and M. Pollnau, Opt. Express **24**, 16366 (2016).

Appendix B

Stokes center frequency change with temperature

Eq. 4.2 was found by:

$$\begin{cases} \nu_S = \frac{c}{\lambda_S} \\ L_{eff} = n \cdot L \\ q \cdot \frac{\lambda_S}{2} = L_e ff \end{cases} \tag{B.1}$$

where c is the speed of light, ν_S the Stokes frequency and λ_S the Stokes wavelength. By following perturbation theory and ignoring second order terms, we can find $\frac{\partial \nu_S}{\partial T}$ as:

$$\lambda_S(T_0 + \Delta T) = \frac{2}{q}\left(L(T_0) + \frac{\partial L}{\partial T}\Delta T\right) \cdot \left(n(T_0, \lambda_S) + \frac{\partial n}{\partial T}\Delta T + \frac{\partial n}{\partial \lambda}\Delta\lambda_S\right)$$

$$\lambda_S + \Delta\lambda_S = \frac{2}{q}\left(\cancel{L \cdot n}^{\lambda_S} + L \cdot \frac{\partial n}{\partial T}\Delta T + L \cdot \frac{\partial n}{\partial \lambda}\Delta\lambda_S + \right.$$

$$\left. + \frac{\partial L}{\partial T}\Delta T \cdot n + \cancel{\frac{\partial L}{\partial T}\Delta T \cdot \frac{\partial n}{\partial T}\Delta T}^{0} + \cancel{\frac{\partial L}{\partial T}\Delta T \cdot \frac{\partial n}{\partial \lambda}\Delta\lambda_S}^{0}\right)$$

$$\Delta\lambda_S = \frac{2}{q}\left(L \cdot \frac{\partial n}{\partial T}\Delta T + L \cdot \frac{\partial n}{\partial \lambda}\Delta\lambda_S + \frac{\partial L}{\partial T}\Delta T \cdot n\right)$$

$$\left(1 - \cancel{\frac{2}{q}L \cdot \frac{\partial n}{\partial \lambda}}^{\lambda_S/n}\right)\Delta\lambda_S = \frac{2}{q}\left(L \cdot \frac{\partial n}{\partial T} + \cancel{\frac{\partial L}{\partial T}}^{\alpha L} \cdot n\right)\Delta T$$

$$\frac{\Delta\lambda_S}{\Delta T} = \frac{\cancel{\frac{2}{q}L \cdot \frac{\partial n}{\partial T}}^{\lambda_S/n} + \alpha\cancel{\frac{2}{q}L \cdot n}^{\lambda_S/n}}{1 - \frac{\lambda_S}{n} \cdot \frac{\partial n}{\partial \lambda}}$$

$$\frac{\partial \lambda_S}{\partial T} = \lambda_S \frac{\frac{1}{n} \cdot \frac{\partial n}{\partial T} + \alpha}{1 - \frac{\lambda_S}{n} \cdot \frac{\partial n}{\partial \lambda}}$$

$$\frac{\partial \nu_S}{\partial T} = -\frac{c}{\lambda_S^2}\frac{\partial \lambda_S}{\partial T} = -c\frac{\frac{1}{n}\frac{\partial n}{\partial T} + \alpha}{\lambda_S\left(1 - \frac{\lambda_S}{n}\frac{\partial n}{\partial \lambda}\right)}$$

Appendix C

Stokes center frequency tuning and measurement

The angle scanning was implemented by interfacing with a pico-motor controller newfocus-8742. The code used was:

```
import logging
import asyncio
import timeit
import AtosRead3
from newfocus8742.tcp import NewFocus8742TCP as TCP
from progressbar import ProgressBar

r=[]
totR=[]

for i in range(4):
    r.append([])

for i in range(2):
    totR.append([])

res=10
samples=10
steps=1

async def alg(dev, f, g, co):
    co1=0
    co2=0

    if co==0:
        co1=1
        co2=1
    elif co==1:
        co1=1
        co2=-1

    pbar=ProgressBar()

    for i in pbar(range(res)):
        dev.set_relative(1,co1*steps)
```

```
            await dev.finish(1)

            for j in range(res):
                dev.set_relative(2,co2*steps)
                await dev.finish(2)

                #d=AtosRead3.get_data()

                f.write(str(i))
                f.write('\t')
                f.write(str(j))
                f.write('\t')

                r[0]=[]
                r[1]=[]
                for k in range(samples):
                    d=AtosRead3.get_data(4)
                    r[0].append(d[0])
                    r[1].append(d[1])
                    g.write(str(d[0]))
                    g.write('\t')
                    g.write(str(d[1]))
                    g.write('\n')

                f.write(str(AtosRead3.avg(r[0])))
                f.write('\t')
                f.write(str(AtosRead3.avg(r[1])))
                f.write('\n')

            dev.set_relative(2,-1*steps*co2*res)
            await dev.finish(2)

        dev.set_relative(1,-1*steps*co1*res)
        await dev.finish(1)

def main():
    logging.basicConfig(level=logging.INFO)
    loop = asyncio.get_event_loop()
    loop.set_debug(False)
    async def run():
        dev = await TCP.connect("128.141.233.226")

        if True:

            print(await dev.get_position(1),
            await dev.get_position(2))

            f=open('data.txt', 'w')
            g=open('dataTot.txt', 'w')

            for i in range(2):
```

```
                await alg(dev, f, g, i)
                print(await dev.get_position(1),
                await dev.get_position(2))

            f.close()
            g.close()

            async def k():
                for i in range(100):
                    await dev.error_code()
            import __main__
            __main__.k = k
            __main__.loop = loop
            __main__.dev = dev
    loop.run_until_complete(run())
    print(timeit.timeit("loop.run_until_complete(k())",
        "from __main__ import k, loop", number=1)/100/1)

if __name__ == "__main__":
    main()
```

Library newFocus8742.tcp can be found at https://github.com/quartiq/newfocus8742. The code used to read the Atos LM-007 wavemeter was:

```
import sys
import struct
import socket
import matplotlib.pyplot as plt

from scipy import signal

# Create a TCP/IP socket
sock = socket.socket(socket.AF_INET, socket.SOCK_STREAM)

# Connect the socket to the port where the server is listening
server_address = ('128.141.233.132', 12001)
print('connecting to %s port %s' % server_address, file=sys.stderr)
sock.connect(server_address)

# Select interferometer
def intf(bytes,x):
    if x==1:
        return list(bytes[1:1024])
    elif x==2:
        return list(bytes[1025:2048])
    elif x==3:
        return list(bytes[2049:3072])
    else:
        return list(bytes[3073:4096])

# FSR and Instrumental width in GHz
def const(x):
```

```
    if x==1:
        return [14952, 1420]
    elif x==2:
        return [1026, 99.5]
    elif x==3:
        return [59.9, 5.26]
    else:
        return [3.75, 0.449]

def avg(lst):
    return sum(lst) / len(lst)

# Average peak distance
def peakDist(lst):
    r=[]

    for i in range(len(lst)-1):
        r.append(abs(lst[i]-lst[i+1]))

    if len(r)==0:
        return -1

    return avg(r)

# Average peak width
def width(bytes, x):

    lst=intf(bytes, x)
    peaks,_=signal.find_peaks(lst, prominence=5) # In case of problem with the

    if len(peaks)>5:
        return -1

    pd=peakDist(peaks)

    if pd==-1:
        return 1

    pwa=signal.peak_widths(lst, peaks, rel_height=0.5)

    if len(pwa[0])==0:
        return 1

    pw=avg(pwa[0])

    return pw*const(x)[0]/pd-const(x)[1]

def wavelength(bytes):
    return float(str(10e-5 * struct.unpack('<i', bytes[4097:4101])[0]))

def make_plot(ar, x):
```

```
    ar.append(x)
    if len(ar)>1023000:
        del(ar[0])
    return ar

def get_data(inf):

    # Send data
    sock.sendall(b'\x03\x00')

    # Look for the response
    amount_received = 0
    amount_expected = 4177

    while amount_received < amount_expected:

        # Receive and plot data
        data = sock.recv(amount_expected)
        bytes = bytearray(data)
        amount_received += len(data)
    return [wavelength(bytes), width(bytes, inf)]

print(get_data(4))
```

Finally, the code for reading and setting the temperature of the precision oven was:

```
import sys
import time

C = str(sys.argv)
T = C[21:26]

ser = serial.Serial(
    port= 'COM4',\
    baudrate=19200,\
    parity=serial.PARITY_NONE,\
    stopbits=serial.STOPBITS_ONE,\
    bytesize=serial.EIGHTBITS,\
    timeout=2)

ser.flushInput()
ser.flushOutput()

time.sleep(1)

def read_temp():

    line = ser.readline(64)
    readout = line[11:17]
    print(readout)
```

```
def set_temp(T):
    print('Setting temperature to: ' + T + '\r\n');
    cmd1 = '!inn1;' + T + ';\r\n'
    ser.write(b'n\r\n'+ bytes([13, 10]))
    time.sleep(1)
    ser.write(b'!inn1;'+str(T)';\r\n' + bytes([13, 10]))
    time.sleep(1)
    ser.flushOutput()


#read_temp()
set_temp()

ser.flushInput()
ser.flushOutput()
ser.close()
```

Appendix D

Data presentation for [6]

The data gathered during experiments for the measurement of the thermo-optic coefficient of diamond, were plotted for the publication using the following codes.

Fig. 4.5 (a):

```
from cmath import atan, pi
import numpy as np
import matplotlib.pyplot as plt
import Calc as clc
import seaborn as sns

def main():
    tp, fr, tp2d, fr2d, wd2d, pw2d=clc.splitter()

    font={'family':'Arial', 'size':14}
    plt.rc('font', **font)

    fig, ax=plt.subplots()

    ax.xaxis.set_tick_params(direction='in', top='on')
    ax.yaxis.set_tick_params(direction='in', right='on')

    c=fr[0]

    for i in range(len(fr)):
        fr[i]=fr[i]-c

    temsbot=np.linspace(tp2d[0][-1], tp2d[-1][-1])
    temstop=np.linspace(tp2d[0][0], tp2d[-1][0])

    plt.plot(temsbot,
    -1*clc.delta_raman(temsbot)+clc.delta_raman(temsbot[0])+\
    +fr2d[0][-1]-c-0.5, '--', color='dodgerblue')

    plt.scatter(tp, fr, color='tab:green', s=20,
    label=r'$\nu_S$ (Stokes)', linewidth=0.6, marker='x')

    plt.plot(temstop, -1*clc.delta_raman(temstop)+\
    +clc.delta_raman(tp2d[1][0])+fr2d[1][0]-c, '--',
    label='$FSR\,(T)$', color='dodgerblue')

    plt.xlim([300, 390])
```

```
    plt.tick_params(axis='x')

    plt.tick_params(axis='y')

    plt.xlabel('Temperature (K)')

    plt.ylabel('Frequency detuning (GHz)')

    plt.arrow(tp2d[9][-1], fr2d[9][0]-c+6.5, 0, -3.8,
    width=0.4, color='orange') #2.8

    x=np.linspace(tp2d[9][-1]-2.5, tp2d[9][-1]+2.5)
    temp=[]
    for i in x:
        temp.append(fr2d[9][0]-c+6.5-3.8-1.5*3*0.4)
    plt.plot(x, temp, color='black', linewidth='0.5')

    plt.arrow(tp2d[9][-1], fr2d[9][-1]-c-6, 0, 3.8,
    width=0.4, color='orange')

    x=np.linspace(tp2d[9][-1]-2.5, tp2d[9][-1]+2.5)
    temp=[]
    for i in x:
        temp.append(fr2d[9][-1]-c-6+3.8+1.5*3*0.4)
    plt.plot(x, temp, color='black', linewidth='0.5')

    plt.text(tp2d[9][-1]+1.5, fr2d[9][-1]-c-6, 'FSR')

    plt.legend(fancybox = 0, facecolor = 'white',
    edgecolor='white', loc=(0.05, 0.75), fontsize=13)

    plt.show()

if __name__ == "__main__":
        main()
```

Fig. 4.5 (b) and (c):

```
import matplotlib.pyplot as plt
import Calc as clc
import constants
from scipy.stats import linregress
from mpl_toolkits.axes_grid1.inset_locator import inset_axes
import scipy.optimize
from scipy.stats import t

def roots(hw, *args):
    dvdt=args[0]
    lam=args[1]
    T=args[2]
```

```
    retval=dvdt*lam*(1-lam/clc.n(lam, T,
    constants.CARDONAS_ALPHA, hw)*clc.dndl(lam))/constants.C+
    clc.thermal_expansion(T)\
        +1/clc.n(lam, T, constants.CARDONAS_ALPHA, hw)\
        *clc.dndt(T, constants.CARDONAS_ALPHA, hw)

    return retval

def ft(Tcap, alpha, beta):
    lam=Tcap[0]
    t=Tcap[1]
    betafin=alpha*t+beta#+gamma*t**2#+delta*t**3
    return clc.dfdt(lam, t, constants.CARDONAS_ALPHA,
    betafin)

def ftprev(Tcap, beta):
    lam=Tcap[0]
    t=Tcap[1]
    return clc.dfdt(lam, t, constants.CARDONAS_ALPHA, beta)

def main():
    tp, fr, tp2d, fr2d, wd2d, pw2d=clc.splitter()

    font={'family':'Arial', 'size':14}
    plt.rc('font', **font)

    fig, ax=plt.subplots()

    ax.xaxis.set_tick_params(direction='in', top='on')
    ax.yaxis.set_tick_params(direction='in', right='on')

    tps=[]
    sls=[]
    errs=[]

    tinv = lambda p, df: abs(t.ppf(p/2, df))


    for i in range(len(tp2d)):
        print(len(tp2d[i]))
        slope, intercept, r, p, se = linregress(tp2d[i],
        fr2d[i])
        ts = tinv(0.01, len(tp2d[i])-2)
        see=ts*se
        tps.append((tp2d[i][-1]+tp2d[i][0])/2)
        sls.append(slope)
        errs.append(see)

    tps.pop(0)
    sls.pop(0)
    errs.pop(0)
```

```
plt.errorbar(tps, sls, yerr=errs, ecolor='black',
capsize=4, fmt='o', color='tab:blue', markersize=4,
label='Measurements')

wls=[]

for i in range(len(tps)):
    absolute_difference_function = lambda list_value:
    abs(list_value - tps[i])
    ind=tp.index(min(tp, key=
    absolute_difference_function))
    wls.append(constants.C/fr[ind])

hws=[]
errhws=[]

for i in range(len(tps)):
    roo=scipy.optimize.fsolve(roots, 711, args=(sls[i],
    wls[i], tps[i]))
    a=scipy.optimize.fsolve(roots, 711, args=(sls[i]\
    +errs[i], wls[i], tps[i]))[0]
    b=scipy.optimize.fsolve(roots, 711, args=(sls[i]\
    -errs[i], wls[i], tps[i]))[0]

    hws.append(roo[0])
    errhws.append(abs(a-b)/2)

plt.tick_params(axis='x')

plt.tick_params(axis='y')

plt.xlim([300, 390])
plt.ylim([-3.055, -1.6])

plt.yticks([-1.8-0.2*i for i in range(7)])

plt.xlabel('Temperature␣(K)')

plt.ylabel(r'$\partial{\nu_S}/\partial{T}$␣(GHz/K)')

axins = inset_axes(ax, width=2, height=2,
bbox_to_anchor=(1.02, 1.025),
bbox_transform=ax.transAxes)

axins.xaxis.set_tick_params(direction='in', top='on')
axins.yaxis.set_tick_params(direction='in', right='on')

plt.errorbar(tps, hws, yerr=errhws, ecolor='black',
capsize=2, fmt='o', color='tab:red', markersize=4,
label=r'Calculated␣$\hbar␣\omega(T_i)$')
```

```
    plt.tick_params(axis='x', labelsize=10)

    plt.tick_params(axis='y', labelsize=10)

    plt.xlabel('Temperature␣(K)', fontsize=10)

    plt.ylabel(r'$\hbar\omega\;\left(cm^{-1}\right)$',
    fontsize=10)

    plt.xticks([320, 340, 360])
    # plt.savefig('slopeNewHist.svg')
    # plt.savefig('slopeInset.svg')

    plt.show()

if __name__ == "__main__":
        main()
```

Fig. 4.6:

```
import matplotlib.pyplot as plt
from mpl_toolkits.axes_grid1.inset_locator import inset_axes

def main():

    hours=[]
    temps=[]
    detune=[]

    f = open('data\Stabilized_frequency.txt','r')

    for row in f:
        row = row.split('\t')
        hours.append(float(row[0]))
        temps.append(float(row[1]))
        detune.append(float(row[2]))

    font={'family':'Arial', 'size':14}
    plt.rc('font', **font)

    fig, ax=plt.subplots()

    ax.set_ylim(35.7, 36.1)

    ax.xaxis.set_tick_params(direction='in', top='on')
    ax.yaxis.set_tick_params(direction='in', right='on')

    ax.set_xlabel('Time␣(Hours)')
    ax.set_ylabel(r'Temperature␣($^\circ$C)',
    color='tab:blue')
    ax.plot(hours, temps)
```

```
plt.tick_params(axis='x')

plt.tick_params(axis='y')

ax1 = ax.twinx()

ax1.set_ylim(-90,120)

ax1.plot(hours, detune, color='tab:red')

ax.xaxis.set_tick_params(direction='in', top='on')
ax.yaxis.set_tick_params(direction='in', right='on')

ax1.set_ylabel(r'$\delta␣\nu_s$␣(MHz)', color='tab:red')

plt.tick_params(axis='x')

plt.tick_params(axis='y')

fig.tight_layout()

axins = inset_axes(ax, width=2, height=1.4,
bbox_to_anchor=(0.5, 1),  bbox_transform=ax.transAxes)

axins.xaxis.set_tick_params(direction='in', top='on')
axins.yaxis.set_tick_params(direction='in', right='on')

axins.yaxis.set_label_position("right")
axins.yaxis.tick_right()

plt.xlabel('Temperature␣(K)')

points=[]
sps=[]
f = open('data\Stokes_spectrum.txt','r')

for row in f:
    row = row.split('\t')
    points.append(float(row[0]))
    sps.append(float(row[1]))

plt.plot(points, sps, color='tab:green')

plt.tick_params(axis='x')

plt.tick_params(axis='y')

ax = plt.gca()
ax.axes.xaxis.set_visible(False)
ax.axes.yaxis.set_visible(False)
```

```
    axins.spines['top'].set_visible(False)
    axins.spines['right'].set_visible(False)
    axins.spines['bottom'].set_visible(False)
    axins.spines['left'].set_visible(False)

    plt.arrow(-950, max(sps)/2, 400, 0, width=0.01,
    color='orange', head_width=0.05, head_length=200)

    plt.arrow(1020, max(sps)/2, -400, 0, width=0.01,
    color='orange', head_width=0.05, head_length=200)

    plt.text(-1500, 0.15, r'$\Delta␣\nu_S=100$␣MHz',
    rotation=90, color='black', fontsize=10)

    # plt.savefig('stability.pdf')

    plt.show()

if __name__ == "__main__":
        main()
```

Fig. 4.7:

```
import matplotlib.pyplot as plt
import Calc as clc
import constants
from scipy.stats import linregress
import scipy.optimize
from scipy.stats import t

def roots(hw, *args):
    dvdt=args[0]
    lam=args[1]
    T=args[2]

    retval=dvdt*lam*(1-lam/clc.n(lam, T,
        constants.CARDONAS_ALPHA, hw)*clc.dndl(lam))\
        /constants.C+clc.thermal_expansion(T)\
        +1/clc.n(lam, T, constants.CARDONAS_ALPHA, hw)\
        *clc.dndt(T, constants.CARDONAS_ALPHA, hw)

    return retval

def main():
    tp, fr, tp2d, fr2d, wd2d, pw2d=clc.splitter()

    tps=[]
    sls=[]
    errs=[]
```

```
tinv = lambda p, df: abs(t.ppf(p/2, df))

for i in range(len(tp2d)):
    slope, intercept, r, p, se = linregress(tp2d[i],
        fr2d[i])
    ts = tinv(0.01, len(tp2d[i])-2)
    see=ts*se
    tps.append((tp2d[i][-1]+tp2d[i][0])/2)
    sls.append(slope)
    errs.append(see)

tps.pop(0)
sls.pop(0)
errs.pop(0)

wls=[]

for i in range(len(tps)):
    absolute_difference_function = lambda list_value:
        abs(list_value - tps[i])
    ind=tp.index(min(tp,
        key=absolute_difference_function))
    wls.append(constants.C/fr[ind])

hws=[]
errhws=[]

for i in range(len(tps)):
    roo=scipy.optimize.fsolve(roots, 711,
        args=(sls[i], wls[i], tps[i]))
    a=scipy.optimize.fsolve(roots, 711,
        args=(sls[i]+errs[i], wls[i], tps[i]))[0]
    b=scipy.optimize.fsolve(roots, 711,
        args=(sls[i]-errs[i], wls[i], tps[i]))[0]

    hws.append(roo[0])
    errhws.append(abs(a-b)/2)

font={'family':'Arial', 'size':14}
plt.rc('font', **font)

fig, ax=plt.subplots()

ax.xaxis.set_tick_params(direction='in', top='on')
ax.yaxis.set_tick_params(direction='in', right='on')

temp=[]
errtemp=[]

for i in range(len(hws)):
```

```
            temp.append(clc.dndt(tps[i],
                constants.CARDONAS_ALPHA, hws[i])/clc.n(wls[i],
                tps[i], constants.CARDONAS_ALPHA, hws[i]))
            a=clc.dndt(tps[i], constants.CARDONAS_ALPHA,
                hws[i]+errhws[i])/clc.n(wls[i], tps[i],
                constants.CARDONAS_ALPHA, hws[i]+errhws[i])
            b=clc.dndt(tps[i], constants.CARDONAS_ALPHA,
                hws[i]-errhws[i])/clc.n(wls[i], tps[i],
                constants.CARDONAS_ALPHA, hws[i]-errhws[i])
            errtemp.append(abs(a-b)/2)

            print(tps[i], clc.dfdt(433.9, tps[i],
                constants.CARDONAS_ALPHA, hws[i]))

        plt.errorbar(tps, temp, yerr=errtemp, ecolor='black',
            capsize=4, fmt='o', color='tab:green', markersize=4,
            label='Caclulated values')

        plt.tick_params(axis='x')

        plt.tick_params(axis='y')

        plt.xlabel('Temperature (K)')#

        plt.ylabel(r'$\frac{1}{n\,}\frac{\partial{n}}
{\partial{T}}$ (K$^{-1}$)')

        # plt.savefig('thermoNoLinearNew.pdf')

        plt.show()

if __name__ == "__main__":
        main()
```

Appendix E

Data presentation for [5]

The data gathered during experiments for the demonstration of double resonance, were plotted for the publication using the following codes.

Fig. 5.4:

```
from cmath import atan, pi
import numpy as np
import matplotlib.pyplot as plt
import Calc as clc
from mpl_toolkits.axes_grid1.inset_locator import inset_axes

def lorentzian(a, gamma):
    # print(l*gamma)
    x=np.linspace(-1430, 1430, 10000)
    return x/1000, a*gamma/(x**2+(gamma/2)**2)/2/pi

def main():
    tp=[]
    wl=[]
    wd=[]
    pw=[]

    f = open('data.txt','r')

    for row in f:
        row = row.split('\t')
        tp.append(float(row[0])+273.16)
        wl.append(float(row[1])/10)
        wd.append(float(row[2])*1e3)
        pw.append(float(row[3]))

    fr=clc.fre2lam(wl)

    font={'family':'Arial', 'size':13}
    plt.rc('font', **font)

    fig, ax=plt.subplots()

    ax.xaxis.set_tick_params(direction='in', top='on')
    ax.yaxis.set_tick_params(direction='in', right='on')
```

```
c=fr[0]

for i in range(len(fr)):
    fr[i]=fr[i]-c

plt.scatter(tp, fr, c=wd, cmap='jet_r', s=50,
    linewidth=0.1, marker='.')

plt.plot(300, 26)

plt.xlabel('Temperature␣(K)')

plt.ylabel(r'$\nu_S-\nu_0$␣(GHz)')

plt.clim(min(wd), 500)

axinsColor=inset_axes(ax,
                      width="40%",
                      height="5%",
                      loc='lower␣right',
                      bbox_to_anchor=(0.15, 0.1, 0.8, 0.5),
                      bbox_transform=ax.transAxes,
                      borderpad=1,)

clb=plt.colorbar(cax=axinsColor,
    orientation="horizontal", ticks=[150, 320, 500])
clb.ax.set_title(r'Linewidth␣$\Delta\nu_S$␣(MHz)',
    fontsize=13)
axinsColor.xaxis.set_ticks_position("bottom")

axinslin=inset_axes(ax,
                      width="40%",
                      height="60%",
                      loc='upper␣left',
                      bbox_to_anchor=(0.15, 0.35, 0.8,
                          0.6),
                      bbox_transform=ax.transAxes,
                      borderpad=0,)

axinslin.spines['right'].set_visible(False)
axinslin.spines['top'].set_visible(False)

axinslin.set_xlabel(r'$\nu$␣(GHz)', fontsize=10)
axinslin.set_ylabel('PSD␣(kW/GHz)', fontsize=10)

narrow_index=4907
broad_index=4594

cmap=plt.cm.get_cmap('jet_r')

fres, power=lorentzian(pw[broad_index], wd[broad_index])
```

```
    axinslin.plot(fres, power*1e7, color=cmap(
        round((wd[broad_index]-min(wd))/max(wd)*500)),
        label='Singly resonant')

    fres, power=lorentzian(pw[narrow_index],
    wd[narrow_index])

    axinslin.plot(fres, power*1e7,
        color=cmap(round((wd[narrow_index]-min(wd))/max(wd)\
        *500)), label='Doubly resonant')

    axinslin.legend(loc=(0.7, 0.7), fontsize=10,
        frameon=False)

    # plt.savefig('data.svg', format='svg', transparent=True)

    plt.show()

if __name__ == "__main__":
        main()
```

Fig. 5.5:

```
import numpy as np
import matplotlib.pyplot as plt
import Calc as clc
from scipy.stats import linregress
from mpl_toolkits.axes_grid1.inset_locator import inset_axes
from scipy.stats import sem
from scipy.signal import find_peaks

tp=[]
wl=[]
wd=[]
pw=[]

f = open('data.txt','r')

for row in f:
    row = row.split('\t')
    tp.append(float(row[0])+273.16)
    wl.append(float(row[1])/10)
    wd.append(float(row[2])*1e3)
    pw.append(float(row[3]))

fr=clc.fre2lam(wl)

c=fr[0]

for i in range(len(fr)):
    fr[i]=fr[i]-c
```

```
tp_single=[]
fr_single=[]
wd_single=[]
std=[]

tp=[i for _,i in sorted(zip(fr, tp))]
wd=[i for _,i in sorted(zip(fr, wd))]
fr.sort()

fr_new=[]
wd_new=[]
tp_new=[]

counter=0

while True:
    for i in range(len(fr[counter:])):
        if fr[i]>fr[counter]+0.05:
            fr_new.append(fr[wd.index(min(wd[counter:i]))])
            tp_new.append(tp[wd.index(min(wd[counter:i]))])
            wd_new.append(min(wd[counter:i]))

            if fr_new[-1]>8.2 and fr_new[-1]<12.3:
                fr_single.append(fr_new[-1])
                wd_single.append(wd_new[-1])
                std.append(sem(wd[counter:i]))

            counter=i+1
    if counter==len(fr) or fr[counter]+0.5>fr[-1]:
        break

wd_new=[i for _,i in sorted(zip(fr_new, wd_new))]
tp_new=[i for _,i in sorted(zip(fr_new, tp_new))]
fr_new.sort()

wd_single=[i for _,i in sorted(zip(fr_single, wd_single))]
fr_single.sort()

fr_new.pop()
wd_new.pop()
tp_new.pop()

for i in range(len(fr_new)):
    if fr_new[i]>-2.22:
        fr_new=fr_new[i:]
        wd_new=wd_new[i:]
        tp_new=tp_new[i:]
        break

fr_min=[]
```

```
wd_min=[]
tp_min=[]

peaks, _=find_peaks(-1*np.array(wd_new), prominence=150,
    width=5)

for i in peaks:
    fr_min.append(fr_new[i])
    wd_min.append(wd_new[i])
    tp_min.append(tp_new[i])

fr_min.insert(-1, fr_new[-2])
wd_min.insert(-1, wd_new[-2])
tp_min.insert(-1, tp_new[-2])

std_min=[]

for i in range(len(fr_min)):
    ind=fr.index(fr_min[i])

    temp=wd[ind-5:ind+5]

    j=0

    while True:
        if abs(temp[j]-wd_min[i])>100:
            temp.pop(j)
            j=j-1
        j=j+1

        if j==len(temp):
            break
    std_min.append(sem(temp))

font={'family':'Arial', 'size':13}
plt.rc('font', **font)

fig, ax=plt.subplots()

ax.xaxis.set_tick_params(direction='in', top='on')
ax.yaxis.set_tick_params(direction='in', right='on')

plt.plot(fr_new, wd_new, color='blue')

plt.xlabel(r'$\nu_S-\nu_0$ (GHz)')

plt.ylabel(r'Linewidth $\Delta\nu_S$ (MHz)')

plt.plot(0, 1000)

axinsingle=inset_axes(ax,
```

```
                        width="40%",
                        height="60%",
                        loc='upper left',
                        bbox_to_anchor=(0.15, 0.3, 0.8, 0.6),
                        bbox_transform=ax.transAxes,
                        borderpad=0,)

axinsingle.tick_params(axis='x', labelsize=10)
axinsingle.tick_params(axis='y', labelsize=10)

axinsingle.set_xlabel(r'$\nu_S-\nu_0$ (GHz)', fontsize=10)
axinsingle.set_ylabel(r'Linewidth $\Delta\nu_S$ (MHz)',
    fontsize=10)

axinsingle.plot(fr_single, wd_single, color='blue')
axinsingle.fill_between(fr_single, np.array(wd_single)\
    -np.array(std), np.array(wd_single)+np.array(std),
    color='tab:red', alpha=0.4)

axinsingle=inset_axes(ax,
                        width="40%",
                        height="60%",
                        loc='upper right',
                        bbox_to_anchor=(0.15, 0.3, 0.8, 0.6),
                        bbox_transform=ax.transAxes,
                        borderpad=0,)

axinsingle.tick_params(axis='x', labelsize=10)
axinsingle.tick_params(axis='y', labelsize=10)

axinsingle.set_xlabel('Temperature (K)', fontsize=10)
axinsingle.set_ylabel(r'Min. Linewidth $\Delta\nu_S$ (MHz)',
    fontsize=10)

fr_min.pop(1)
wd_min.pop(1)
tp_min.pop(1)
std_min.pop(1)

lin=linregress(tp_min, wd_min)

t=np.linspace(min(tp_min), max(tp_min))

axinsingle.plot(t, t*lin[0]+lin[1], color='blue')

axinsingle.errorbar(tp_min, wd_min, yerr=std_min, capsize=4,
    capthick=1, ls='none')

axinsingle.scatter(tp_min, wd_min, color='tab:red')
# plt.savefig('dip.svg', format='svg', transparent=True)
plt.show()
```

Fig. 5.6:

```
from cmath import pi
import matplotlib.pyplot as plt
import numpy as  np
import Calc as clc
from scipy.stats import linregress
from mpl_toolkits.axes_grid1.inset_locator import inset_axes

tp=[]
wl=[]
wd=[]
pw=[]

f = open('data.txt','r')

for row in f:
    row = row.split('\t')
    if float(row[0])>84.52 and float(row[0])<86.71:
        tp.append(float(row[0])+273.16)
        wl.append(float(row[1])/10)
        wd.append(float(row[2]))
        pw.append(float(row[3])*1e4)

fr=clc.fre2lam(wl)

c=fr[0]

for i in range(len(fr)):
    fr[i]=fr[i]-c

font={'family':'Arial', 'size':13}
plt.rc('font', **font)

fig, ax=plt.subplots()

ax.set_xlabel('Temperature (K)')
ax.set_ylabel(r'$\nu_S-\nu_0$ (GHz)')

ax.set_xticks([358.0, 358.5, 359.0, 359.5])

slope, intercept, r, p, se = linregress(tp, fr)

TPS, FRS=np.meshgrid(tp, fr)
TPS, WDS=np.meshgrid(tp, wd)
TPS, PWS=np.meshgrid(tp, pw)

Z=PWS*WDS/2/pi/((FRS-(slope*TPS+intercept))**2+(WDS/2)**2)

mapa=ax.contour(TPS, FRS, Z, 100, cmap='jet')
```

```
axinsColor=inset_axes(ax,
                      width="40%",
                      height="8%",
                      loc='lower left',
                      bbox_to_anchor=(0., 0.1, 0.8, 0.5),
                      bbox_transform=ax.transAxes,
                      borderpad=1,)

clb=fig.colorbar(mapa, cax=axinsColor,
    orientation="horizontal", ticks=[0, 21.6])
clb.ax.set_title('PSD (kW/GHz)', fontsize=13)
axinsColor.xaxis.set_ticks_position("bottom")

# plt.savefig('psd.pdf')
plt.show()
```

Bibliography

[1] Pawel Latawiec et al. "On-chip diamond Raman laser". In: *Optica* 2.11 (Nov. 2015), pp. 924–928. DOI: 10.1364/OPTICA.2.000924. URL: http://opg.optica.org/optica/abstract.cfm?URI=optica-2-11-924.

[2] Eduardo Granados et al. "Spectral synthesis of multimode lasers to the Fourier limit in integrated Fabry–Perot diamond resonators". In: *Optica* 9.3 (Mar. 2022), pp. 317–324. DOI: 10.1364/OPTICA.447380. URL: https://opg.optica.org/optica/abstract.cfm?URI=optica-9-3-317.

[3] E. Granados et al. "Tunable spectral squeezers based on monolithically integrated diamond Raman resonators". In: *Applied Physics Letters* 120.15 (2022), p. 151101. DOI: 10.1063/5.0088592. eprint: https://doi.org/10.1063/5.0088592. URL: https://doi.org/10.1063/5.0088592.

[4] Thomas Moses et al. "A simpler scanning Fabry-Perot interferometer for high-resolution spectroscopy experiments". In: *American Journal of Physics* 83.7 (2015), pp. 656–659. DOI: 10.1119/1.4921391. eprint: https://doi.org/10.1119/1.4921391. URL: https://doi.org/10.1119/1.4921391.

[5] Eduardo Granados and Georgios Stoikos. "Spectral purification of single-frequency Stokes pulses in doubly resonant integrated diamond resonators". In: *Opt. Lett.* 47.16 (Aug. 2022), pp. 3976–3979. DOI: 10.1364/OL.464816. URL: https://opg.optica.org/ol/abstract.cfm?URI=ol-47-16-3976.

[6] Georgios Stoikos and Eduardo Granados. "Influence of phonon harmonicity on spectrally pure resonant Stokes fields". In: *Phys. Rev. A* 106 (2 Aug. 2022), p. 023504. DOI: 10.1103/PhysRevA.106.023504. URL: https://link.aps.org/doi/10.1103/PhysRevA.106.023504.

[7] Matthew A. Norcia et al. "Frequency Measurements of Superradiance from the Strontium Clock Transition". In: *Phys. Rev. X* 8 (2 May 2018), p. 021036. DOI: 10.1103/PhysRevX.8.021036. URL: https://link.aps.org/doi/10.1103/PhysRevX.8.021036.

[8] C. J. Baker et al. "Laser cooling of antihydrogen atoms". In: *Nature* 592.7852 (Apr. 2021), pp. 35–42. ISSN: 1476-4687. DOI: 10.1038/s41586-021-03289-6. URL: https://doi.org/10.1038/s41586-021-03289-6.

[9] Karan K. Mehta et al. "Integrated optical multi-ion quantum logic". In: *Nature* 586.7830 (Oct. 2020), pp. 533–537. ISSN: 1476-4687. DOI: 10.1038/s41586-020-2823-6. URL: https://doi.org/10.1038/s41586-020-2823-6.

[10] C. Granados et al. "In-gas laser ionization and spectroscopy of actinium isotopes near the $N = 126$ closed shell". In: *Phys. Rev. C* 96 (5 Nov. 2017), p. 054331. DOI: 10.1103/PhysRevC.96.054331. URL: https://link.aps.org/doi/10.1103/PhysRevC.96.054331.

[11] Quntao Zhuang, Zheshen Zhang, and Jeffrey H. Shapiro. "Entanglement-enhanced lidars for simultaneous range and velocity measurements". In: *Phys. Rev. A* 96 (4 Oct. 2017), p. 040304. DOI: 10.1103/PhysRevA.96.040304. URL: https://link.aps.org/doi/10.1103/PhysRevA.96.040304.

[12] Kim Patokoski et al. "Single-frequency 100 ns / 0.5 mJ laser pulses from all-fiber double clad ytterbium doped tapered fiber amplifier". In: *Opt. Express* 27.22 (Oct. 2019), pp. 31532–31541. DOI: 10.1364/OE.27.031532. URL: https://opg.optica.org/oe/abstract.cfm?URI=oe-27-22-31532.

[13] Jed Rowland et al. "Using an injection-locked VCSEL to produce Fourier-transform-limited optical pulses". In: *Opt. Lett.* 46.2 (Jan. 2021), pp. 412–415. DOI: 10.1364/OL.416166. URL: https://opg.optica.org/ol/abstract.cfm?URI=ol-46-2-412.

[14] K. Chrysalidis et al. "First demonstration of Doppler-free 2-photon in-source laser spectroscopy at the ISOLDE-RILIS". In: *Nuclear Instruments and Methods in Physics Research Section B: Beam Interactions with Materials and Atoms* 463 (2020), pp. 476–481. ISSN: 0168-583X. DOI: https://doi.org/10.1016/j.nimb.2019.04.020. URL: https://www.sciencedirect.com/science/article/pii/S0168583X19302046.

[15] Wikipedia. *Stimulated Raman scattering*. URL: https://en.wikipedia.org/wiki/Stimulated_Raman_spectroscopy.

[16] Daniel T Echarri et al. "Tunable diamond raman lasers for resonance photoionization and ion beam production". In: *Frontiers in Physics* (2022), p. 697.

[17] Oliver Lux et al. "Single longitudinal mode diamond Raman laser in the eye-safe spectral region for water vapor detection". In: *Opt. Express* 24.24 (Nov. 2016), pp. 27812–27820. DOI: 10.1364/OE.24.027812. URL: http://www.opticsexpress.org/abstract.cfm?URI=oe-24-24-27812.

[18] Oliver Lux et al. "Intrinsically stable high-power single longitudinal mode laser using spatial hole burning free gain". In: *Optica* 3.8 (Aug. 2016), pp. 876–881. DOI: 10.1364/OPTICA.3.000876. URL: https://opg.optica.org/optica/abstract.cfm?URI=optica-3-8-876.

[19] A. S. Grabtchikov et al. "Multimode pumped continuous-wave solid-state Raman laser". In: *Opt. Lett.* 29.21 (Nov. 2004), pp. 2524–2526. DOI: 10.1364/OL.29.002524. URL: http://opg.optica.org/ol/abstract.cfm?URI=ol-29-21-2524.

[20] Peter Dekker, Helen M. Pask, and James A. Piper. "All-solid-state 704 mW continuous-wave yellow source based on an intracavity, frequency-doubled crystalline Raman laser". In: *Opt. Lett.* 32.9 (May 2007), pp. 1114–1116. DOI: 10.1364/OL.32.001114. URL: http://opg.optica.org/ol/abstract.cfm?URI=ol-32-9-1114.

[21] Wikipedia. *Raman laser guide star*. URL: https://en.wikipedia.org/wiki/Laser_guide_star.

[22] Xuezong Yang et al. "Single-frequency 620 nm diamond laser at high power, stabilized via harmonic self-suppression and spatial-hole-burning-free gain". In: *Opt. Lett.* 44.4 (Feb. 2019), pp. 839–842. DOI: 10.1364/OL.44.000839. URL: http://opg.optica.org/ol/abstract.cfm?URI=ol-44-4-839.

[23] Oliver Lux et al. "Single longitudinal mode diamond Raman laser in the eye-safe spectral region for water vapor detection". In: *Opt. Express* 24.24 (Nov. 2016), pp. 27812–27820. DOI: 10.1364/OE.24.027812. URL: https://opg.optica.org/oe/abstract.cfm?URI=oe-24-24-27812.

[24] Ondrej Kitzler et al. "Single-longitudinal-mode ring diamond Raman laser". In: *Opt. Lett.* 42.7 (Apr. 2017), pp. 1229–1232. DOI: 10.1364/OL.42.001229. URL: https://opg.optica.org/ol/abstract.cfm?URI=ol-42-7-1229.

[25] Ozdal Boyraz and Bahram Jalali. "Demonstration of a silicon Raman laser". In: *Opt. Express* 12.21 (Oct. 2004), pp. 5269–5273. DOI: 10.1364/OPEX.12.005269. URL: http://opg.optica.org/oe/abstract.cfm?URI=oe-12-21-5269.

[26] Eduardo Granados, David J. Spence, and Richard P. Mildren. "Deep ultraviolet diamond Raman laser". In: *Opt. Express* 19.11 (May 2011), pp. 10857–10863. DOI: 10.1364/OE.19.010857. URL: http://opg.optica.org/oe/abstract.cfm?URI=oe-19-11-10857.

[27] Rich P. Mildren. "Intrinsic Optical Properties of Diamond". In: *Optical Engineering of Diamond*. John Wiley & Sons, Ltd, 2013. Chap. 1, pp. 1–34. ISBN: 9783527648603. DOI: https://doi.org/10.1002/9783527648603.ch1. eprint: https://onlinelibrary.wiley.com/doi/pdf/10.1002/9783527648603.ch1. URL: https://onlinelibrary.wiley.com/doi/abs/10.1002/9783527648603.ch1.

[28] J. H. Parker, D. W. Feldman, and M. Ashkin. "Raman Scattering by Silicon and Germanium". In: *Phys. Rev.* 155 (3 Mar. 1967), pp. 712–714. DOI: 10.1103/PhysRev.155.712. URL: https://link.aps.org/doi/10.1103/PhysRev.155.712.

[29] James A. Piper and Helen M. Pask. "Crystalline Raman Lasers". In: *IEEE Journal of Selected Topics in Quantum Electronics* 13.3 (2007), pp. 692–704. DOI: 10.1109/JSTQE.2007.897175.

[30] Tasoltan T. Basiev et al. "Comparative spontaneous Raman spectroscopy of crystals for Raman lasers". In: *Appl. Opt.* 38.3 (Jan. 1999), pp. 594–598. DOI: 10.1364/AO.38.000594. URL: https://opg.optica.org/ao/abstract.cfm?URI=ao-38-3-594.

[31] Daniel T. Echarri et al. "Broadly tunable linewidth-invariant Raman Stokes comb for selective resonance photoionization". In: *Opt. Express* 28.6 (Mar. 2020), pp. 8589–8600. DOI: 10.1364/OE.384630. URL: http://www.opticsexpress.org/abstract.cfm?URI=oe-28-6-8589.

[32] R. P. Mildren and A. Sabella. "Highly efficient diamond Raman laser". In: *Opt. Lett.* 34.18 (Sept. 2009), pp. 2811–2813. DOI: 10.1364/OL.34.002811. URL: http://opg.optica.org/ol/abstract.cfm?URI=ol-34-18-2811.

[33] Sean Reilly et al. "Monolithic diamond Raman laser". In: *Opt. Lett.* 40.6 (Mar. 2015), pp. 930–933. DOI: 10.1364/OL.40.000930. URL: http://opg.optica.org/ol/abstract.cfm?URI=ol-40-6-930.

[34] Alexander Valavanis. "n-type silicon-germanium based terahertz quantum cascade lasers". In: (July 2009).

[35] V G Sidorovich. "Reproduction of the pump spectrum in stimulated Raman scattering". In: *Soviet Journal of Quantum Electronics* 8.6 (June 1978), pp. 784–785. DOI: 10.1070/qe1978v008n06abeh010403. URL: https://doi.org/10.1070/qe1978v008n06abeh010403.

[36] Katsunari Okamoto. "Chapter 5 - Nonlinear Optical Effects in Optical Fibers". In: *Fundamentals of Optical Waveguides (Third Edition)*. Ed. by Katsunari Okamoto. Third Edition. Academic Press, 2022, pp. 219–269. ISBN: 978-0-12-815601-8. DOI: https://doi.org/10.1016/B978-0-12-815601-8.50005-7. URL: https://www.sciencedirect.com/science/article/pii/B9780128156018500057.

[37] Ming S. Liu et al. "Temperature dependence of the first-order Raman phonon line of diamond". In: *Phys. Rev. B* 61 (5 Feb. 2000), pp. 3391–3395. DOI: 10.1103/PhysRevB.61.3391. URL: https://link.aps.org/doi/10.1103/PhysRevB.61.3391.

[38] Katerina Chrysalidis et al. "Continuously tunable diamond Raman laser for resonance laser ionization". In: *Opt. Lett.* 44.16 (Aug. 2019), pp. 3924–3927. DOI: 10.1364/OL.44.003924. URL: https://opg.optica.org/ol/abstract.cfm?URI=ol-44-16-3924.

[39] John Fontanella et al. "Temperature and pressure variation of the refractive index of diamond". In: *Appl. Opt.* 16.11 (Nov. 1977), pp. 2949–2951. DOI: 10.1364/AO.16.002949. URL: http://www.osapublishing.org/ao/abstract.cfm?URI=ao-16-11-2949.

[40] T. Ruf et al. "Temperature dependence of the refractive index of diamond up to 925K". In: *Phys. Rev. B* 62 (24 Dec. 2000), pp. 16578–16581. DOI: 10.1103/PhysRevB.62.16578. URL: https://link.aps.org/doi/10.1103/PhysRevB.62.16578.

[41] Giorgio Turri et al. "Index of refraction from the near-ultraviolet to the near-infrared from a single crystal microwave-assisted CVD diamond". In: *Opt. Mater. Express* 7.3 (Mar. 2017), pp. 855–859. DOI: 10.1364/OME.7.000855. URL: http://www.osapublishing.org/ome/abstract.cfm?URI=ome-7-3-855.

[42] R. Loudon. "The Raman effect in crystals". In: *Advances in Physics* 13.52 (1964), pp. 423–482. DOI: 10.1080/00018736400101051. eprint: https://doi.org/10.1080/00018736400101051. URL: https://doi.org/10.1080/00018736400101051.

[43] Jesus Gonzalez, E. Moya, and J. Chervin. "Anharmonic effects in light scattering due to optical phonons in CuGaS_2". In: *Phys. Rev. B* 54 (Aug. 1996). DOI: 10.1103/PhysRevB.54.4707.

[44] P. Jacobson and S. Stoupin. "Thermal expansion coefficient of diamond in a wide temperature range". In: *Diamond and Related Materials* 97 (2019), p. 107469. ISSN: 0925-9635. DOI: https://doi.org/10.1016/j.diamond.2019.107469. URL: https://www.sciencedirect.com/science/article/pii/S0925963519303851.

[45] P. G. Klemens. "Anharmonic Decay of Optical Phonons". In: *Phys. Rev.* 148 (2 Aug. 1966), pp. 845–848. DOI: 10.1103/PhysRev.148.845. URL: https://link.aps.org/doi/10.1103/PhysRev.148.845.

[46] Alberto Debernardi, Stefano Baroni, and Elisa Molinari. "Anharmonic Phonon Lifetimes in Semiconductors from Density-Functional Perturbation Theory". In: *Phys. Rev. Lett.* 75 (9 Aug. 1995), pp. 1819–1822. DOI: 10.1103/PhysRevLett.75.1819. URL: https://link.aps.org/doi/10.1103/PhysRevLett.75.1819.

[47] Reinhard Heinke. "In-source high-resolution spectroscopy of holmium radioisotopes - On-line tailored perpendicular laser interaction at ISOLDE's Laser Ion Source and Trap LIST". Presented 16 Oct 2019. 2019. URL: https://cds.cern.ch/record/2718446.

[48] S. Warren et al. "Offline 2, ISOLDE's target, laser and beams development facility". In: *Nuclear Instruments and Methods in Physics Research Section B: Beam Interactions with Materials and Atoms* 463 (2020), pp. 115–118. ISSN: 0168-583X. DOI: https://doi.org/10.1016/j.nimb.2019.07.016. URL: https://www.sciencedirect.com/science/article/pii/S0168583X19305075.

[49] S. Rothe et al. "Laser ion beam production at CERN-ISOLDE: New features – More possibilities". In: *Nuclear Instruments and Methods in Physics Research Section B: Beam Interactions with Materials and Atoms* 376 (2016). Proceedings of the XVIIth International Conference on Electromagnetic Isotope Separators and Related Topics (EMIS2015), Grand Rapids, MI, U.S.A., 11-15 May 2015, pp. 91–96. ISSN: 0168-583X. DOI: https://doi.org/10.1016/j.nimb.2016.02.024. URL: https://www.sciencedirect.com/science/article/pii/S0168583X1600152X.

[50] Jonathan Levine. "A simplified calculation of power-broadened linewidths, with application to resonance ionization mass spectrometry". In: *Spectrochimica Acta Part B: Atomic Spectroscopy* 69 (2012), pp. 61–66. ISSN: 0584-8547. DOI: https://doi.org/10.1016/j.sab.2012.02.001. URL: https://www.sciencedirect.com/science/article/pii/S0584854712000298.